Numerical Analysis of the Metal Spinning Process Utilizing Rotating Reference Frames

by

Huy-Hoan NGUYEN

THESIS PRESENTED TO ÉCOLE DE TECHNOLOGIE SUPÉRIEURE IN PARTIAL FULFILLEMENT OF THE REQUIREMENTS FORTHE DEGREE OF DOCTOR OF PHILOSOPHY
Ph. D

MONTREAL, JULY 17, 2024

ÉCOLE DE TECHNOLOGIE SUPÉRIEURE
UNIVERSITÉ DU QUÉBEC

BOARD OF EXAMINERS

THIS THESIS HAS BEEN EVALUATED

BY THE FOLLOWING BOARD OF EXAMINERS

M. Henri Champliaud, Thesis Supervisor
Department of Mechanical Engineering at École de technologie supérieure

M. Van Ngan Lê, Thesis Co-supervisor
Department of Mechanical Engineering at École de technologie supérieure

M. Julio Montecinos, President of the Board of Examiners
Department of Systems Engineering at École de technologie supérieure

M. Zhaoheng Liu, Member of the jury
Department of Mechanical Engineering at École de technologie supérieure

M. Thien-My Dao, Member of the jury
Department of Mechanical Engineering at École de technologie supérieure

M. Lyès Hacini, External Evaluator
Hatch Ltd.

THIS THESIS WAS PRESENTED AND DEFENDED

IN THE PRESENCE OF A BOARD OF EXAMINERS AND PUBLIC

ON JULY 4, 2024

AT ÉCOLE DE TECHNOLOGIE SUPÉRIEURE

ACKNOWLEDGMENTS

I express my deep gratitude to my supervisor, Professor Henri Champliaud, for his unwavering patience, invaluable guidance, and constant encouragement throughout the course of this research endeavor.

I extend sincere appreciation to my co-supervisor, Professor Van Ngan Lê, for his diligent supervision, unwavering support, and constructive feedback that greatly enriched my work.

Furthermore, I would like to extend my gratitude to the esteemed jury members for graciously accepting the responsibility of evaluating this thesis and for their insightful feedback, which has been instrumental in enhancing the quality of this work.

We acknowledge the support of the Natural Sciences and Engineering Research Council of Canada (NSERC), [funding reference number 05972].

ANALYSE NUMÉRIQUE DU PROCÉDÉ DE REPOUSSAGE UTILISANT DES RÉFÉRENTIELS ROTATIFS

Huy-Hoan NGUYEN

RÉSUMÉ

Le procédé de repoussage, une technique de formage de tôles minces, fabrique des produits de forme axisymétrique à partir de pièces circulaires en exploitant les propriétés de déformation plastique des matériaux métalliques. Malgré son utilisation généralisée, des lacunes significatives persistent dans notre compréhension de ce procédé, comme le révèle la littérature existante. Les domaines clés nécessitant une investigation plus approfondie comprennent : la caractérisation incomplète de l'évolution des contraintes et des déformations au-delà du domaine élastique; une compréhension limitée des mécanismes de défaillance tels que les fissures et les plis ; et le manque de méthodes fiables pour concevoir des trajectoires d'outil afin de produire des pièces finales sans défauts. Cette thèse aborde ces lacunes en mettant en œuvre un modèle numérique configuré dans un cadre de référence rotatif, ce qui se traduit par une réduction substantielle du temps de calcul d'un facteur de 50 tout en améliorant la précision. De plus, l'intégration du modèle d'endommagement dépendant de l'état de contrainte incrémentiel généralisé dans cette configuration de cadre de référence rotatif améliore la prédiction de la fissuration circonférentielle. Une approche novatrice est proposée pour analyser le procédé tout au long d'une rotation complète du mandrin, plutôt que seulement à la fin du procédé, ce qui a été validé par rapport à la littérature existante. Cette analyse montre que le rayon du rebord diminue à chaque déformation plastique induite par le rouleau, entraînant le développement de plis sur le rebord. Deux paramètres spécifiques, à savoir l'amplitude et le nombre de pics, sont utilisés pour caractériser la forme des plis du rebord, révélant une relation inverse entre eux en raison de la cohérence volumétrique. Notamment, l'apparition de nouveaux pics se produit continuellement pendant le procédé. Les trajectoires intermédiaires avec des angles de course appropriés sont identifiées comme des moyens efficaces de contrôler en toute sécurité l'amplitude des plis en augmentant le nombre de pics. De plus, ces trajectoires intermédiaires atténuent les problèmes d'amincissement dans le produit final.

Mots-Clés: Procédé de repoussage, défaut de repli, modélisation par éléments finis, conception de trajectoire d'outil

NUMERICAL ANALYSIS OF THE METAL SPINNING PROCESS UTILIZING ROTATING REFERENCE FRAMES

Huy-Hoan NGUYEN

ABSTRACT

The metal spinning process, a metalworking technique, fabricates axisymmetric shaped products from circular workpieces by leveraging the plastic deformation properties of certain metals. Despite its widespread use, significant gaps persist in our understanding of this process as revealed by existing literature. Key areas requiring further investigation include: the incomplete characterization of stress and strain evolution beyond the elastic domain; a limited understanding of failure mechanisms such as cracking and wrinkling; and the lack of reliable methods for designing toolpaths to produce final parts without defects. This thesis addresses these gaps by implementing a numerical model configured within a rotating reference frame, resulting in a substantial reduction in computational time by a factor of 50 while improving accuracy. Furthermore, the integration of the Generalized Incremental Stress State dependent damage Model within this rotating reference frame configuration enhances the prediction of circumferential cracking efficiency. A novel approach is proposed for analyzing the process throughout one full rotation of the mandrel, as opposed to solely at the end of the process, which has been validated against existing literature. This analysis exhibits that the flange radius diminishes with each plastic deformation induced by the roller, leading to the development of wrinkles on the flange. Two specific parameters, namely the amplitude and the number of peaks, are employed to characterize the flange wrinkling shape, revealing an inverse relationship between them due to volume consistency. Notably, the appearance of new peaks continuously during the process is observed. Intermediate paths with appropriate stroke angles are identified as effective means to control wrinkle amplitude safely by increasing the number of peaks. Additionally, these intermediate paths mitigate thinning issues in the final product. The process can be more flexible, to produce a wider range of shapes, and to form more challenging materials.

X

Keywords: metal spinning process, wrinkle defect, finite element modeling, toolpath design

TABLE OF CONTENTS

Page

LIST OF TABLES

Page

LIST OF FIGURES

Page

LIST OF SYMBOLS

Symbol	Units	Description
σ_{ij}	MPa	Stress tensor
σ_{rz}	MPa	Shear stress in rz direction
$\sigma_{\varphi z}$	MPa	Shear stress in rz direction
σ_{zz}	MPa	Normal stress in zz direction
ϵ_{rr}	MPa	Normal stress in rr direction
$\epsilon_{\varphi\varphi}$	MPa	Normal stress in φφ direction
$\gamma_{r\varphi}$	MPa	Shear stress in rφ direction
ν	-	Poisson's ratio
ω	Rad/s	Angular velocity
ρ	g/mm^3	Density
f	mm/rev	Feed rate
b	N	Body force
a	mm/s^2	Acceleration
$\vec{\alpha}$	rad/s^2	Angular acceleration vector
$\mathcal{F}_0$	-	The inertial frame
$\mathcal{F}_1$	-	The rotational frame
E	MPa	Young modulus
V_d	m/s	Dilatational wave
K	-	Strength coefficient
n	-	Hardening exponent
σ_{eff}	MPa	Effective stress
σ_Y	MPa	Yield stress
ϵ_p	MPa	Effective plastic strain
η	-	Triaxiality
D	-	Current damaged scalar
ΔD	-	Incremental damage scalar

$\epsilon_{failure}$	mm/mm	Failure strain
α	degree	Stroke angle

INTRODUCTION

Metal spinning, a manufacturing technique, involves the transformation of circular plates or discs into axisymmetrically shaped parts. These parts encompass a wide array of products, including funnels, hoppers, tank heads, bells, antenna reflectors, satellites, and musical instruments, among others. Commonly utilized materials in this process comprise steel, stainless steel, aluminum, brass, and bronze, with typical thicknesses ranging from 0.8 mm to 3.0 mm. The final dimensions of the spun parts typically span from a few millimeters to 1300 millimeters.

The fundamental elements of the metal spinning process include a circular plate (depicted in Figure 0.1a) that is to be shaped, a rotating mandrel (as illustrated in Figure 0.1b), a tailstock used for clamping the plate onto the mandrel (seen in Figure 0.1c), and a forming tool or roller (shown in Figure 0.1d). Through the concurrent movement of the roller (Figure 0.1f) and the rotational movement of the mandrel (Figure 0.1e), the initial flat plate undergoes transformation into an axisymmetric shape over the mandrel (depicted in Figure 0.1g).

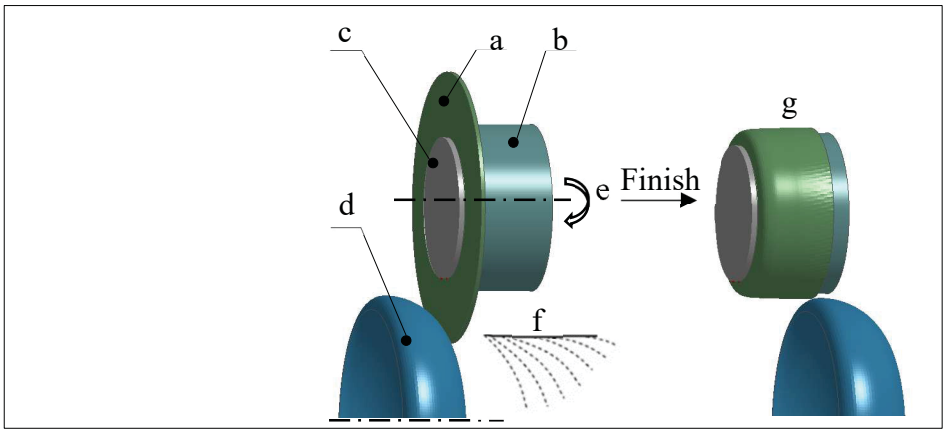

Figure 0.1 Metal spinning process, (a) a circular plate, (b) a mandrel, (c) a tailstock, (d) a roller, (e) mandrel rotation, (f) roller path, (g) final part

The geometry of the roller movement or roller path (toolpath), displayed in Figure 0.1f, contains numerous single paths required for a successful metal spinning process. A simple

straightforward path which follows the mandrel geometry usually turns out to be a failed process due to defects on the final products. Two types of defects are flange wrinkling and circumferential cracking.

The existing literature showed several gaps of current knowledge in the metal spinning mechanics: the development of the stress and strain history of the workpiece is only observed in the first path but they are not well understood in the rest, mainly due to the very long computational time of the numerical model with sufficient fine mesh; the development of residual stress and springback has not been investigated, either numerically or by experiment; the failure mechanism of metal spinning, cracking and wrinkling, are not fully understood; the design of toolpaths to make final parts without failure remains an art, and cannot be generated reliably. The evaluation of the current situation shows the great potential for innovation of the metal spinning process.

Objectives of this thesis:

This research aims to understand and explain the successful toolpath geometry of the metal spinning process so that it can be generated systematically instead of remaining intuitively.
The objective of this thesis is to advance the comprehension of the metal spinning process by addressing three key gaps in current knowledge:

1. Reducing Computational Time: Develop a novel numerical model aimed at significantly reducing computational time while ensuring the accuracy of the results.
2. Understanding Failure Mechanisms: Develop a comprehensive failure model to predict and analyze cracking occurrences during the metal spinning process. This analysis aims to reveal the underlying mechanisms behind such failures.
3. Optimizing Toolpath Design: Conduct an in-depth analysis of the numerical model results to determine the characteristics of successful toolpaths. This will facilitate the development of guidelines for designing toolpaths to achieve defect-free metal spinning operations.

Structure of thesis:

This thesis is composed of five chapters and is organized as follows:

Chapter 1 provides a literature review about the state of the art of the three main topics: the configuration of the numerical model; the failure mechanisms; the approaches for designing toolpaths. Then, the analysis and evaluation of these sources are reviewed. The gap knowledge in the current situation is presented.

Chapter 2 shows the methodology and short description of analysis performed in the next three chapters.

Chapter 3 presents an original approach addressed the topic: improvement of the numerical model in terms of computational time and accuracy. The plate, rotating on the mandrel, can be considered as rotating disc problem. Therefore, the numerical model of metal spinning process can be analyzed in the rotating frame. The theory of transformation from inertial frame to the rotating frame is provided. The new configuration of the finite element in the rotating frame is analyzed thoroughly. Finally, the benchmark of this new configuration is investigated.

Chapter 4 presents an additional feature of the numerical model about predicting the circumferential cracking. The GISSMO is implemented in the numerical model. The configuration is analyzed thoroughly. The result of the simulation provides an insight into the circumferential cracking phenomena of the metal spinning process.

Chapter 5 presents an original approach addressed the topic: failure mechanisms and guideline to design the toolpaths. The original approach is that the metal spinning process is analyzed for every rotation of the mandrel instead of only the end of the process. This theory is then validated with the current literature. Consequently, four new applications are presented: an

observation and analysis of post-wrinkling; a circumferential cracking formulation; a reliable guidelines of toolpaths designs; a relationship between toolpath and thickness of the final product.

CHAPTER 1

LITERATURE REVIEW

This chapter addresses three key issues, each requiring separate discussion:

1. Review of Numerical Models: Evaluation of the numerical model utilized for simulating the metal spinning process.
2. Mechanism of Defects: Examination of defect mechanisms, focusing on issues such as wrinkling and cracking.
3. State-of-the-Art Toolpath Design: Overview of current advancements and strategies in toolpath design.

1.1 Finite element modeling of the metal spinning process

Music et al (Music, Allwood, and Kawai, 2010a) produced an excellent review of the numerical methods used to simulate the spinning process up to 2010. They began with three studies of the simplified 2D-dimensional models with an assumption of axisymmetric deformation (Alberti, Cannizzaro, Lo Valvo, and Micari, 1989; Liu, Yang, and Li, 2002; Mori and Nonaka, 2004). This model had a very short computational time, but with poor accuracy. Next, they covered nine full 3D-dimensional models. These 3D models are mainly differentiated by their solvers or software (MSC (Awiszus and Härtel, 2011),(L. Li, Chen, Lu, Shu, Zhang, and Shen, 2023), Abaqus (Khamis Essa and Hartley, 2009; Gao, Yan, Li, Zhan, Ma, and Fu, 2022; Yu, Zhao, Du, Liu, and Evsyukov, 2020), LS-Dyna (Rentsch, Manopulo, and Hora, 2017)), their element types (solid (Awiszus and Härtel, 2011; Khamis Essa and Hartley, 2009; Yu, Zhao, Du, Liu, and Evsyukov, 2020), shell (Gao, Yan, Li, Zhan, Ma, and Fu, 2022; Rentsch, Manopulo, and Hora, 2017), or thick shell (Kong, Yu, Zhao, Wang, and Lin, 2017c)), their incorporation of the strain – hardening material law (the Hollomon law (Gao, Yan, Li, Zhan, Ma, and Fu, 2022; Kong, Yu, Zhao, Wang, and Lin, 2017c), power law (Khamis Essa and Hartley, 2009), or of the Ghosh law (Rentsch, Manopulo, and Hora, 2017)), and their time integration schemes (implicit(Quigley and Monaghan, 2002) or

explicit(Awiszus and Härtel, 2011; Khamis Essa and Hartley, 2009; Gao, Yan, Li, Zhan, Ma, and Fu, 2022; Rentsch, Manopulo, and Hora, 2017)). One article (Nguyen, Champliaud, and Lê, 2020) integrated the generalized incremental stress state dependent damage model (GISSMO) into a numerical simulation of the process to predict the circumferential cracking defect by measuring a damaged scalar D, in which failure at $D = 1$.

Recent FE models of the metal spinning process (Awiszus and Härtel, 2011; Härtel and Laue, 2016; Liu, 2007; Marghmaleki, Beni, Noghrehabadi, Kazemi, and Abadyan, 2011; Marghmaleki and Beni, 2014; Zhan, Yang, Zhang, Xu, and Ma, 2007) defined the rotation of mandrel by means of boundary condition as constant angular velocity over time. Then, the circular plate is driven to rotate by the pressure applied from the tailstock to the mandrel.

The disadvantage of these conventional 3D models is that they require an excessive amount of computational time to perform a single toolpath. Therefore, these models may not be practical to use for predicting the final shape of a product or for optimizing a roller path where numerous toolpaths are required to form a product. Some observations related to computational time are given below.

Firstly, a widely accepted assumption is that the only deformable part in the spinning process is the plate. The remaining parts, including the roller, backplate, and mandrel are considered as rigid bodies. Therefore, most of the time is invested in the plate and the rigid bodies require much less time to compute.

Secondly, the plate in the spinning process is rotating at a high speed. If there was only a rotating plate in the process without any contact with the mandrel or the roller, this would be a rotating disc problem (Nguyen, Champliaud, and Lê, 2018) which could be modeled as a static problem in a rotating reference frame where the plate is fixed, and the rotating speed is converted to a centrifugal force.

1.2 Metal spinning process failure: wrinkling and cracking

The most common defects in the spinning process are wrinkling, circumferential crack and radial crack. However, the wrinkling is the only failure which has been conducted so far by some authors such as (Chen, Gao, Zhan, Ma, Zhang, and Xu, 2019a; Kong, Yu, Zhao, Wang, and Lin, 2017a) . On the review of spinning process (Music, Allwood, and Kawai, 2010b), the circumferential crack can be observed intuitively by the high tensile radial stress. The Finite Element method is used to analysis the circumferential crack observed in the experiment of one - path conventional spinning process. This phenomenon is presented in Figure 1.2 where the plate suffered to the complete circumferential crack which create two separated parts after failure. The experimental configuration is showed in Figure 1.1. The roller deforms the 2mm thick aluminum plate at a clearance of 10mm away from the mandrel.

In the literature of predicting material failure, there are three common approaches which are based on the maximum effective plastic strain, Gurson yield criterion and the Generalized Incremental Stress State dependent damage model (GISSMO).

In case of failure prediction based on the maximum effective plastic strain, the material is considered as failure when the effective plastic strain reaches a critical value. The critical value usually is the maximum true plastic strain obtained from the tensile test. The failure sets on if the effective plastic strain reaches the maximum true plastic strain. However, these terms are defined in Appendix I and Appendix II by an assumption that the material is isochoric meaning the volume is constant during deformation. This assumption is only applied for plastic deformation. In the other hand, the fracture is pressure - dependent. Therefore, these terms are not properly defined beyond the plastic hence they cannot be used to assess the failure of the material.

The Gurson yield criterion is the micromechanical model which is described by nucleation, growth, and coalescence of micro voids (Needleman and Tvergaard, 1984). This model uses the alternative yield function which applied for both plastic stage and damage stage. Therefore, the plastic model must be replaced by the Gurson model hence the predefined plastic model cannot be chosen freely for example as anisotropic plasticity, etc. This is a disadvantage of the Gurson yield criterion.

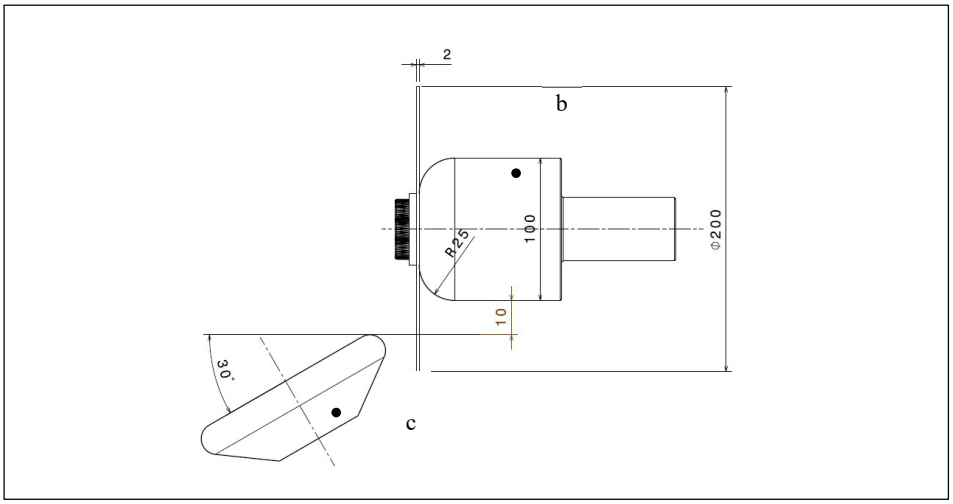

Figure 1.1 Experiment configuration, (a) a plate; (b) a mandrel; (c) a roller

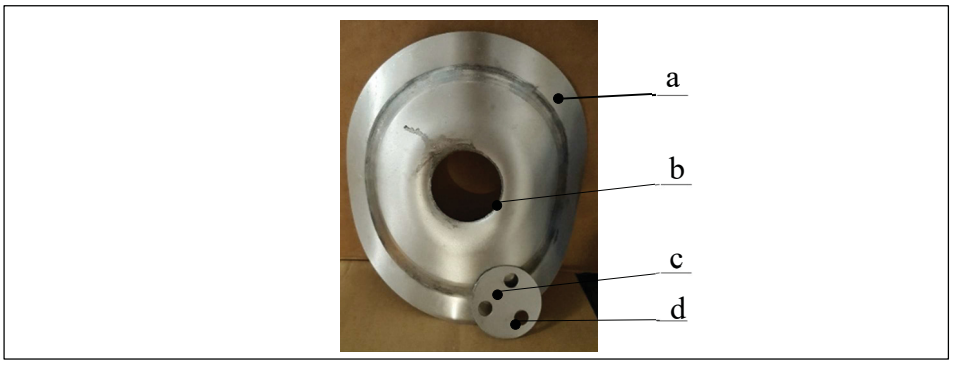

Figure 1.2 Circumferential crack; (a) the plate; (b) circumferential crack line; (c) failure part; (d) tailstock mounted hole

The material model called GISSMO, developed by (F Neukamm, Feucht, Haufe, and Roll, 2008; Frieder Neukamm, Feucht, and Haufe, 2009), introduces the damage parameter in the

material which can fully describe the material softening and fracture. In addition, this model resolves Gurson's disadvantage which is independent of the plasticity formula. This model has been widely used in the crashworthiness and forming process simulation (A. Haufe M. Feucht, P. DuBois and T. Borvall, 2010; Effelsberg, Haufe, Feucht, Neukamm, and Bois, 2012).

Li et al. (L. Li, Chen, Lu, Shu, Zhang, and Shen, 2023), Abd-Alrazzaq et al. (Abd-Alrazzaq, Ahmed, and Younes, 2018), and Xia et al. (Y. Xia, Shu, Zhu, and Li, 2020) studied the influential parameters of the spinning process using experiments on a computer numerical control (CNC) machine. They first present the most significant parameters and then explain how they optimized those parameters for minimum radial spinning force and tangential spinning force, which are considered as maximum spinning efficiency. The optimum quality was obtained by using a large number of rollers passes at a high-speed ratio.

Watson et al. (Michael Watson and Long, 2014), (M. Watson, Long, and Lu, 2015) investigated the wrinkling failure mechanics by means of finite element simulation. The plastic hinge on the flange causes the wrinkling failure initiation. At the wrinkling initiation, the magnitude of a bending moment and the elastic strain energy is lower.

Kong et al. (Kong, Yu, Zhao, Wang, and Lin, 2017c) found two stable compressive stress rings on the flange. The first one is distributed at the roller location and the second is in the middle of the flange. The second stress ring is likely the cause of flange wrinkling. Therefore, a double curved surface, representing the outer flange, buckling prediction model, based on the energy method, can be used to predict severe flange wrinkling. The average compressive stresses calculated in the FEM model and in the buckling model are compared to detect wrinkling defects.

Kong et al. (Kong, Yu, Zhao, Wang, and Lin, 2017b) found that the compressive stress on the outer edge causes a slight wrinkling defect, which has little effect on the quality of the final

part and can be smoothed out. However, the compressive stress on the inner part causes a severe wrinkling defect, which is not able to be recovered.

Chen et al. (Chen, Gao, Zhan, Ma, Zhang, and Xu, 2019b) proposed an analytical wrinkling defect model based on the fact that the flange diameter is reduced, and its volume is consistent throughout the spinning process. Therefore, the strain and the stress of the flange can be calculated analytically without the need for an FEM model. Subsequently, the wrinkling defect is detected by comparison of this stress to the critical circumferential stress.

Chen et al. (Chen, Zhan, Gao, Ma, and Zhang, 2021) found that the specific zone affected by the roller causes the flange to wrinkle in that zone instead of the whole flange. The authors proposed a theoretical model of the annular sector instead of the annular plate.

Li et al. (Z. H. Li and Long, 2022) proposed an analytical model integrating a toolpath design for wrinkle prediction. The wrinkling wave function, defined with a deforming depth variable, combined with the consistent volume, helps to calculate the critical stress that indicates wrinkle initiation. Therefore, this approach does not require a finite element method (FEM) model.
The wrinkling mechanism is caused by the excessive circumferential stress on the flange. Most of the studies considered that the complete flange circumferential stress is the cause of wrinkling. However, one researcher (Chen, Zhan, Gao, Ma, and Zhang, 2021) observed that only one section of the flange influences this defect.

While the roller path can be designed by the wrinkling predictive model with the objective of avoiding wrinkle initiation, a minor wrinkle flange can be smoothed out, as observed by (Kong, Yu, Zhao, Wang, and Lin, 2017b) and (Z. H. Li and Long, 2022). Some prediction models show that a higher forming depth can be that would avoid wrinkling (Z. H. Li and Long, 2022). Therefore, the idea that a wrinkle can be eliminated after wrinkle initiation can be a possible option for roller path design.

Summary effect of process parameters on wrinkle defection

Increased feed rates have been identified as a contributing factor to the premature onset of wrinkles. (Kong, Yu, Zhao, Wang, and Lin, 2017c) observed that wrinkles manifested earlier when employing a higher feed rate of 2 mm/rev at a stroke angle of 45° compared to a stroke angle of 40° with a feed rate of 1 mm/rev. Similarly, (Wang and Long, 2011) reported that the absence of wrinkles was ensured when the feed rate remained below 1.9 mm/rev for a 2mm thick steel workpiece; however, this investigation exclusively focused on the first path, leaving the impact of feed rate on subsequent paths unexplored.

In the realm of path patterns, the rotational path was found to pose a heightened risk of wrinkling according to the findings of (Hayama, Kudo, and Shinokura, 1970). (Sugita and Arai, 2015) corroborated these results, demonstrating that the utilization of a rotational path pattern increased the likelihood of wrinkles, while a translational path pattern led to circumferential cracks.

Furthermore, the research by (K Essa and Hartley, 2010) indicated that the initial workpiece diameter exerts minimal influence on wrinkle formation. Contrarily, (Wang and Long, 2011) noted that thinner workpiece thickness correlated with an increased likelihood of failure, ultimately resulting in wrinkling.

Summary effect of process parameters on crack and tearing

(Wang and Long, 2011) identified that employing a low feed rate may induce circumferential cracks on the workpiece surface.

(Hayama, Kudo, and Shinokura, 1970) observed that utilizing a translational path pattern elevates the risk of tearing in the spinning process. Conversely, they found that employing a mixed involute path pattern yields optimal results, mitigating the likelihood of tearing.

Additionally, research conducted by (Q. Xia, Shima, Kotera, and Yasuhuku, 2005) revealed that a high spinning ratio, defined as the ratio between the initial workpiece diameter and the final product diameter, increases the susceptibility to tearing during spinning operations.

Summary effect of process parameters on thinning

The feed rate parameter, particularly when set to a low value, is recognized as a determinant factor in inducing thinning of the workpiece material, as noted by (Wang and Long, 2011). Further reinforcing this observation, (El-Khabeery, Fattouh, El-Sheikh, and Hamed, 1991) demonstrated that lower feed rates corresponded to higher levels of thinning. Specifically, experimental investigations spanning feed rates ranging from 0.25 to 1 mm/rev resulted in thinning up to 25% in the initial path. Similarly, (Šugár, Šugárová, and Petrovič, 2016) reported comparable outcomes, with feed rates ranging from 0.5 to 1.5 mm/rev resulting in thinning up to 10% across multiple paths.

Regarding path geometries, concave paths are associated with the most pronounced thinning effects, while convex paths exhibit mitigated thinning tendencies. (Wang and Long, 2011) observed that the initial path induces twice as much thinning compared to subsequent paths.

In terms of overall failure modes, (Hayama, Kudo, and Shinokura, 1970) found that concave involute paths offer superior resistance against various failure modes, including wrinkling, tearing, and thinning. This finding aligns with the work of Liu (2007), who similarly concluded that concave involute paths result in the smallest and most uniform stress and strain distributions, contributing to enhanced structural integrity during spinning operations.

Several factors have been identified as contributing to specific defects in metal spinning process:

1. Wrinkles: Higher feed rates, rotational path patterns, and smaller workpiece thicknesses have all been associated with increased wrinkle formation.
2. Circumferential Cracks: Slower feed rates, translational path patterns, and higher spinning ratios have been found to increase the occurrence of circumferential cracks.
3. Thinning: Lower feed rates and concave path geometry have been shown to lead to increased thinning of the workpiece material.

1.3 Toolpath design

Utilizing a straightforward tool-path, as outlined in Figure 1.3, aligned with the mandrel's contours, can result in two types of defects: flange wrinkling, shown in Figure 1.4a and Figure 1.4b and circumferential cracking, shown in Figure 1.4c and Figure 1.4d.

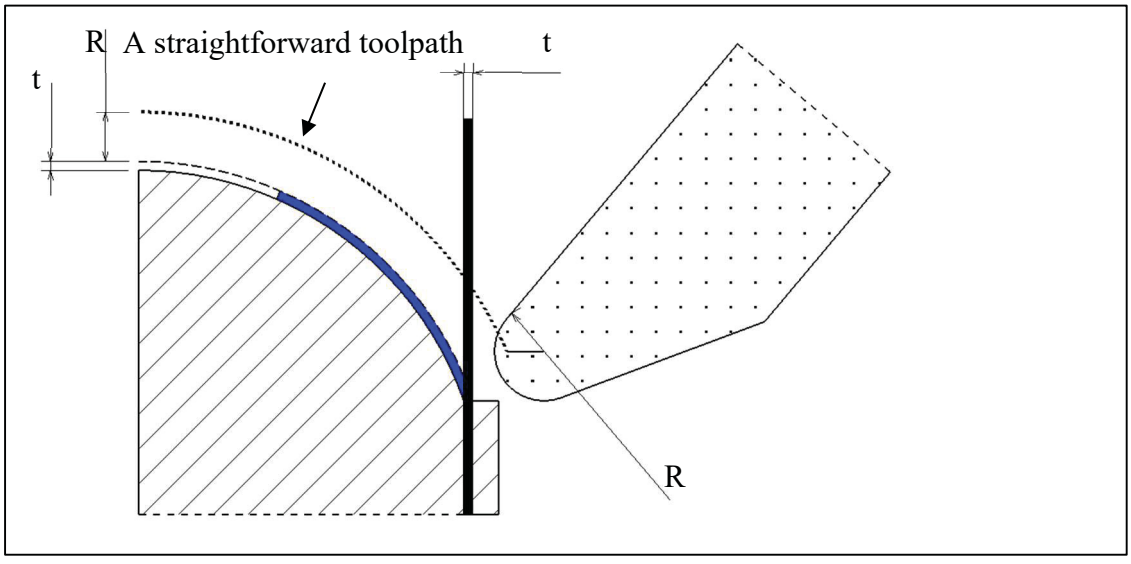

Figure 1.3 A straightforward toolpath demonstration

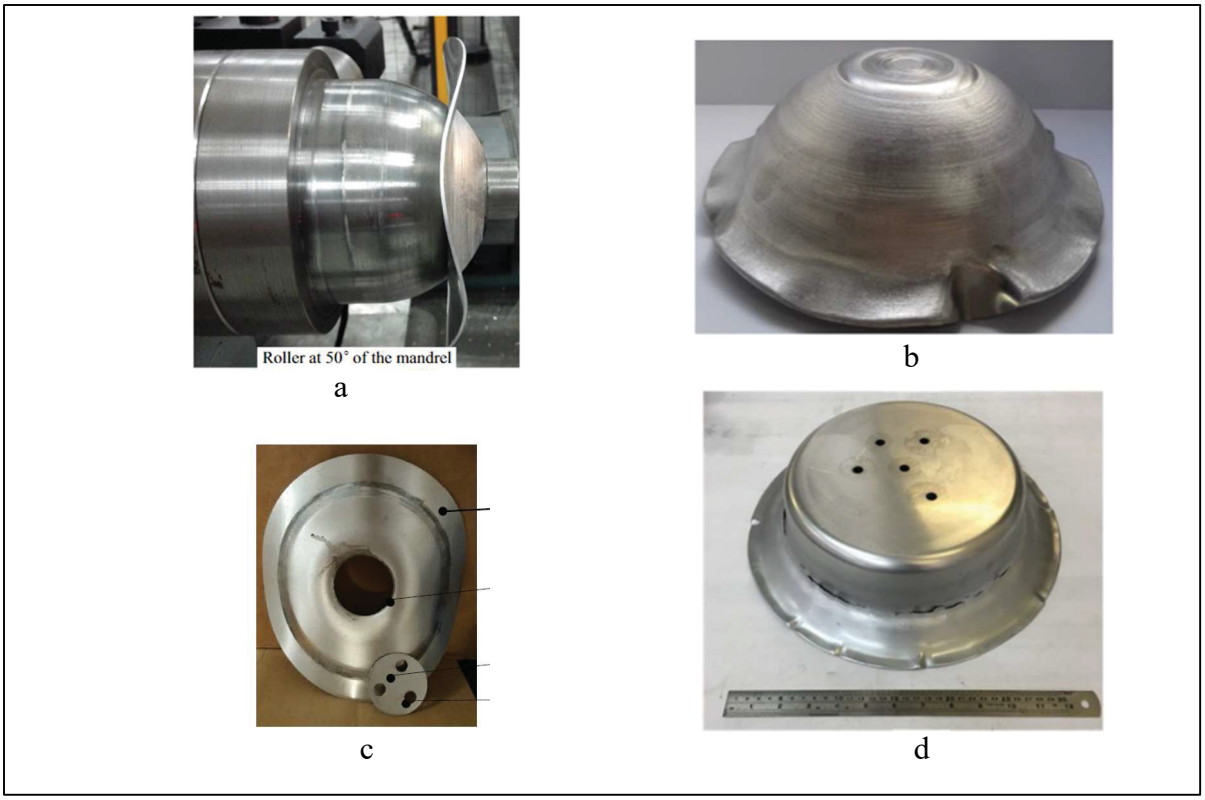

Figure 1.4 Metals spinning process defects: (a) wrinkle during process, (b) wrinkle of the final part, (c), (d) Circumferential cracking

Taken from (a) Kong (2017, p. 59); (b) Kong (2017, p. 3595); (c), (d) Nguyen (2020, p. 166)

Figure 1.5 shows successful toolpath geometries and associated forces, gathered from experienced spinners employing the modern tool arrangement. A total of 16 paths are delineated, spanning the entire process. Primarily linear, the paths encompass a variety of profiles. Notably, Path 9 and Path 11 entail a combination of convex and linear segments. Obviously, these paths are lacking optimization in terms of path geometry and the total numbers of paths employed.

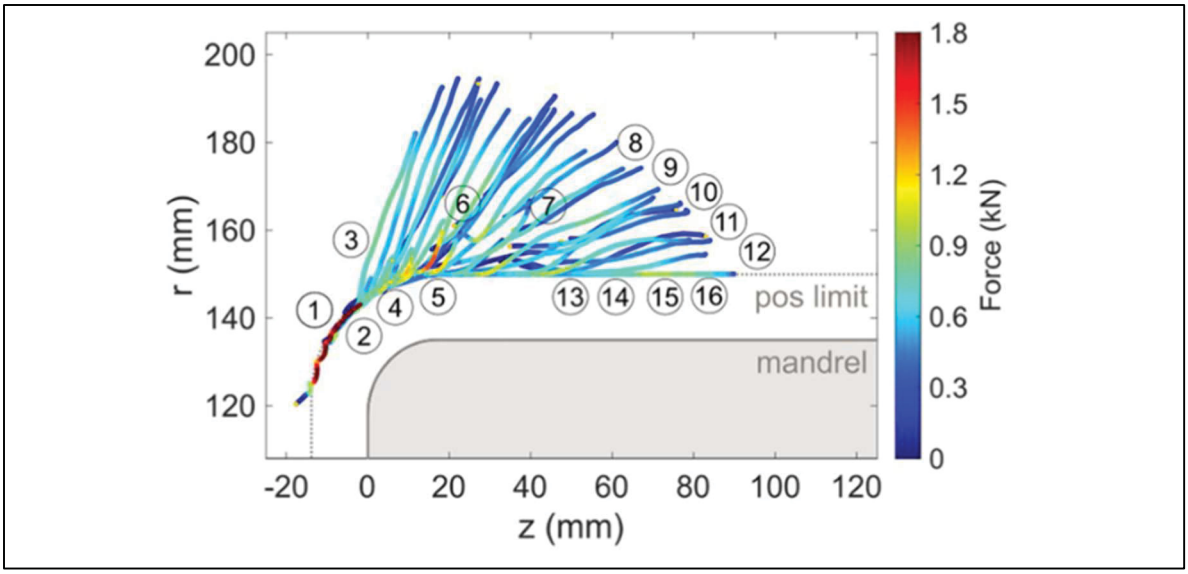

Figure 1.5 Recorded toolpaths and forces of spinners

Taken from Russo (2021, p. 12)

A specialized tool known as the spinning arrangement tool is necessary to create the movement of the roller. The earliest version of this arrangement, shown in Figure 1.6a, comprises a tool rest featuring various holes, a support pin, and a spinning tool. However, this setup is limited to producing translational path patterns governed by circular formulas, with a fixed pitch length between adjacent holes. While effective in certain scenarios, its applicability is constrained.

In contrast, the modern tool arrangement showcased in Figure 1.6b introduces an additional level arm capable of traversing along the tool rest, facilitating greater versatility. The roller is affixed to this level arm, enabling the creation of a hybrid of rotational and translational path patterns, thereby expanding the scope of achievable geometries, and enhancing process flexibility.

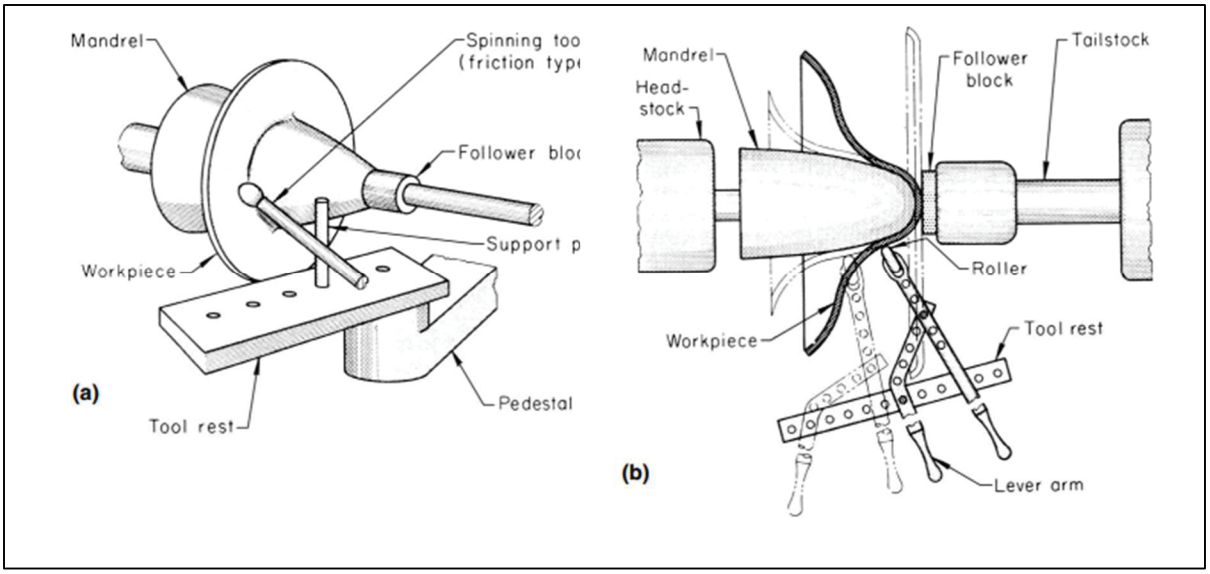

Figure 1.6 Typical arrangements for manual spinning using a lathe. (a) Simple arrangement with a friction type spinning tool. (b) More complex setup using levers and a spinning roller

Taken from Semiatin (2006, p. 369)

The toolpaths in metal spinning typically consist of multiple sequential paths, each defined by specific geometries, path numbers, and corresponding feed rates. The feed rate, measured in millimeters per revolution (mm/rev), indicates the distance the roller travels during one revolution of the mandrel. Path geometries, as illustrated in Figure 1.7, encompass linear curves, concave curves, and convex curves. Movement of the roller can be forward, from the mandrel towards the edge of the plate or the flange, or backward, in the opposite direction from the flange towards the mandrel.

Sequential paths can be categorized into three main patterns:

1. Rotational Pattern: In this pattern, the roller initiates from a fixed point on the mandrel and follows a sequential path with a continuously decreasing stroke angle $\Delta\alpha$, as depicted in Figure 1.8 [A] and [B].
2. Translational Pattern: Paths in this pattern utilize a fixed stroke angle β, and each path maintains a consistent distance pitch p, as shown in Figure 1.8 [D].

3. Mixed Pattern: This pattern combines elements of both rotational and translational patterns. Each path maintains the same distance pitch p and experiences a decreased stroke angle Δα, as illustrated in Figure 1.8 [C].

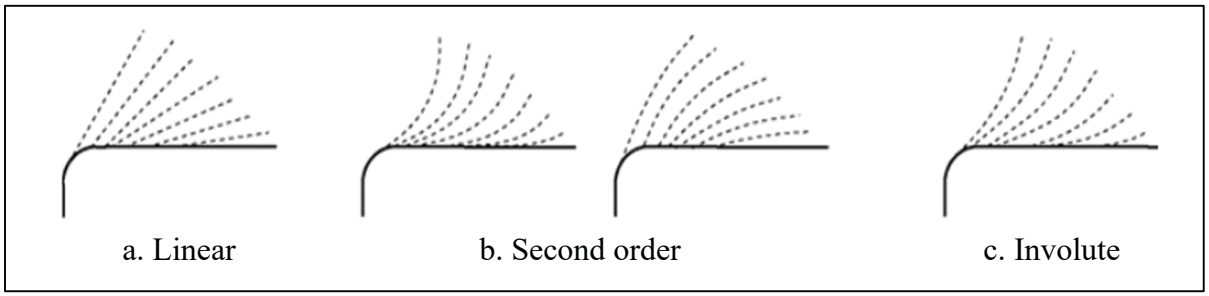

Figure 1.7 Toolpath design options
Taken from Music (2010, p. 20)

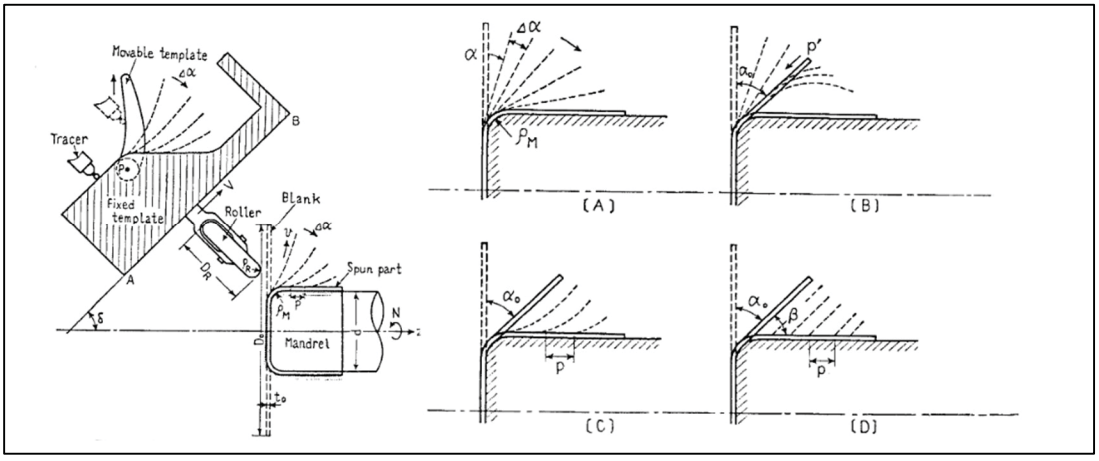

Figure 1.8 Sequential path patterns. [A], [B]: rotational pattern; [C], [D]: translational pattern
Taken from Hayama (1970, p. 1359)

The study conducted by (Hayama, Kudo, and Shinokura, 1970) identified the concave involute curve [C], depicted in Figure 1.8, as the optimal profile based on experimental findings. This pattern demonstrated superior performance in terms of the ability to freely control the height

of cups and achieve a limit drawing ratio of 2.5, surpassing the common limit drawing ratios of 1.8 to 1.85 observed with other patterns, as well as deep drawing with conical dies.

While the empirical study conducted by (Hayama, Kudo, and Shinokura, 1970) successfully identified the most effective multiple path pattern for metal spinning, there remain notable gaps in our understanding of the metal spinning process:

1. Absence of Force and Workpiece Shape Consideration: Pre-defined toolpaths often overlook crucial factors such as force dynamics and workpiece shape variations. These oversights can limit the applicability and adaptability of identified optimal patterns across different scenarios.
2. Limited Validation Scope: The results obtained from empirical studies like (Hayama, Kudo, and Shinokura, 1970) may be limited to specific configurations, including geometry, material composition, and thickness of the workpiece. Consequently, the generalizability of these findings to broader contexts may be uncertain.
3. Incomplete Approach to Tool-Path Optimization: Despite numerous studies exploring various configurations such as mandrel geometry, tool feed rate, and workpiece characteristics, there remains a lack of comprehensive methodologies for automatically generating optimized toolpaths. Existing research efforts often fail to integrate diverse variables into a unified framework for achieving optimal results.

Addressing these knowledge gaps requires a comprehensive approach that considers factors beyond pre-defined toolpaths, incorporates a broader range of experimental configurations for validation, and develops comprehensive methodologies for optimizing tool-path generation across diverse metal spinning scenarios.

The study by (Russo, Cleaver, and Allwood, 2021) aimed to capture and parameterize the skills of experienced metal spinners through the use of a haptic spinning system, as depicted in Figure 1.9. Six skilled artisans, each with between 10 to 40 years of metal spinning experience, participated in over 70 experimental trials. By analyzing their speech and actions, the study

formulated seven principles, which were then parameterized using six path parameters. These path parameters include the average plastic strain, the shape of the undeformed workpiece, the number of backward passes, the position of maximum force, the feed ratio, and the concavity of the paths. Notably, the study emphasized that relying solely on path geometry is insufficient for successfully executing the metal spinning process and advocated for the integration of force and shape control. The results of the study revealed that tool forces are highest near the mandrel and decrease as the tool moves away from it. Additionally, the majority of paths exhibited linear geometries, with some incorporating convex elements. The origin of the paths was observed to translate along the shape of the mandrel, while the stroke angle of the paths increased. Despite the complexity and diversity of the multiple toolpaths analyzed (totaling 16 paths), the study suggests that there is still room for improvement in generating more effective toolpaths compared to those executed manually by skilled spinners.

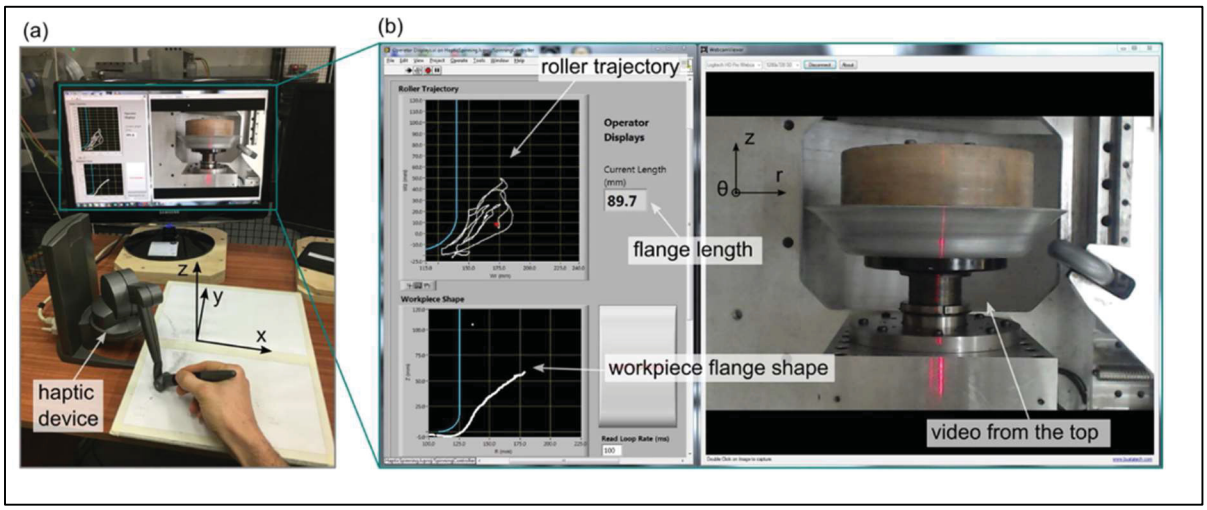

Figure 1.9 A haptic device for recording the action of spinner
Taken from Russo (2021, p.6)

The study by (Kleiner, Göbel, Kantz, Klimmek, and Homberg, 2002) employed statistical design of experiments to design toolpaths, operating under the assumption of circular-shaped paths with variable radii of curvature. Their primary objective was to minimize wrinkle grades,

ranging from 1 to 6, although thinning was not a considered factor. This approach necessitates a significant number of experiments to be conducted for each new mandrel shape, workpiece material, thickness, and diameter. By systematically varying these parameters and analyzing their effects on wrinkle formation, Kleiner et al. sought to optimize the toolpaths for enhanced manufacturing outcomes. Despite its effectiveness in minimizing wrinkles, this methodology's reliance on extensive experimentation poses practical challenges in terms of time, resources, and scalability for diverse production scenarios.

(Polyblank and Allwood, 2015) introduced a novel approach to toolpath design by integrating finite element (FE) modeling into a closed-loop control strategy. Their methodology involves modeling the toolpath using either a quadratic Bezier curve or involute paths, both of which are controlled by three points. Through FE simulation, the location of these points is adjusted iteratively to optimize the toolpath. However, this optimization process can be computationally intensive and time-consuming. Each adjustment necessitates running an FE simulation to completion, resulting in a timeframe ranging from hours to months to find an optimized toolpath. Despite its potential to yield highly optimized toolpaths, the significant computational burden associated with this approach may limit its practical applicability in real-time or high-throughput manufacturing environments.

In their recent study, (Z. H. Li and Long, 2022) presented an innovative approach to wrinkle prediction in metal spinning processes by integrating an analytical model with toolpath design. Unlike finite element method (FEM) approaches, this method does not rely on complex numerical simulations. Instead, it utilizes a wrinkling wave function, which is defined with a forming depth variable, to calculate the critical stress indicative of wrinkle onset. However, it's important to note that the analytical model employed in this approach necessitates several assumptions, potentially more than those required by FEM approaches. Some of these assumptions include neglecting friction between the tool and workpiece and assuming a pre-defined deformed geometry based on constant thicRkness and volume consistency. While this analytical approach offers computational efficiency and simplicity compared to FEM simulations, the validity of its predictions may be influenced by the accuracy of these

assumptions. Further validation and refinement of the analytical model may be necessary to enhance its predictive capabilities and broaden its applicability in real-world metal spinning processes.

In conclusion, the literature has identified four different approaches aimed at understanding and designing reliable multiple toolpaths:

1. Parameterization of Human Skill: This approach involves the identification of six parameters utilized in the design of multiple toolpaths based on human expertise.
2. Empirical Experimentation: Studies employing empirical experimentation have determined that the involute geometry represents the optimal pattern for multiple toolpaths.
3. Analytical Wrinkle Model with Effective Roller Path: This approach focuses on the development of an analytical wrinkle model coupled with an effective roller path to mitigate wrinkling during the metal spinning process.
4. Optimization Solver Based on Surrogate Model: Utilizing optimization solvers based on surrogate models, this approach seeks to optimize multiple toolpaths efficiently.

However, the toolpaths design still remains as an art and a vast area of research.

CHAPTER 2

METHODOLOGY

Chapter 1's literature review has provided an overview of the current understanding, theories, and methodologies utilized to characterize the metal spinning process. Notably, the toolpath geometry is an interesting aspect, which often relies on the intuition and expertise of skilled spinners. This research aims to understand and explain the successful toolpath geometry of the metal spinning process, thereby enabling its systematic rather than relying solely on intuition.

To address this aim, four distinct approaches have been undertaken to investigate toolpath geometry, each yielding unique insights:

1. Empirical Experimentation: Previous studies have highlighted the concave involute profile as an optimal pattern; However, precise parameters for this profile remain undetermined.
2. Analytical Wrinkle Model: This approach utilizes a wrinkle model based on instability theory, where forming depth emerges as a critical variable. Nonetheless, analytical methods necessitate certain assumptions, such as zero thickness strain and neglected friction.
3. Optimization Solver Based on Surrogate Model: While this method has identified the concave involute profile as a favorable outcome, computational time proves to be a significant limitation.
4. Parameterization of Human Skill: Consideration of tool forces and flange shape by skilled spinners has also been explored. However, the toolpath geometry generated by skilled spinners may not always be optimal.

The literature review has revealed a consensus regarding the concave involute profile as the optimal pattern for wrinkle-free spinning. Nonetheless, a discrepancy exists in determining the

geometry: while the analytical wrinkle model focuses on the forming depth variable measured at the process's end, the parameterization of human skill adjusts the toolpath continuously based on tool forces and flange shape measured during the process. This research opts for the latter approach to further probe toolpath geometry. Additionally, observations indicate that workpiece flanges may exhibit wrinkles during the process, although they may be smoothed out eventually in some instances. Consequently, there is a pressing need to investigate these phenomena during the process. Therefore, the methodology used in this thesis is included in three steps as listed below:

1. Develop an efficient numerical model aimed at significantly reducing computational time while ensuring the accuracy of the results.
2. Develop a comprehensive failure model to predict and analyze cracking occurrences during the metal spinning process. This analysis aims to reveal the underlying mechanisms behind such failures.
3. Conduct an in-depth analysis of the numerical model results to determine the characteristics of successful toolpaths. This will facilitate the development of guidelines for designing toolpaths to achieve defect-free metal spinning operations.

Methodology of an efficient numerical model:

Based on treating the plate as a rotating disc problem, a new model is configured in the commercial simulation software LS Dyna. By default, this software does not explicitly support the configuration of the spinning process in a rotating reference frame. Therefore, the strong form of the spinning process must be formulated in the rotating reference frame. The mandrel movement, the plate boundary condition, and the roller path must all be adapted to this new frame as shown in Figure 2.1. The advantages of this configuration compared to the conventional configuration are discussed later in terms of its ability to obtain better accuracy and to reduce the computational time. The result of thickness distribution is compared to the experiment and to a conventional numerical model. Two new techniques are proposed for this model to obtain a convergent and accurate result with a shorter computing time. This implementation and validation are presented in CHAPTER 3.

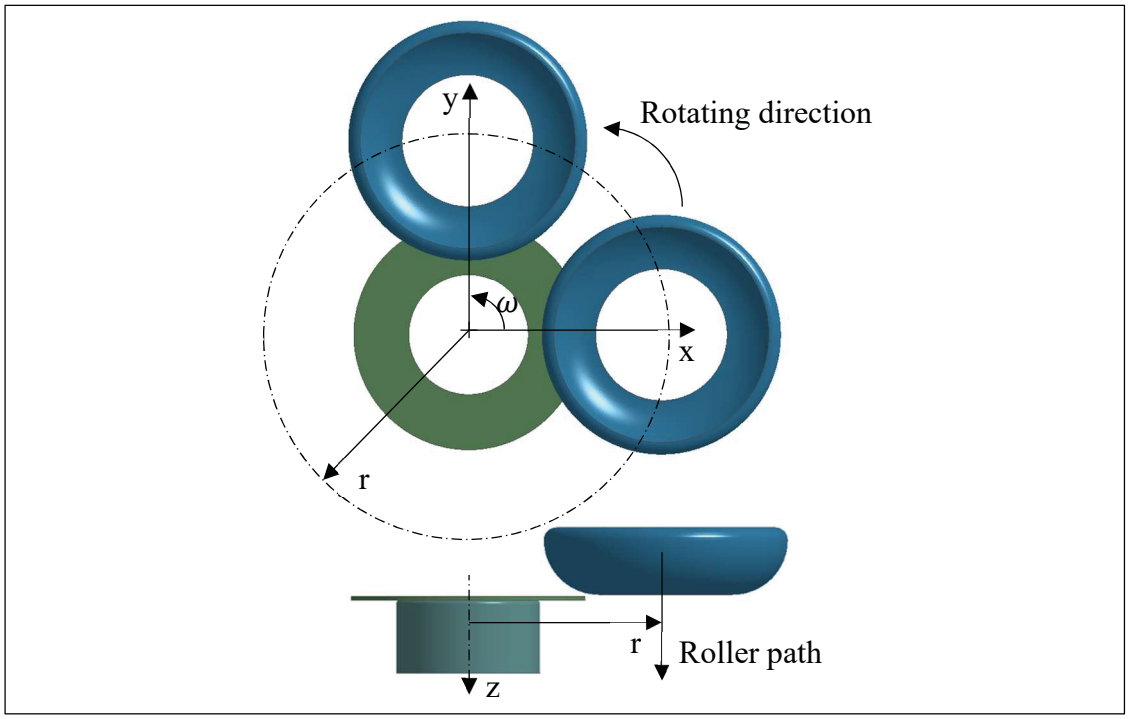

Figure 2.1 Equivalent kinematic of numeric model in a rotating reference frame

Methodology of failure model

By critical review of three common approaches, used to predict material failure, the GISSMO method is used to simulate the circumferential cracking in the metal spinning process. This implementation and validation are presented in CHAPTER 4.

Methodology of analysis numerical model result

The thesis proposes a novel approach to address these challenges, wherein the toolpath is constructed by multiple linear segments. Each segment has a length of the feed rate mm/rad which every one rotation 2π radiant of the mandrel causes the roller to move a straight-line

millimeter. The analysis of the spinning process in one full rotation is presented in CHAPTER 5.

CHAPTER 3

FINITE ELEMENT MODELING OF THE METAL SPINNING PROCESS IN A ROTATING REFERENCE FRAME

Part of chapter published in "30th European Modeling and Simulation Symposium" in September, 2018

Part of chapter published to "Journal of Manufacturing and Materials Processing" in January, 2024.

The development of Finite Element Model of the metal spinning process is composed of two three parts:

- Firstly, the chapter presents the study of the rotating disc (initial plate) problems with specific boundary conditions encountered in the metal spinning process.
- Secondly, the formal transformation from the inertial frame to the rotating reference frame is presented. This new mathematical approach is successfully applied in the simulation of the metal spinning process. In addition, new techniques related to FEM configuration are presented, including mesh sizing based on a minimized aspect ratio, a mesh convergence study, and a feed rate scale.
- Thirdly, the advantages of this configuration compared to the conventional configuration are discussed later in terms of its ability to obtain better accuracy and to reduce the computational time. The result of thickness distribution is compared to the experiment and to a conventional numerical model. Two new techniques are proposed for this model to obtain a convergent and accurate result with a shorter computing time.

3.1 Analysis of rotating disc problem

3.1.1 Analytical solution

The disc can be assumed as a plane stress problem due to the small ratio between thickness and the other dimensions. The material behavior is represented by Hooke's law. It is more convenient to study the rotating disc in the cylindrical coordinate system as in Figure 3.1.
The stresses σ_{rz}, $\sigma_{\varphi z}$, σ_{zz} are equal to zero in the plane stress assumption. The relation of stresses and strains in case of Hooke's law is defined as:

$$\begin{bmatrix} \epsilon_{rr} \\ \epsilon_{\varphi\varphi} \\ \gamma_{r\varphi} \end{bmatrix} = \frac{1}{E}\begin{bmatrix} 1 & -\nu & 0 \\ -\nu & 1 & 0 \\ 0 & 0 & 2(1+\nu) \end{bmatrix}\begin{bmatrix} \sigma_{rr} \\ \sigma_{\varphi\varphi} \\ \sigma_{r\varphi} \end{bmatrix} \tag{3.1}$$

The constant angular velocity ω is converted to the centrifugal force or inertial force per unit volume (N/m^3) applied to the internal of the body.

$$F = \rho\omega^2 r \tag{3.2}$$

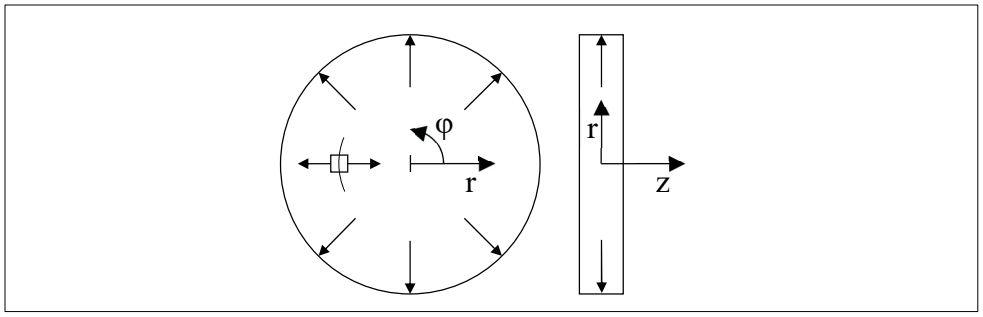

Figure 3.1 Plane stress problem in cylindrical coordinate system

The tailstock can be neglected by introducing an equivalent boundary condition assuming that zero deformation of material between the tailstock and mandrel thus the disc become a hollow geometry for the internal radius r_i is equal to the outer radius of the tailstock. With this

boundary conditions, the radial stress of outer boundary and displacements of inner boundary are zero. The complete boundary conditions are illustrated in Figure 3.2.

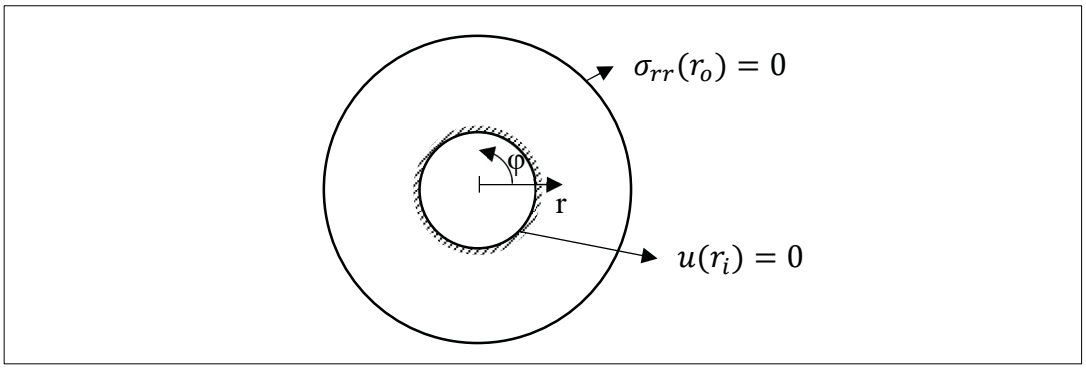

Figure 3.2 Boundary conditions of rotating disc problem

The analytical solution of this problem is given in (Bruhns, 2003).

$$\sigma_{rr}(r) = \frac{c_1}{r^2} + 2c_2 - \frac{3+\nu}{8}\rho\omega^2 r^2 \tag{3.3}$$

$$\sigma_{\varphi\varphi}(r) = -\frac{c_1}{r^2} + 2c_2 - \frac{1+3\nu}{8}\rho\omega^2 r^2 \tag{3.4}$$

$$u(r) = \frac{1}{E}\left[-(1+\nu)\frac{c_1}{r} + 2(1-\nu)c_2 r - \frac{1}{8}(1-\nu^2)\rho\omega^2 r^3\right] \tag{3.5}$$

With

ρ: Density (g/mm^3)

ν: Poisson's ratio

ω: Angular velocity (rad/s)

r: Radius (mm)

σ: Stresses (MPa)

c_1 , c_2: Parameters defined by boundary conditions

The parameters c_1 and c_2 can be found by applying two boundary conditions $\sigma_{rr}(r_o) = 0$ and $u(r_i) = 0$

$$c_1 = \frac{1}{8}(3+\nu)\rho\omega^2 r_o^4 - 2c_2 r_o^2 \tag{3.6}$$

$$c_2 = \left[\frac{(1+\nu)(3+\nu)\rho\omega^2 r_o^4}{8r_i} + \frac{(1-\nu^2)\rho\omega^2 r_i^3}{8}\right] / \left[\frac{(1+\nu)2r_o^2}{r_o} + 2(1-\nu)r_o\right] \tag{3.7}$$

3.1.2 Numerical solution

The numerical solution is carried out using the FE solver LS-Dyna. The one Gauss integration point solid element is used to model the disc since this is also the element type used for the metal spinning model presented in following sections. Meshes and boundary conditions of model are illustrated in Figure 3.3. The boundary conditions of nodes on the inner radius must assure a condition that is free movement in thickness direction as a plane stress property. The implicit time integration of one timestep of one millisecond is used for alternative of static solver. The elastic material is used for presenting Hooke's law.

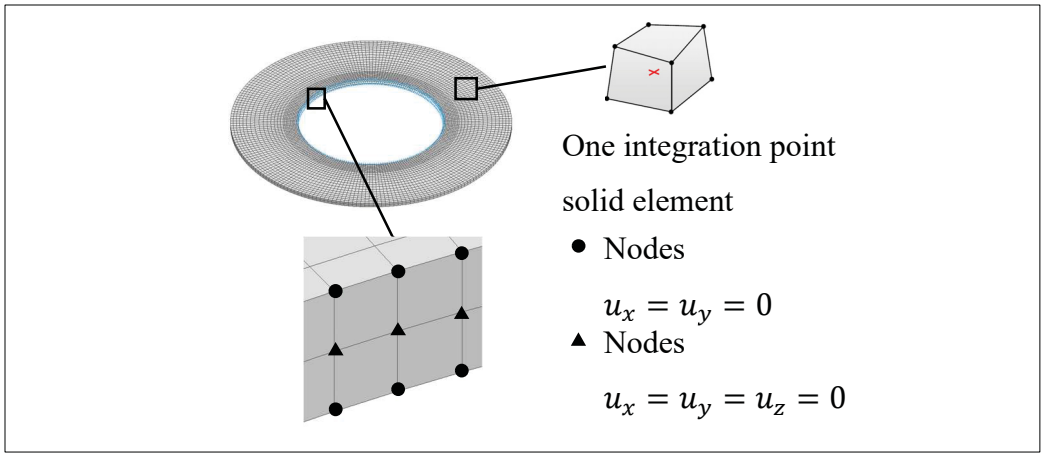

Figure 3.3 Mesh and boundary condition for solid element model

3.1.3 Verification

Parameters are taken from a real metal spinning process setup. The angular speed of disc is 200 rpm or 20.94 $\mathrm{rad/s}$. The aluminum A 1100-O has density of 2.7E-3 $\mathrm{g/mm^3}$, Poisson ratio is 0.33. The inner and outer radius are 50 mm and 96 mm respectively.

The stresses distribution on the disc are showed in Figure 3.4. The maximum principal stress and second principal stress at Gauss points of elements are compared to the analytical solution described in a previous section. The trend of both radial and circumferential stresses of the analytical are displayed in Figure 3.5. The radial stress obtains a maximum value at the inner boundary and decreases gradually to zero at the outer boundary. The circumferential stress peaks at the radius of 62.9 mm.

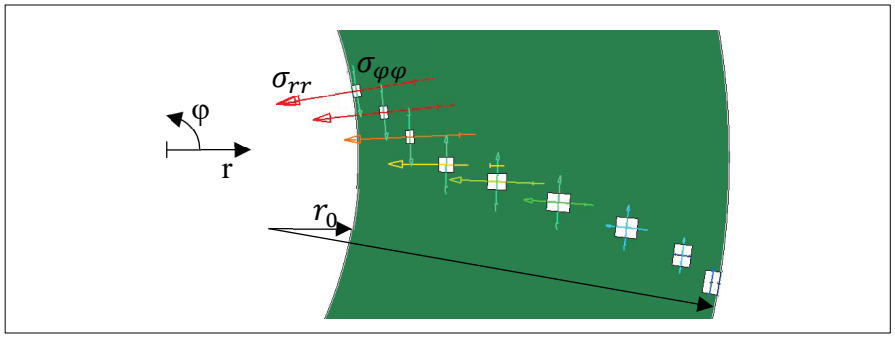

Figure 3.4 Stresses distribution on disc

The maximum error between analytical and numerical solution is just 0.0167 percent thus it cannot be distinguished on the diagram. The Table 3.1 and Table 3.2 show the analytical, numerical and error value of radial and circumferential stresses at Gauss points. In conclusion, the numerical model can compute exact results for the rotating disc problem.

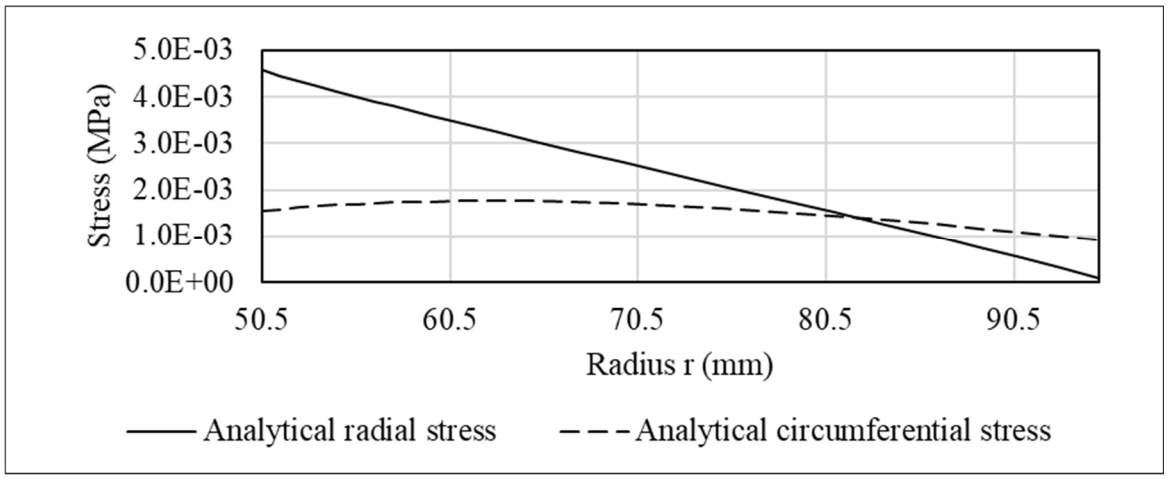

Figure 3.5 Stresses in rotating disc problems

The rotating disc problem can be used as a based finite element model to simulate a full metal spinning process by adding contact pressure of the roller on disc. The following section describes the kinematics of a revolving roller around a fixed mandrel.

Table 3.1 Radial stresses of analytical and numerical solution at Gauss points

r (mm)	Analytical σ_{rr} (MPa)	Numerical σ_{rr} (MPa)	Error (%)
50.5	4.58E-03	4.58E-03	1.67E-01
51.5	4.46E-03	4.47E-03	1.67E-01
52.5	4.34E-03	4.35E-03	1.66E-01
…	…	…	…
91.0	5.22E-04	5.22E-04	1.13E-01
93.1	3.05E-04	3.05E-04	8.54E-02
95.0	1.00E-04	9.99E-05	-5.09E-02

Table 3.2 Circumferential stresses of analytical and numerical solution at Gauss points

r (mm)	Analytical $\sigma_{\varphi\varphi}$ (MPa)	Numerical $\sigma_{\varphi\varphi}$ (MPa)	Error (%)
50.5	1.55E-03	1.55E-03	1.8E-01
51.5	1.59E-03	1.59E-03	1.1E-01
52.5	1.62E-03	1.62E-03	1.6E-01
…	…	…	…
91.0	1.08E-03	1.08E-03	8.4E-02
93.1	9.90E-04	9.91E-04	1.3E-01
95.0	9.01E-04	9.02E-04	5.6E-02

3.2 Simulation of metal spinning process based on proposed configuration

The circular disc is made from the commercial pure aluminum A1100-O with properties taken from (Inc, 2010) as in Table 4.1.

The material model is isotropic elastoplastic using a power law hardening rule (see plot of Equation (3.8), showed in Figure 3.7).

$$\sigma_t = K\epsilon_t^n \tag{3.8}$$

With

σ_t: True stress

ϵ_t: True strain

K: Strength coefficient

n: Strain hardening coefficient

Table 3.3 Aluminum A1100-O properties

Young modulus	E = 68.9 GPa
Yield offset	0.002
Yield strength at offset	$\sigma_y = 34.5$ MPa
Engineering ultimate tensile strength	EUTS = 89.6 MPa
Mass density	2.7E-6 kg/mm^3

Two parameters K and n can be found by using two conditions showed in Figure 3.6 that satisfy the yield engineering strength at offset and zero tangent slope of the engineering stress – strain curve at engineering ultimate strain. The values of K and n are 0.1636 and 0.2594 respectively.

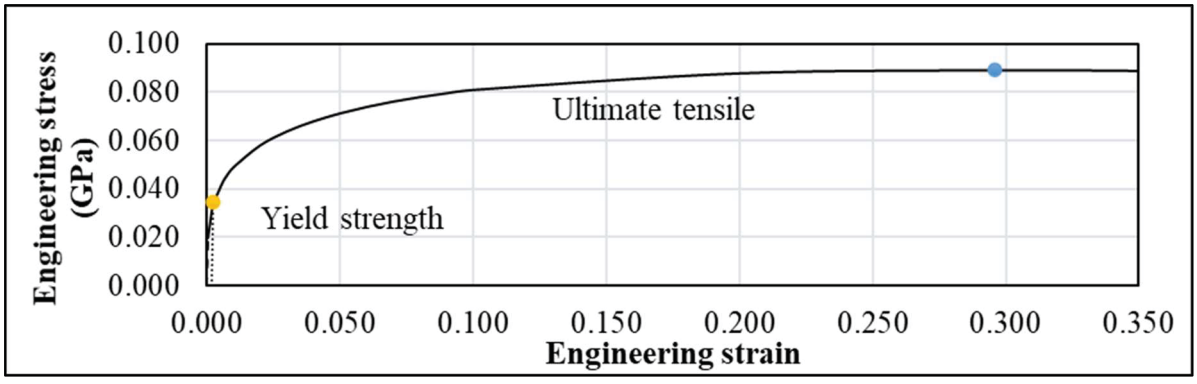

Figure 3.6 Engineering stress-strain curve A1100-O

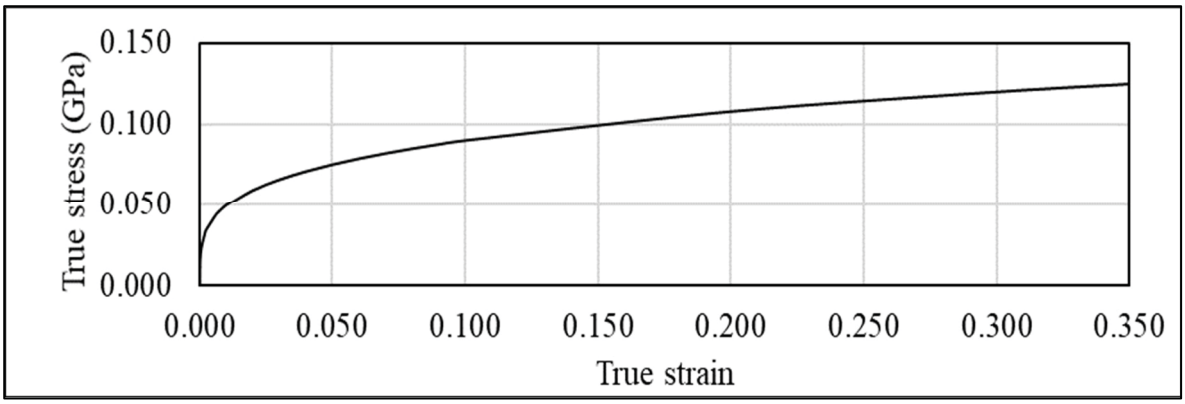

Figure 3.7 True stress-strain curve

The contact one - way surface to surface is used for computing the contact pressure between the disc and mandrel as well as the disc and roller. This contact type assures the zero penetration one – way from slave surface to master surface. The disc is chosen for slave surface and the other are master surface.

The simulation uses an explicit time integration scheme. Different time steps, 1E-3, 4E-3, 9E-3, 2E-2 millisecond, are studied to determine the convergence of maximum axial force. The results of conventional model and the proposed model are compared about the value of maximum axial force and run time.

The maximum axial forces of both models converged to the value of 2875N, but it comes from opposite directions, with the conventional model overestimating the axial force until it reaches the converged value and the proposed model underestimating it until convergence. A Figure 3.8 shows directions and speed of convergence for both models. It is clear that the proposed model got convergent value at time step 4E-3 ms, while the conventional model needs a time step of 1E-3 ms with the difference to the previous time step is about 1.63 percent. These values are presented in Table 3.4. Additionally, the computational time is nearly 4-times faster for a 4E-3 ms time step with 18h in comparison with 68h on a ZBook 15 core i7-4800MQ 2.7 GHz laptop.

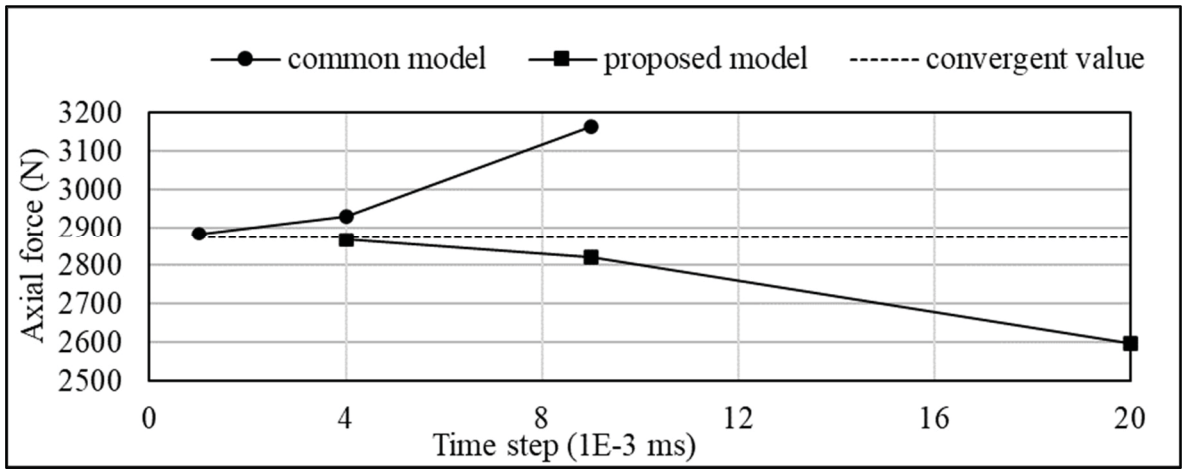

Figure 3.8 Time step convergence

Table 3.4 Convergence of maximum axial force and runtime

Δt	Conventional model; % change	Proposed model; % change	Runtime
1E-3	2883; -1.57%	N/A	68h16
4E-3	2929; -7.45%	2867; 1.63%	18h09
9E-3	3165	2821; 8.66%	8h27
2E-2	N/A	2596	3h43

The advantages of the proposed approach in case of metal spinning process are the displacement of deformable disc is almost in the z direction. On the other hand, the deformed part in conventional model includes additional displacement in xy plane due to rotation.

3.3 Formulation of a plate in a rotating frame

The equation of motion in an inertial frame is written as

$$\frac{\partial \sigma_{ij}}{\partial x_j} + b_i = \rho a_i \tag{3.9}$$

Which ij is the Einstein notation.

σ_{ij} are stresses.

b_i are the body forces.

a_i are accelerations.

ρ is the density.

These parameters are expressed in an inertial frame, but while the stresses σ and density ρ are independent of the frame, the two other parameters, accelerations a, and body forces b, are dependent on the reference frame. In the case of the spinning process, the body forces, caused by gravity, can be neglected. Therefore, acceleration is the only parameter that needs to be derived in the rotational frame. Acceleration is the derivative of velocity with respect to time, and velocity is the derivative of displacement with respect to time; the displacement, velocity and acceleration therefore need to be derived in order.

Figure 3.9 shows an arbitrary point P on the plate in the inertial frame $\mathcal{F}_0$ and in the rotational frame $\mathcal{F}_1$. The velocity and acceleration of this point are calculated in the rotational frame $\mathcal{F}_1$ from the inertial frame $\mathcal{F}_0$, shown below.

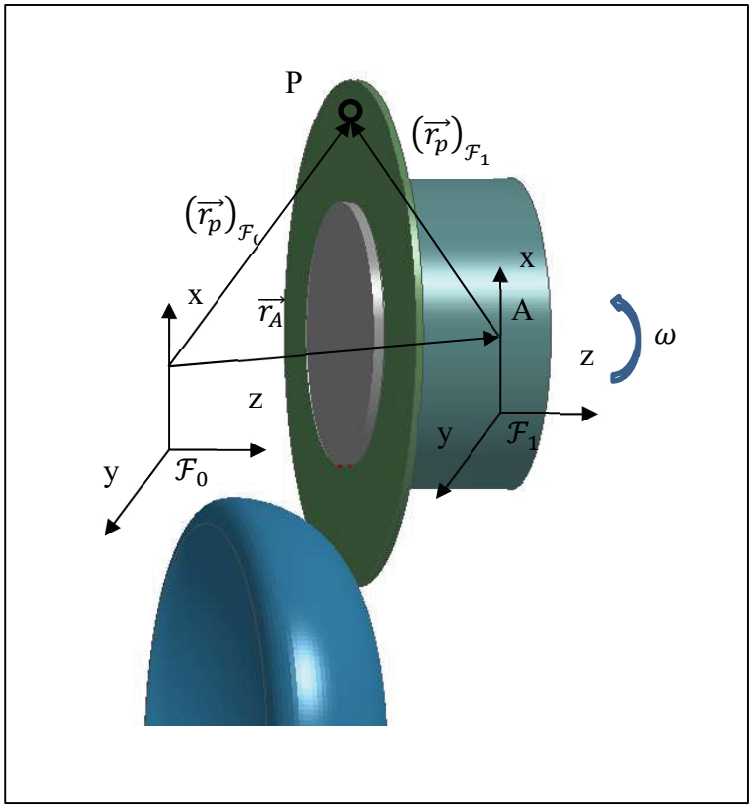

Figure 3.9 Inertial frame $\mathcal{F}_0$ and rotating frame $\mathcal{F}_1$

A point P on the plate is described by a vector $(\vec{r_p})_{\mathcal{F}_0}$ in the inertial frame and by a vector $(\vec{r_p})_{\mathcal{F}_1}$ in the rotational frame. Two vectors are related together by the vector connecting two frames $\vec{r}_A$

$$(\vec{r_p})_{\mathcal{F}_0} = \vec{r}_A + (\vec{r_p})_{\mathcal{F}_1} \tag{3.10}$$

The velocity of a point in the inertial frame $\vec{v}_{\mathcal{F}_0}$ is the derivative versus time of its position.

$$\begin{aligned} (\vec{v}_p)_{\mathcal{F}_0} = \frac{d}{dt}\left((\vec{r_p})_{\mathcal{F}_0}\right) &= \frac{d}{dt}\left(\vec{r}_A + (\vec{r_p})_{\mathcal{F}_1}\right) \\ &= \underbrace{\frac{d}{dt}(\vec{r}_A)}_{=0} + \frac{d}{dt}(\vec{r_p})_{\mathcal{F}_1} \end{aligned} \tag{3.11}$$

When the position between two frames is fixed, then the derivative of vector $\frac{d}{dt}(\vec{r}_A) = 0$. Hence, the only unknown term is the derivative of the position P versus time $\frac{d}{dt}\left(\overrightarrow{r_p}\right)_{\mathcal{F}_1}$. The vector $\left(\overrightarrow{r_p}\right)_{\mathcal{F}_1}$ can be decomposed according to a unit vector referenced in the rotational frame.

$$\left(\overrightarrow{r_p}\right)_{\mathcal{F}_1} = p_x\overrightarrow{e_x} + p_y\overrightarrow{e_y} + p_z\overrightarrow{e_z} \tag{3.12}$$

Taking the derivative of equation (3.12)

$$\frac{d}{dt}\left(\overrightarrow{r_p}\right)_{\mathcal{F}_1} = \underbrace{\dot{p}_x\,\overrightarrow{e_x} + \dot{p}_y\overrightarrow{e_y} + \dot{p}_z\overrightarrow{e_z}}_{(\vec{v}_p)_{\mathcal{F}_1}} + \underbrace{p_x\overrightarrow{\dot{e}_x} + p_y\overrightarrow{\dot{e}_y} + p_z\overrightarrow{\dot{e}_z}}_{\vec{\omega}\times(\vec{r}_p)_{\mathcal{F}_1}} \tag{3.13}$$

Substituting equation (3.13) in equation (3.11), the relationship between the velocities described in the two different reference frames F0 and F1 can be written as

$$\left(\vec{v}_p\right)_{\mathcal{F}_0} = \left(\vec{v}_p\right)_{\mathcal{F}_1} + \vec{\omega} \times \left(\vec{r}_p\right)_{\mathcal{F}_1} \tag{3.14}$$

Which $\vec{\omega}$ is the angular velocity vector.

The last step is the derivation of the expression of the acceleration.

$$\begin{aligned}
\left(\vec{a}_p\right)_{\mathcal{F}_0} &= \frac{d}{dt}\left(\left(\vec{v}_p\right)_{\mathcal{F}_1} + \vec{\omega} \times \left(\vec{r}_p\right)_{\mathcal{F}_1}\right) \\
&= \frac{d}{dt}\left(\left(\vec{v}_p\right)_{\mathcal{F}_1}\right) + \frac{d}{dt}\left(\vec{\omega} \times \left(\vec{r}_p\right)_{\mathcal{F}_1}\right) \\
&= \frac{d}{dt}\left(\left(\vec{v}_p\right)_{\mathcal{F}_1}\right) + \vec{\alpha} \times \left(\vec{r}_p\right)_{\mathcal{F}_1} \\
&\quad + \vec{\omega} \times \frac{d}{dt}\left(\left(\vec{r}_p\right)_{\mathcal{F}_1}\right)
\end{aligned} \tag{3.15}$$

$\vec{\alpha}$ is the angular acceleration vector. The last term was calculated using equation (3.13), and so the only remaining unknown term is the first one $\frac{d}{dt}\left(\left(\vec{v}_p\right)_{\mathcal{F}_1}\right)$. The velocity of a point P in rotating frame $(\vec{v}_P)_{\mathcal{F}_1}$ can be decomposed using a unit vector:

$$(\vec{v}_P)_{\mathcal{F}_1} = \dot{p}_x\overrightarrow{e_x} + \dot{p}_y\overrightarrow{e_y} + \dot{p}_z\overrightarrow{e_z} \tag{3.16}$$

Let's take a derivative of the equation (3.16)

$$\frac{d}{dt}(\vec{v}_P)_{\mathcal{F}_1} = \underbrace{\ddot{p}_x\,\overrightarrow{e_x} + \ddot{p}_y\overrightarrow{e_y} + \ddot{p}_z\overrightarrow{e_z}}_{(\vec{a}_P)_{\mathcal{F}_1}} + \underbrace{\dot{p}_x\overrightarrow{\dot{e}_x} + \dot{p}_y\overrightarrow{\dot{e}_y} + \dot{p}_z\overrightarrow{\dot{e}_z}}_{\vec{\omega}\times(\vec{v}_P)_{\mathcal{F}_1}} \tag{3.17}$$

Substituting equation (3.17) and equation (3.13) in equation (3.15), the relation of the accelerations between two frames can be written as

$$\left(\vec{a}_p\right)_{\mathcal{F}_0} = (\vec{a}_P)_{\mathcal{F}_1} + 2\vec{\omega}\times(\vec{v}_P)_{\mathcal{F}_1} + \vec{\alpha}\times(\vec{r}_P)_{\mathcal{F}_1} + \vec{\omega}\times\left(\vec{\omega}\times(\vec{r}_P)_{\mathcal{F}_1}\right) \tag{3.18}$$

Finally, the equation of motion becomes

$$\frac{\partial\sigma_{ij}}{\partial x_j} = \rho\left((\vec{a}_P)_{\mathcal{F}_1} + 2\vec{\omega}\times(\vec{v}_P)_{\mathcal{F}_1} + \vec{\alpha}\times(\vec{r}_P)_{\mathcal{F}_1} + \vec{\omega}\times\left(\vec{\omega}\times(\vec{r}_P)_{\mathcal{F}_1}\right)\right) \tag{3.19}$$

The quantities vector and location of the point P are now represented in the rotating frame $\mathcal{F}_1$. There are three new terms: the Coriolis force $2\vec{\omega}\times(\vec{v}_P)_{\mathcal{F}_1}$, the Euler force $\vec{\alpha}\times(\vec{r}_P)_{\mathcal{F}_1}$ and the centrifugal force $\vec{\omega}\times\left(\vec{\omega}\times(\vec{r}_P)_{\mathcal{F}_1}\right)$.

3.4 Formulation of the new toolpath in the rotating frame.

The roller is modeled as a rigid body. Therefore, the roller path is described by its center point. The displacement of this point is the difference between two locations at two instants t and t_0 and is written as

$$\vec{u}_{\mathcal{F}_1}^{(t)} = \vec{r}_{\mathcal{F}_1}^{(t)} - \vec{r}_{\mathcal{F}_1}^{(t_0)} \tag{3.20}$$

The se two terms expressed in the rotating frame can be described in the inertial frame $\mathcal{F}_0$ as

$$\vec{r}_{\mathcal{F}_1}^{(t)} = \bar{\bar{R}}\vec{r}_{\mathcal{F}_0}^{(t)} \tag{3.21}$$

Which $\bar{\bar{R}}$ is the rotational matrix

$$\bar{\bar{R}} = \begin{bmatrix} cos\omega t & sin\omega t & 0 \\ -sin\omega t & cos\omega t & 0 \\ 0 & 0 & 1 \end{bmatrix} \tag{3.22}$$

The initial location in frame $\mathcal{F}_1$ can be chosen so that the two frames have the same origin. Therefore, $\vec{r}_{\mathcal{F}_1}^{(t_0)} = \vec{r}_{\mathcal{F}_0}^{(t_0)}$. Finally, the displacement formula of the roller can be transferred to the rotating reference frame.

$$\vec{u}_{\mathcal{F}_1}^{(t)} = \bar{\bar{R}}\vec{r}_{\mathcal{F}_0}^{(t)} - \vec{r}_{\mathcal{F}_0}^{(t_0)} \tag{3.23}$$

The only dynamic part in the process is the roller whose movement can be divided into two components. The first component is the rotation ω about mandrel's axis with the same angular velocity as mandrel's speed. The second component is the movement of a roller path which is a combination of radial direction r on xy plane and stroked direction z. The velocity in z

direction is the feed rate. The radial direction r is constant if the roller path is a straight line. The illustration of this kinematics is showed in Figure 3.10.

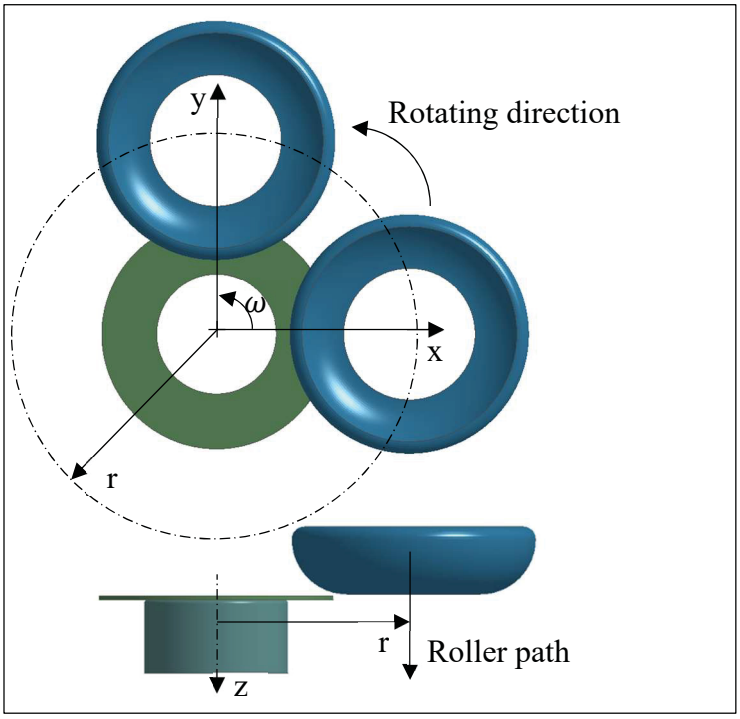

Figure 3.10 Equivalent kinematic of proposed model

3.5 Finite element model of a new spinning approach in LS-DYNA

3.6 Inefficiency of the rotating boundary condition of a plate in a conventional configuration

The popular approach to reduce computational time i.e., via a larger time step size, is to assume that the process is quasi-static so that two techniques, mass scaling and loading rate scaling, can be applied to maintain the quasi-static status that can be respected if the ratio of kinetic energy to internal energy is less than 10% and impact tool speed is less than 1% of the material dilatational wave speed (Smith, 2020).

The dilatational wave speed is defined as below.

$$V_d = \sqrt{\frac{E(1-\nu)}{(1+\nu)(1-2\nu)\rho}} \tag{3.24}$$

in which E is the elasticity modulus,

ν: Poisson's ratio, and

ρ: is the density.

The properties of common metals are summarized in Table 3.5.

Table 3.5 Bulk wave speeds in solids (Ravi-Chandar, 2004)

Material	Elasticity E (GPa)	Poisson's ratio ν	Density ρ (kg/m^3)	Dilatational wave speed V_d (m/s)
High strength steel	200	0.3	7.8	5875
Tungsten and alloys	406	0.3	13.4	6386
Aluminum alloys	70	0.3	2.7	5908

There are two places of contact in the spinning process, the speed of the rotational boundary condition V_c and the speed of the impact between the roller and the plate V_z. Therefore, the scaling is limited by two conditions C_1 and C_2 for V_c and V_z respectively.

The speed of the rotational boundary condition V_c is also called the circumferential speed of the inner radius of the plate, shown in Figure 3.11.

$$V_c = 2\pi R_{in} \times \frac{\omega}{60 \times 1000}\ (m/s) \tag{3.25}$$

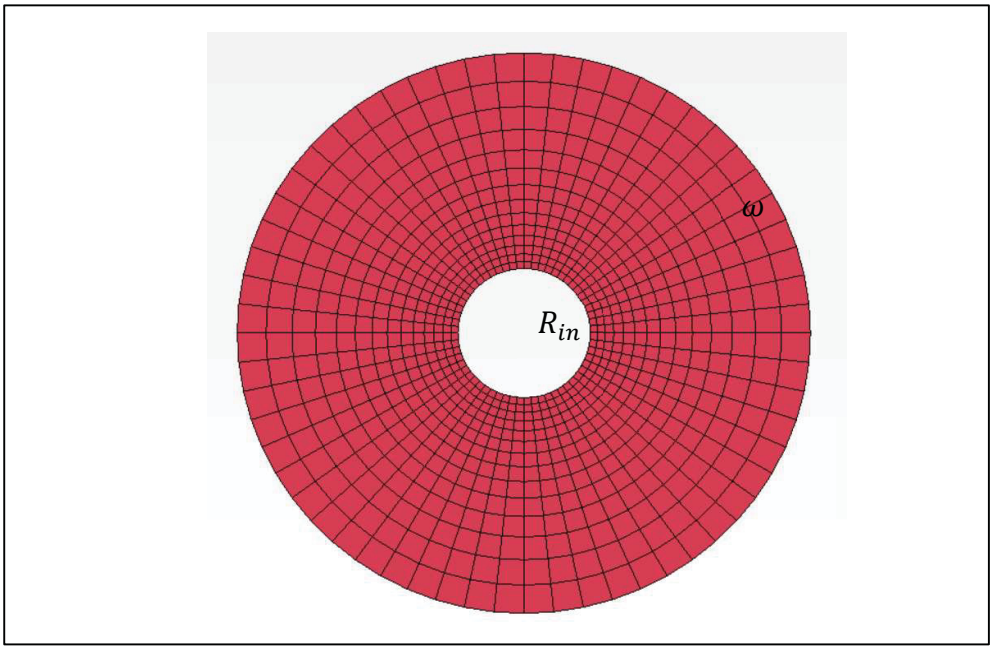

Figure 3.11 Conventional rotating boundary condition of a rotating plate

The other condition is the speed of impact between the roller and the plate V_z. The roller slides on the surface of the plate in the circumferential direction and in the radial direction, hence the effect of the roller on the plate in the circumferential direction is neglected because a very small friction effect occurs, as the roller is rotating around its own axis. The only noteworthy speed is in the stroke or z direction. The speed of this stroke is calculated by the rotating speed (rpm) multiplied by the feed rate (mm/rev).

$$V_z = \frac{\omega}{60} \times \frac{f}{1000} (m/s) \tag{3.26}$$

In loading rate scaling, the rotating speed of the mandrel ω is scaled up by a multiplier α to become the artificial rotating speed $\omega_a = \alpha\omega$. Therefore, the rotational speed becomes artificially $V_{ca} = \alpha V_c$ and the axial speed also becomes $V_{za} = \alpha V_z$. The constraint that the impact speed over the dilatational speed be smaller than 1%, must be satisfied.

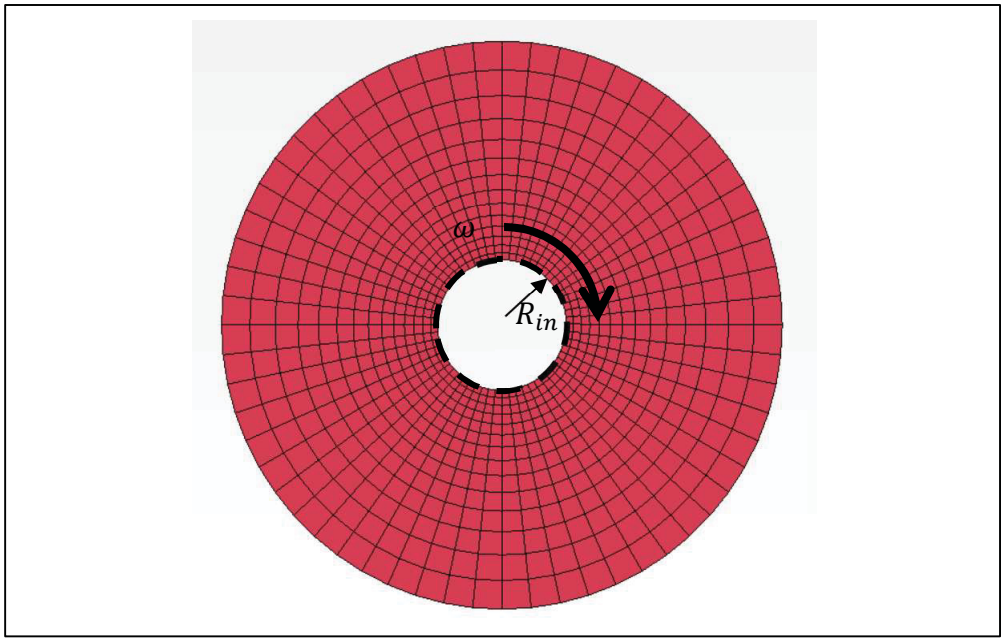

Figure 3.12 Conventional rotating boundary condition of a rotating plate

The first condition of rotational speed gives a limitation C_1 for the multiplier α.

$$\frac{V_{ca}}{V_d} = \alpha \frac{V_c}{V_d} < 0.01 \Leftrightarrow \alpha < 0.01 \frac{V_d}{V_c} = C_1 \tag{3.27}$$

The second condition of stroke speed also gives a limitation C_2.

$$\frac{V_{za}}{V_d} = \alpha \frac{V_z}{V_d} < 0.01 \Leftrightarrow \alpha < 0.01 \frac{V_d}{V_z} = C_2 \tag{3.28}$$

Therefore, the multiplier α is either smaller than C_1 or smaller than C_2.

The ratio $\frac{C_2}{C_1} = \frac{V_c}{V_z} = \frac{2\pi R_{in}}{f}$. In practice, the feed rate is often less than 1 $\mathrm{mm/rev}$ to reduce the wrinkles and the radius R_{in} depends on the dimension of the mandrel which is usually larger

than 1 mm. Therefore, the ratio $\frac{2\pi R_{in}}{f}$ is larger than 1 and so the condition C_2 is larger than condition C_1, $\frac{2\pi R_{in}}{f}$ times.

The potential increase of loading rate scaling is limited by the first condition C_1 in the case of a conventional model. In contrast, the new model does not have the first condition, hence the loading rate scaling can be applied as much as the value of condition C_2, which is much larger than condition C_1.

In mass scaling, the mass is scaled up by a multiplier β so the artificial density $\rho_a = \beta\rho$, or reducing dilatational speed.

$$V_{da} = \frac{V_d}{\sqrt{\beta}} \tag{3.29}$$

The first condition of rotational speed gives a limitation C_1 for the multiplier β.

$$\frac{V_c}{V_{da}} = \frac{V_c}{V_d}\sqrt{\beta} < 0.01 \Leftrightarrow \beta < \left(0.01\frac{V_d}{V_c}\right)^2 = C_1 \tag{3.30}$$

The second condition of stroke speed also gives a limitation C_2.

$$\frac{V_z}{V_{da}} = \frac{V_z}{V_d}\sqrt{\beta} < 0.01 \Leftrightarrow \beta < \left(0.01\frac{V_d}{V_z}\right)^2 = C_2 \tag{3.31}$$

Therefore, the multiplier β is either smaller than C_1 or smaller than C_2.

The ratio $\frac{C_2}{C_1} = \left(\frac{V_c}{V_z}\right)^2 = \left(\frac{2\pi R_{in}}{f}\right)^2$, and so the condition C_2 is larger than condition C_1, $\left(\frac{2\pi R_{in}}{f}\right)^2$ times.

The potential increase of mass scaling may also be limited by the first condition C_1 in the case of a conventional model. In contrast, the new model does not have the first condition, hence the mass scaling can be applied as long as condition C_2 is much larger than condition C_1.

3.6.1 Boundary condition

Based on the previous derivation of the strong form in the rotating reference frame, the mandrel and the backplate will be fixed. Therefore, the backplate does not need to be modeled and can be replaced by a fixed displacement of nodes at the outer diameter of the backplate as shown in Figure 3.13. These nodes are fixed by a LS-DYNA command "BOUDARY_SPC_SET" for six degrees of freedom x, y, z, rx, ry, rz.

The rotating speed of the mandrel is constant $\omega = const$, which means the acceleration is zero and so the Euler force is zero. The generalized body force includes the centrifugal acceleration: the Coriolis acceleration is applied to the plate.

The rigid body movement is applied by prescribing the "boundary_presribed_motion_rigid" LS-DYNA command with six parameters: the x, y, and z displacements and the rx, ry, rz rotations.

According to equation (3.23), there is an advantage when choosing the center of the roller so that it lies on the x-z plane where the y axis is zero. The explicit formula can be written in the matrix form.

$$\vec{u}_{\mathcal{F}_1}^{(t)} = \begin{bmatrix} r_x^{(t)} cos\omega t \\ r_x^{(t)} sin\omega t \\ r_z^{(t)} \end{bmatrix} - \begin{bmatrix} r_x^{(0)} \\ 0 \\ r_z^{(0)} \end{bmatrix} \tag{3.32}$$

This formula can be applied in LS-DYNA by a command “define_function”.

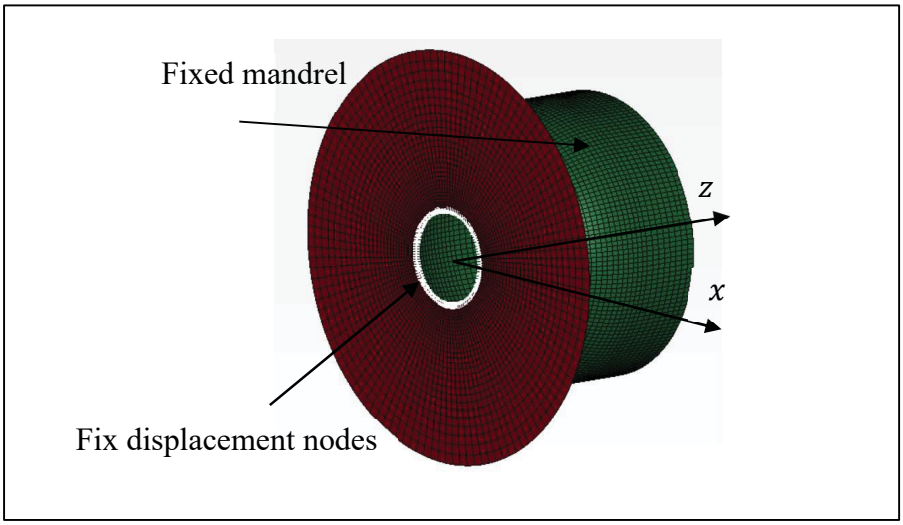

Figure 3.13 Boundary conditions of the plate and the mandrel

3.6.2 Material model and elements

The material is modeled using the plasticity power law $\sigma_y = k\epsilon^n$ where k is the strength coefficient and n is the hardening exponent; both are shown in Table 3.6. In the experiment, the thickness of the final product can be 18.33% smaller than the initial thickness. Therefore, the element’s formula should include the change in thickness. A shell formula with variable thickness was chosen for the model. A full integration gauss point was chosen because it responds very well to tensile tests compared to the reduced integration scheme, offering the same accuracy. Another advantage is that it does not require any additional element, and so the time step size is a benefit of this feature. The 4-node fully integrated shell element with thickness stretch is therefore chosen as equation (26) in LS-DYNA software.

Table 3.6 Mechanical properties of the Aluminum Alloy 2024-O

Young's modulus (GPa)	Poisson's ratio ν	Yield strength (MPa)	Strength coefficient (MPa)	Hardening exponent (n)
71.3	0.33	70.06	308.62	0.234

3.6.3 Loading rate scaling

If the material in the metal spinning process can be assumed to be quasi-static and non-rate dependent, the stroke speed of the roller can be increased without affecting the simulation results. The stroke of the roller moves in both the circumferential and the z direction. The circumferential speed relates to the rotating speed. The z speed relates to the feed ratio mm/rev and the rotating speed rev/minute, and so it has speed in mm/minute. Therefore, the rotating speed and/or the feed ratio can be used to increase the stroke speed. However, it is reported in the literature that the feed ratio plays an important role in flange wrinkling (Kong, Yu, Zhao, Wang, and Lin, 2017c). Therefore, only the rotating speed is used here to speed up the stroke speed with a constant feed ratio.

3.6.4 Mass scaling

Mass scaling is another way to speed up the simulation time with an assumption of a quasi-static state. As the density of material increases, the dilatational wave speed in material decreases, hence the stable time step size increases. The mass is added to quantify the number of elements whose characteristic length is small so that the time step size satisfies all the elements of the plate. In this way, greater mass is added to the inner surface of the plate where the characteristic lengths of these elements are the smallest.

3.7 Experiment and simulation configuration

The proposed numerical model was validated with experiments and its robustness verified using common models. An experiment of the conventional spinning of a hemi-spherical part described in (Kong, Yu, Zhao, Wang, and Lin, 2017c) was used, as well as the results of their simulation.

The aluminum alloy 2024-O circular plate with the properties listed in Table 3.6 has a 200mm diameter and 1.8 mm thickness. The mandrel speed is 200 rpm, and the feed ratio is 1 mm/rev. The process parameters and the toolpath are shown in Figure 3.14; a workpiece with thickness 1.8 mm and a roller radius of 10 mm follows the shape of the mandrel with radius of 69.61 mm until reaching the angle 55°.

The thickness distribution is measured when the stroke angle, which is the angle between the roller and the center axis shown in Figure 3.15, is 55°.

The elements shown along the line indicated in Figure 3.16 are selected to measure their thickness. The thickness of the final product was measured by the laser scanning system.

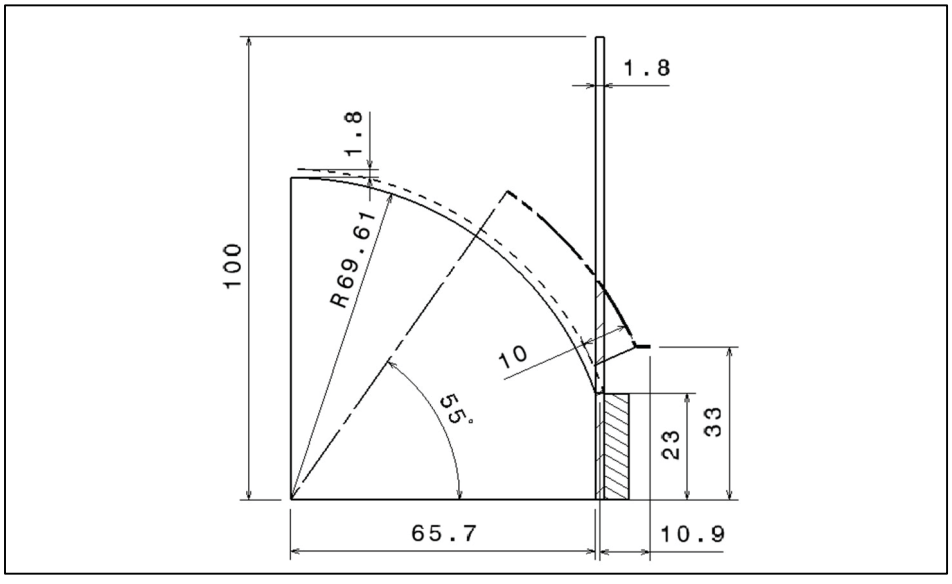

Figure 3.14 Process geometry and toolpath dimension

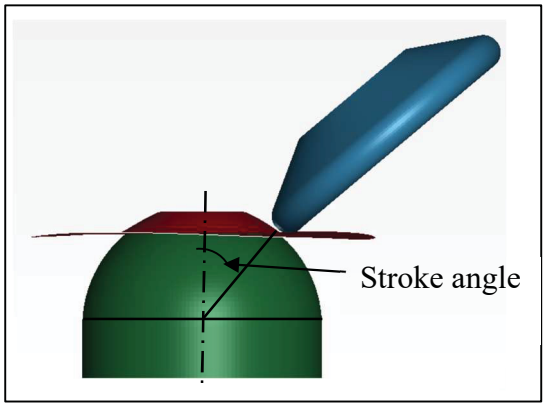

Figure 3.15 Roller stroke angle

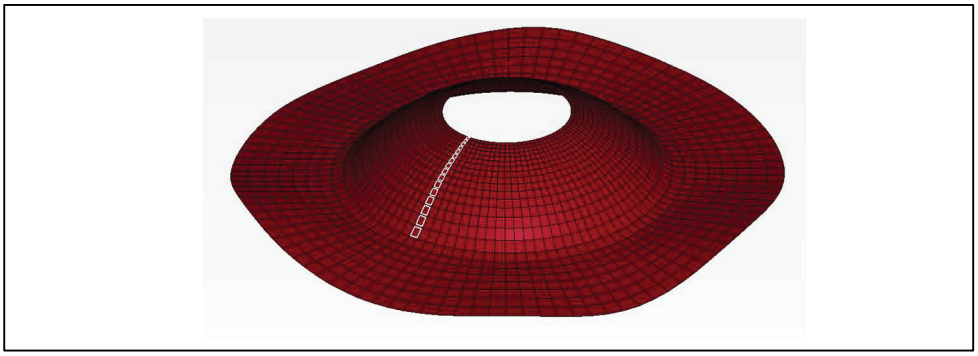

Figure 3.16 Thickness measurement line when stroke angle is 55°

3.8 Results and discussion

3.8.1 Mesh convergence study

A reliable result is a value that is not affected by changing the size of the mesh. The response of thickness distribution will converge to a repeatable solution with decreasing element size. Therefore, one strategy is to run multiple simulations from coarse mesh to fine mesh until a converged result is obtained.

The disc can be meshed using two parameters: the number of elements in the radial direction n_r and the number of elements in the circumferential direction n_c as shown in Figure 3.17. The running strategy is simple when there is only one variable to vary instead of two, n_r and n_c. In this chapter, the rule applied to construct a relation between r and c is that the aspect ratio of the mesh is always minimized. By focussing on this minimization of the mesh ratio, the solution is convergent to the final value which matches well to the experiment.

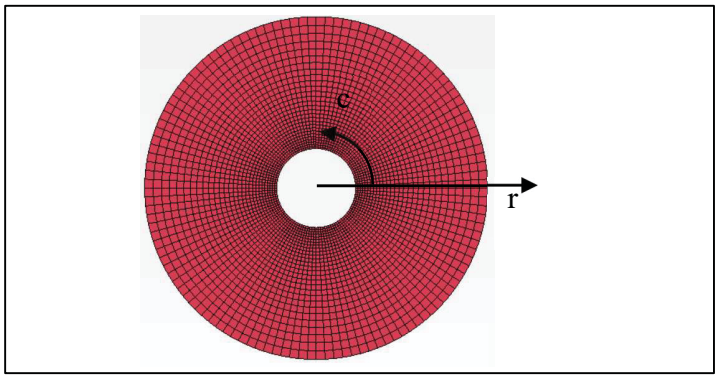

Figure 3.17 Meshing parameters of the disc: n_r, n_c

The aspect ratio is the ratio of the longest and shortest lengths of an element's edges. Let us start with the element shown in Figure 3.18. It is formed by three parameters s_n, ΔR_n and s_{n+1}. The first length of the element is

$$s_n = 2R_n \, tan\left(\frac{\pi}{c}\right) \tag{3.33}$$

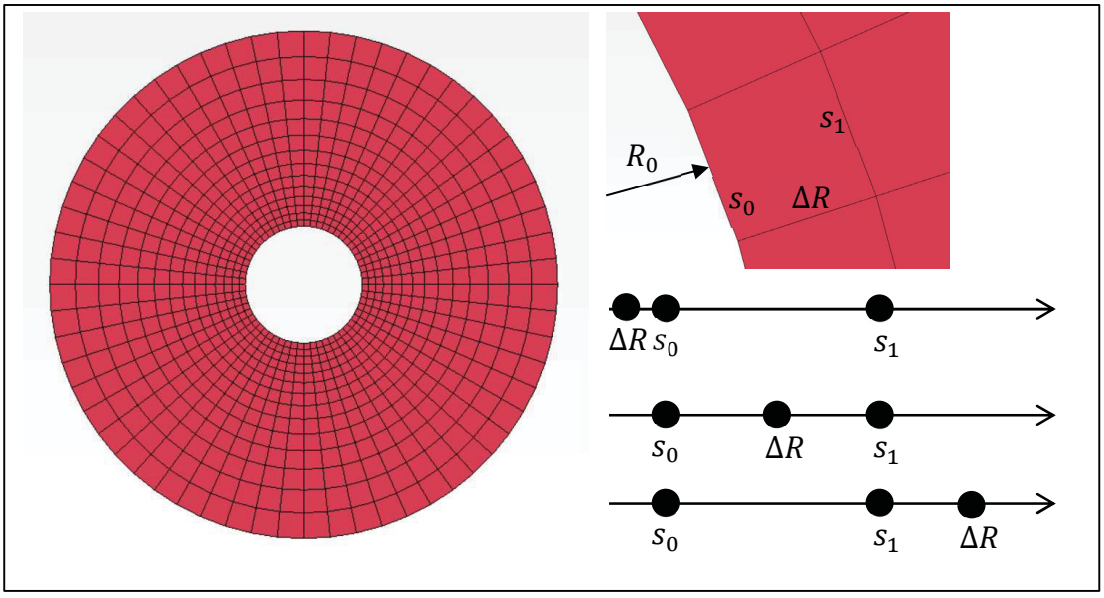

Figure 3.18 Three individual element parameters: s_0, s_1 and ΔR

The parameter s_{n+1} can be calculated in the same manner with a larger radius $R_{n+1} = R_0 + \Delta R$.

$$s_{n+1} = 2R_{n+1}\, tan\left(\frac{\pi}{c}\right) = 2(R_n + \Delta R_n)\, tan\left(\frac{\pi}{c}\right) \tag{3.34}$$

The parameter s_{n+1} is always larger than s_n. Therefore, the parameter ΔR can fall into three possible cases: $\Delta R_n \leq s_n < s_{n+1}$, $s_n < \Delta R_n < s_{n+1}$ and $s_n < s_{n+1} \leq \Delta R_n$. This image is shown in Figure 3.18.

In the first case with $\Delta R_n \leq s_n < s_{n+1}$, the aspect ratio $AS_1 = \frac{s_{n+1}}{\Delta R_n}$, so that $\min\limits_{\Delta R_n} AS_1 = \frac{s_{n+1}}{s_n} = 1 + 2\tan\left(\frac{\pi}{c}\right)$ when $\Delta R = s_n$.

In the second case with $s_n < \Delta R_n < s_{n+1}$, the aspect ratio $AS_2 = \frac{s_{n+1}}{s_n}$, so that $\min_{\Delta R_n} AS_2 = \frac{s_{n+1}}{s_n} = 1 + 2\tan\left(\frac{\pi}{c}\right)$.

In the third case with $s_n < s_{n+1} \leq \Delta R_n$, the aspect ratio $AS_3 = \frac{\Delta R_n}{s_n}$, so that $\min_{\Delta R_n} AS_3 = \frac{s_{n+1}}{s_n} = \frac{1}{1-2\,\mathrm{ta}\,\left(\frac{\pi}{c}\right)}$ when $\Delta R = s_{n+1}$.

The values of AS of the first two cases are the same but they are smaller than in the third case and are calculated as shown below in equation (3.35).

$$s_{n+1} = 2R_{n+1}\,tan\left(\frac{\pi}{c}\right) = 2(R_n + \Delta R_n)\,tan\left(\frac{\pi}{c}\right) \tag{3.35}$$

In conclusion, the minimum aspect ratio is $1 + 2\tan\frac{\pi}{c}$ when the $\Delta R_n = s_n$.

There is a way to adjust mesh parameters so that the aspect ratio is satisfied. First, the dividend in the circumferential direction is chosen to be constant. The aspect ratio is then adjusted by the parameter n_r and the bias factor bf, which is used to control the length of the elements in the radial direction.

For a given number of elements in the circumferential direction, the bias factor bf relates to the growth rate r and the number of elements in the radial direction n_r.

$$bf = r^{n_r - 1} \tag{3.36}$$

The growth rate r is the ratio between the length of two contiguous elements in the radial direction.

$$r = \frac{\Delta R_{n+1}}{\Delta R_n} = \frac{s_{n+1}}{s_n} = 1 + \frac{\Delta R_n}{R_n} = 1 + \frac{s_n}{R_n} = 1 + 2\,tan\frac{\pi}{c} \tag{3.37}$$

The number of elements is related to the growth rate as shown in the equation below.

$$L = \sum_{i=0}^{n_c-1} l_1 r^i = \frac{l_1\left(1 - r^{i+1}\right)}{1 - r} \tag{3.38}$$

The number of elements in the radial direction n_r is calculated with equation (3.38). The bias factor is calculated with equation (3.36).

Finally, Table 3.7 presents solutions from four meshes using Ansys Workbench software with parameters $n_c\_n_r$ equal to 60_40, 80_18, 100_24, and 120_28.

Table 3.7 Bias factor and average aspect ratio for four different meshes

Mesh	n_e	Bias factor	Aspect ratio average
60_14	840	4.032	1.0078
80_18	1440	3.89988	1.0385
100_24	2400	4.3166	1.0267

The simulation is speeded up by loading rate scaling of values 10000 rpm and 20000 rpm. The feed ratio is constant. However, in the experiment, the forces acting on the plate are calculated at a value of 200 rpm.

The thickness distribution of the loading rate scaling at 20k rpm is shown in Figure 3.19. The first two meshes exhibit a large difference at about the first 10%. While the last two meshes

seem to match very well together, the convergent mesh for this rate scaling was finally obtained at mesh 100_24 and 120_28.

The solution of convergent meshes run with three different artificial rotating speeds 10k rpm, 20k rpm, and 30k rpm are shown in Figure 3.20. The two curves with the speeds of 10k and 20k are very close to each other. The curve with the speed 30k fits with the others until around one third of the range, and then it diverges. Therefore, the convergent rate scaling is set at 10k rpm.

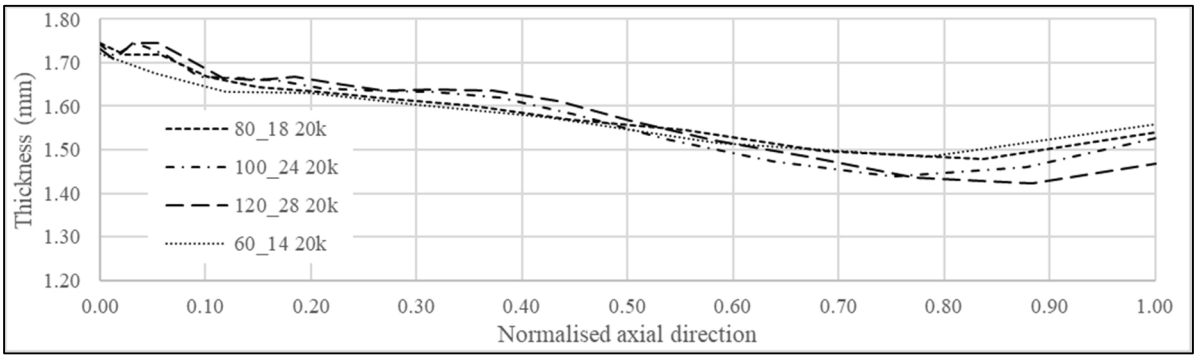

Figure 3.19 Thickness distribution of four meshes at the artificial rotating speed of 20k rpm

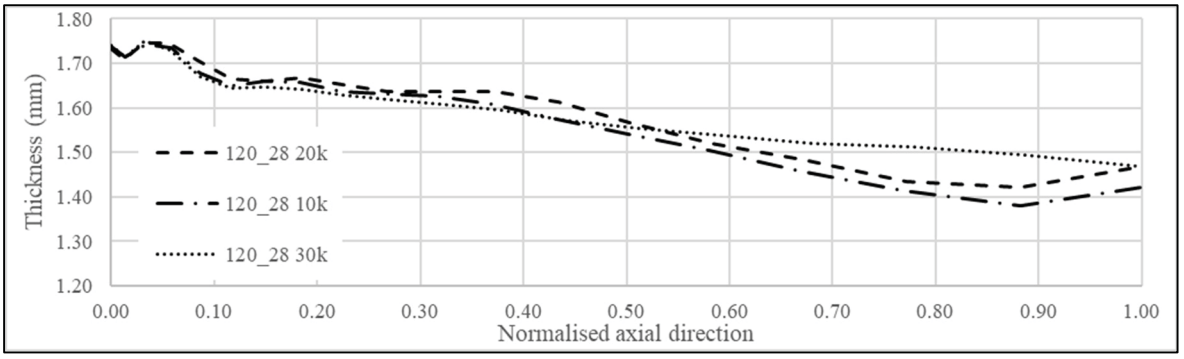

Figure 3.20 Thickness distribution of convergent meshes at three artificial rotating speeds

3.8.2 Comparison of the experimental model with a conventional model

The thickness distribution of convergent meshes is compared to the experimental and the conventional model with the highest element number from (Kong, Yu, Zhao, Wang, and Lin, 2017c), as shown in Figure 3.21. The maximum error between the new model and the experimental model is 7.38% at value 0.78.

The trend of the thickness distribution agrees well with the experiment values in the case of the new model, with four peaks: 2 top peaks at 0.03 and 0.16 and 2 bottom peaks at 0.11 and 0.878. This not the case for the conventional model shown in Figure 3.21.
The maximum difference between experiment and simulation is 0.06 mm at a normalized axial of 0.88 where the stroke angle is 55°. This value is still below the tolerance of sheet metal thickness variation ±0.1 mm ("Thickness Tolerances of Aluminium from Ullrich Aluminium," n.d.).

The number of elements of the densest mesh of the conventional model is 9000, while only 3360 elements are needed for the convergent solution in the new model.

The number of elements of the densest mesh of the conventional model is 9000, while only 3360 elements are needed for the convergent solution in the new model. Furthermore, the conventional model is performed with a mass scaling of 25. This means the time step is boosted by $\sqrt{25}=5$ times. The new model can get a convergent solution at an artificial rotating speed of 10k rpm i.e., 50 times faster. This reveals that the computational cost of the new model is more economical than that of the conventional one in both the number of elements and scaling aspects, appropriate 12.67 times that are 10 times in term of scaling and 2.67 times in term of element number.

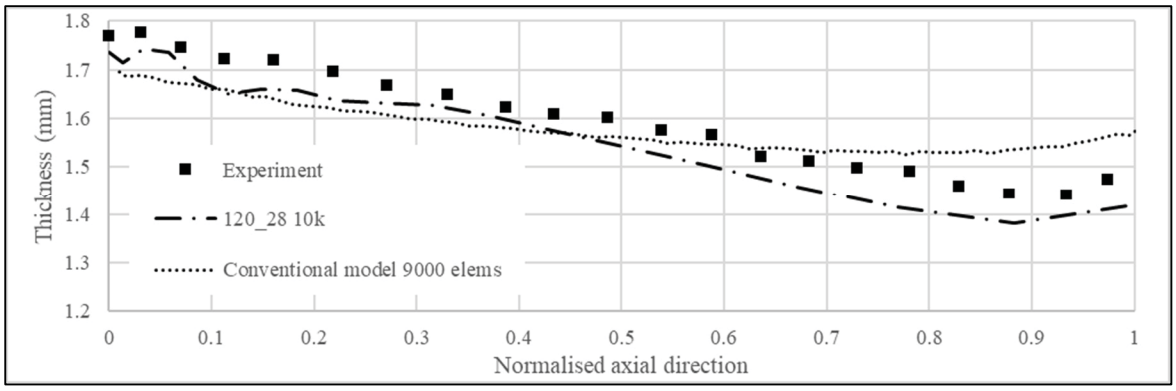

Figure 3.21 Thickness distribution of experiment versus new model and conventional model

3.8.3 Loading rate scaling versus mass scaling

The thickness distribution of the numerical models with mass scaling and loading rate scaling are shown in Figure 3.22. The two curves representing the numerical results match together over almost all of the range except at the beginning and near the end. A first observation is that the loading rate scaling gives a better result than mass scaling because mass scaling adds most of the mass to the inner area of the plate due to the small characteristic length of those elements. This mass produces an error of artificial added mass in this area.

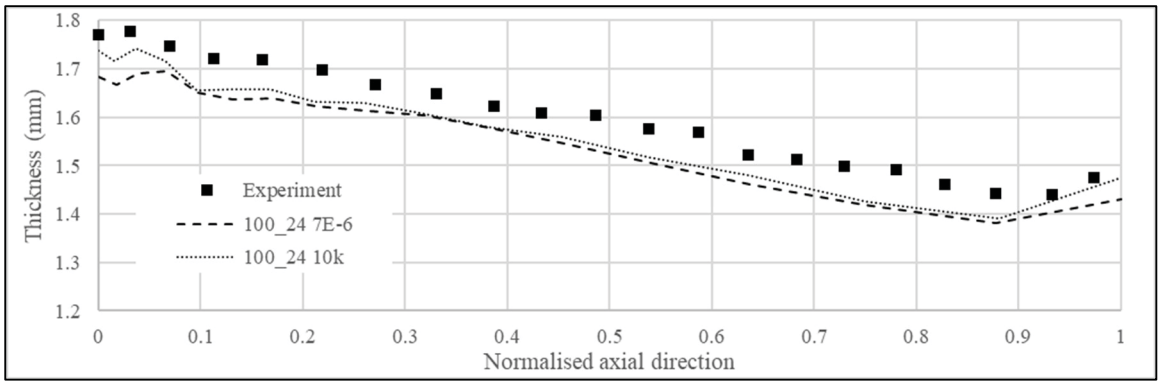

Figure 3.22 Thickness distribution of mass scaling versus loading rate scaling versus experiment results

Secondly, loading rate scaling has the flexibility to be applied at different stages of the process, which makes it possible to control the accuracy at any desired area.

Thirdly, mass scaling gives a convergent solution with a time step size of 7E-6 for the process time of 16.654, hence the time step number is 2.379.142, while loading rate scaling case has a convergent time step size of 1.96E-7 for the process time 0.333s and so its time step number is 1.698.979. Obviously, the computational time of loading rate scaling is less than the mass scaling case by a ratio of 1.4.

However, loading rate scaling has a disadvantage: it cannot be applied to rate-dependent material (ABAQUS, 2019) because it changes the rate of deformation which will affect the response stress-strain curve of rate-dependent material.

3.8.4 Influence of the rotating speed

By analyzing the spinning process in a rotating reference frame, it can be determined that the rotating speed of the mandrel creates the centrifugal force and the Coriolis force. According to (Nguyen, Champliaud, and Lê, 2018), the maximum stresses are where centrifugal force is created on the plate, as summarized in Table 3.8. While the yield stress of the material is 70.06 MPa, the maximum stress in the plate is 1.78 MPa at 3200 rpm, 2.54% of the yield stress. This really has a very small effect on the deformation of the plate.

Table 3.8 Stresses in the plate with various rotating speeds

Rotating speed (rpm)	**Radial stress**	**Circumferential stress**
200	6.94E-3	3.6E-3
1000	1.73E-1	9.01E-2
3200	1.78	0.922

The rotating speed also affects the stroke speed of the roller to the plate by the feed rate. This increased speed is still in the quasi-static zone, as it is less than 1% of the wave speed of the material. The simulation with a very high stroke speed at 10000 rpm showed very small changes in the results. Hence, the variations observed in the results when increasing the rotating speed to 3200 are very small and can be neglected.

3.9 Summary

A novel modeling technique was introduced, accompanied by its underlying theoretical framework and a comprehensive implementation within the LS-DYNA software. This technique underwent comparative assessment against both experimental data and a conventional model. Remarkably, the results derived from the new model exhibited a high degree of agreement with the experimental data, indicating significant advancements in predicting thickness variation. Notably, the new model demonstrated superior accuracy in terms of value error and trend.

In terms of computational efficiency, employing loading rate scaling for the mandrel rotating speed resulted in a remarkable 50-fold reduction in computational time for the analysis. Furthermore, the integration of the proposed mesh pattern significantly enhanced the accuracy and efficiency of the new model, further underscoring its potential for practical application in industrial settings.

CHAPTER 4

CIRCUMFERENTIAL CRACKING IN CONVENTIONAL METAL SPINNING PROCESS

Article published in "17th International Multidisciplinary Modeling & Simulation Multiconference", January, 2020

Circumferential cracking of conventional metal spinning process is investigated by means of finite element simulation using the Generalized Incremental Stress State dependent damage model (GISSMO). This model provides a damage scalar as an indicator to remove elements where a crack appears. Result show that simulation predictions are in very good agreement with experiment cracking locations. A region around the cracking area deforms in the opposite direction of a roller's stroke during cracking. This phenomenon is considered as a reason for circumferential cracking at the interaction between a plate and a tailstock. This chapter shows a successful damage model to predict circumferential crack and new insights into this defect. In the next sections, the GISSMO's formula is presented shortly. This formula illustrates the meaning and the number of parameters needing to be known. A simple strategy, applied only for the spinning process, is proposed to obtain these parameters. Finally, the simulation of spinning process using the GISSMO is conducted and analyzed.

4.1 GISSMO for predicting failure in spinning process.

The evolution of material under deformation contains three states in the orders of elastic, plasticity, and fracture. Each state requires some properties for complete definition. Shell element is used to model the thin sheet metal with plane stress condition. Therefore, the material model now only focuses on 2D stress and 2D strain.

4.1.1 Constitutive relationship in elastic region

In the elastic region, the material's properties are assumed to be isotropic. The relationship of stress and strain is linear and presented as below.

$$\begin{bmatrix}\sigma_{11}\\ \sigma_{22}\\ \sigma_{12}\end{bmatrix} = \frac{E}{1-\nu^2}\begin{bmatrix}1 & \nu & 0\\ \nu & 1 & 0\\ 0 & 0 & \frac{1-\nu}{2}\end{bmatrix}\begin{bmatrix}\epsilon_{11}\\ \epsilon_{22}\\ 2\epsilon_{12}\end{bmatrix} \tag{4.1}$$

Two properties need to be determined are the Young's modulus E and the Poisson's ratio ν.

4.1.2 Constitutive relationship in plastic region

A switch of elastic to plastic state is determined by the yield condition as be written as

$$f(\sigma, \epsilon_p) = \sigma_{eff}(\sigma_{11}, \sigma_{22}, \sigma_{12}) - \sigma_Y(\epsilon_p) \leq 0 \tag{4.2}$$

With σ_{eff}: effective stress; σ_Y: yield stress; ϵ_p: effective plastic strain

If the yield condition is negative, the state of material is on the elastic and vice versa. The yield stress $\sigma_Y(\epsilon_p = 0)$ and the hardening stress curve $\sigma_Y(\epsilon_p)$ are determined experimentally by the tensile test because this test presents the uniform deformation in the gauge region and constant volume change (the Poisson's ratio is 0.5) in plastic state hence the conversion from the measurement (force vs displacement) to the hardening stress curve $\sigma_Y(\epsilon_p)$ is straight forward as be illustrated in appendix A.

The effective stress σ_{eff} is Von Mises stress for assumption that the material is isotropic.

4.1.3 Constitutive relationship in fracture region

The Generalized Incremental Stress State dependent damage Model (GISSMO) is used for adding damage to the existing material model (elastic and plasticity). A damage (scalar) $0 \leq D \leq 1$ is added to the stress tensor

$$\boldsymbol{\sigma}^* = \boldsymbol{\sigma}(1 - D) \tag{4.3}$$

An assumption is that the material has already very small defect prescribed by $D = 1e^{-20}$ so $\boldsymbol{\sigma}^* \cong \boldsymbol{\sigma}$. During the deformation, the defect expands itself inside the material until $D = 1$ so $\boldsymbol{\sigma}^* = 0$ at which the material is totally fracture.

According to a work (Mackenzie, Hancock, and Brown, 1977), the failure strain depends on a triaxiality which means that there are many failure strains respecting to various triaxiality. Triaxiality is defined as a ratio of pressure stress to the effective stress.

$$\eta = \frac{\sigma_{xx} + \sigma_{yy} + \sigma_{zz}}{3\sigma_{eff}} \tag{4.4}$$

The evolution of damage scalar is

$$\Delta D = \frac{n}{\epsilon_{failure}(\eta)} D^{1-\frac{1}{n}} \Delta\epsilon_p \tag{4.5}$$

With ΔD:	the incremental damage scalar
D:	the current damage
n:	the damage exponent

ϵ_p: the effective plastic strain

$\epsilon_{failure}$: the failure strain

η: the triaxiality

In equation (4.5), two parameters damage exponent n and failure strain $\epsilon_{failure}$ are unknown. The damage exponent n is chosen so that the damage scalar only grows significantly at the final region of plastic strain instead of elastic and plastic region. Usually, $n = 3$ is chosen. The effective plastic strain at which fracture is the failure strain.

In conclusion, the fracture model needs the failure strain as a function of triaxiality.

4.1.4 Strategies to determine model parameters

Properties which are needed to obtain, are:

For elastic

E: The Young modulus

ν: The Poisson's ratio

For plasticity

$\sigma_Y(\epsilon_p)$: The hardening curve

For fracture

$\epsilon_{failure}(\eta)$: The failure strain

The properties E, ν, $\sigma_Y(\epsilon_p)$ are obtained by tensile test. The hardening curve $\sigma_Y(\epsilon_p)$ is a function of effective plastic strain versus yield stress. In tensile test, the effective plastic strain is the true plastic strain, and the yield stress is the true stress. They are calculated using equations in Appendix A.

The final parameter, needed to determine, is the failure strain curve $\epsilon_{failure}(\eta)$ which is a collection of failure strain respected to various triaxialities. This parameter requires a numerous

of experimental tests, including shear 0^0, shear 45^0, small tensile test, notched tensile test and biaxial test (Andrade, Feucht, and Haufe, 2014) to fully define which are expensive to do. However, the simulation of spinning process showed that the critical region has the triaxiality of 0.5. Fortunately, the fracture region in the tensile test also has the triaxiality of 0.5 showed in Figure 4.1 which is the same as spinning process circumferential crack area. This means that the state of stress on the failure period is the same of both tensile test and spinning process. Therefore, the only failure strain of tensile test is enough to predict circumferential crack for spinning process.

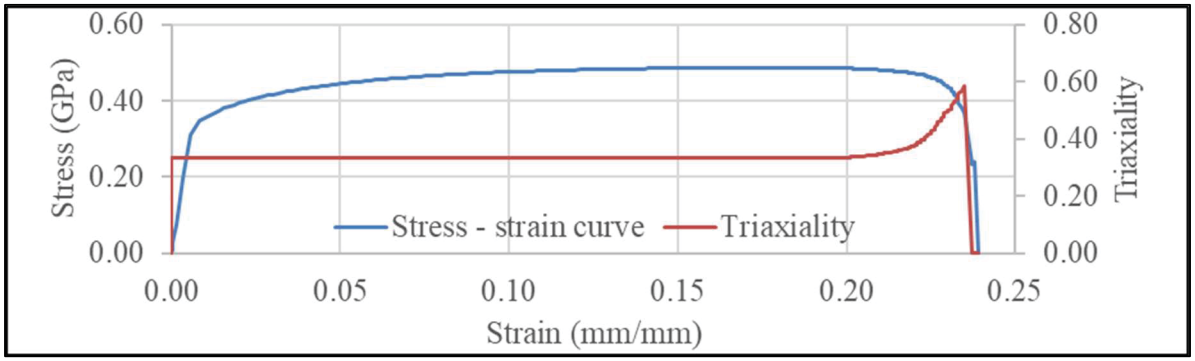

Figure 4.1 Stress - strain curve and triaxiality

The failure strain is obtained by reverse – engineering approach because the effective plastic strain in damage area cannot be calculated by the data from the tensile test. These formulas in the Appendix are only applicable in the plasticity region. The steps are:

- Calculate the young modulus, effective plastic strain versus yield stress.
- Conduct tensile test simulation. This should give the same stress – strain curve as tensile test experiment.
- In the tensile test simulation, note the maximum effective plastic strain according to the elongation of failure in the experiment tensile test.

- This value is chosen as an initial failure strain. The tensile test simulation is conducted. The expected result will be only different beyond necking point.
- Try to adjust the failure strain to match results between tensile test simulation and tensile test experiment.

4.1.5 Analysis of simulation

The circular disc is made from the aluminum 2024 with properties are presented in Table 4.1.

Table 4.1 Aluminum 6061-T6 properties

Young modulus	E = 56.388 GPa
Yield offset	0.002
Yield strength at offset	$\sigma_y = 347.9$ MPa
Engineering ultimate tensile strength	EUTS = 487.4 MPa
Mass density	2.7E-6 kg/mm^3

The material model is isotropic elastoplastic using a power law hardening rule.

$$\sigma_t = K\epsilon_t^n \tag{4.6}$$

With

σ_t: True stress

ϵ_t: True strain

K: Strength coefficient

n: Strain hardening coefficient

The values of K and n are 0.1642 and 0.7723 respectively. The failure strain is 0.75. The output of a material model with GISSMO is showed in Figure 4.2.

The kinematic setup uses a special approach developed by (Nguyen, Champliaud, and Lê, 2018). This setup requires the stationary mandrel and so the rotating tool. The implicit time integration scheme is used to eliminate the trial – error of mass scaling guesswork and provides unconditional stability.

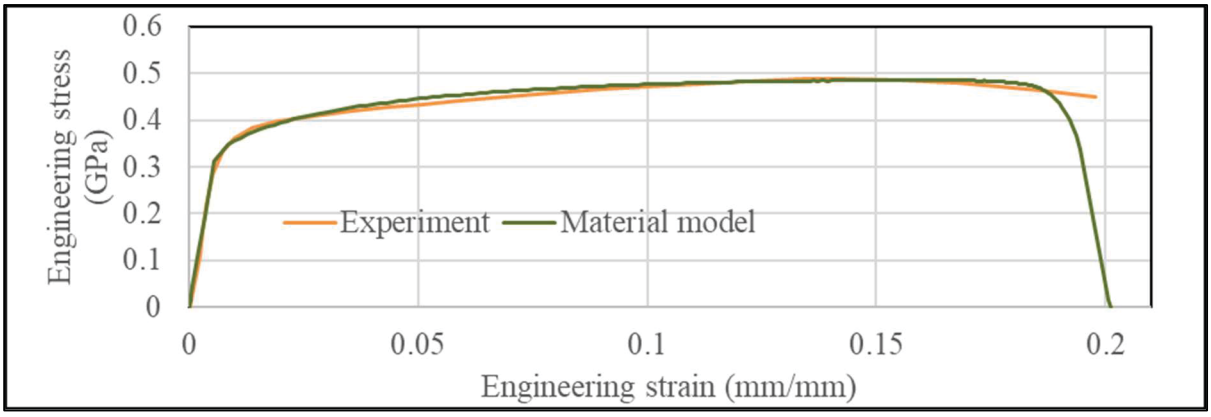

Figure 4.2 Engineering stress - strain curve of experiment and material model

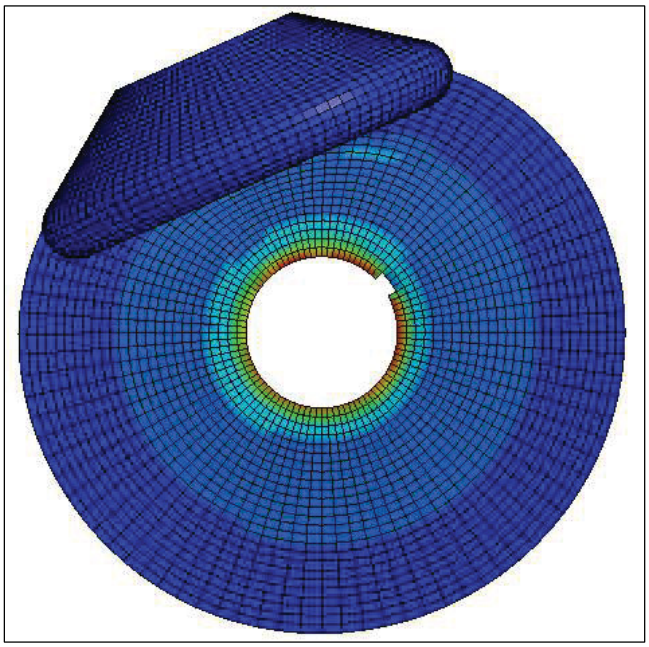

Figure 4.3 Circumferential crack at beginning

The Figure 4.3 showed the first place where crack is initial. The Figure 4.4 showed the crack grown in the circumferential direction and expected to complete a circle at the intersection of the plate and the mandrel. This position matched exactly with the experiment showed in Figure 1.2.

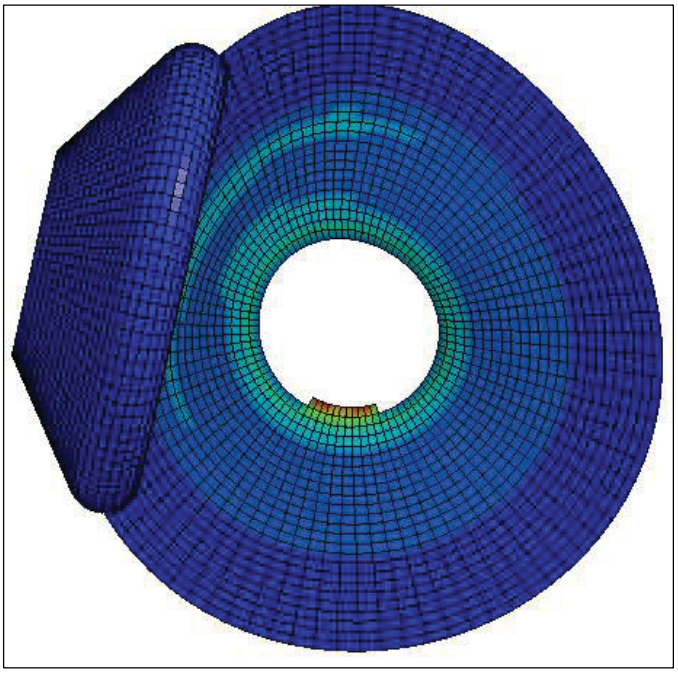

Figure 4.4 Circumferential crack at ending

The displacement around cracking is in the opposite direction with the stroke direction of the roller where is showed in Figure 4.5. Therefore, this area doesn't get support from the mandrel behind it. The stress state in this area, showed in Figure 4.6, is the same as the middle of tensile test beyond the necking moment. The magnitude of this displacement increases gradually following the roller's stroke increment until damage reaches unity then those elements were deleted as cracking happened.

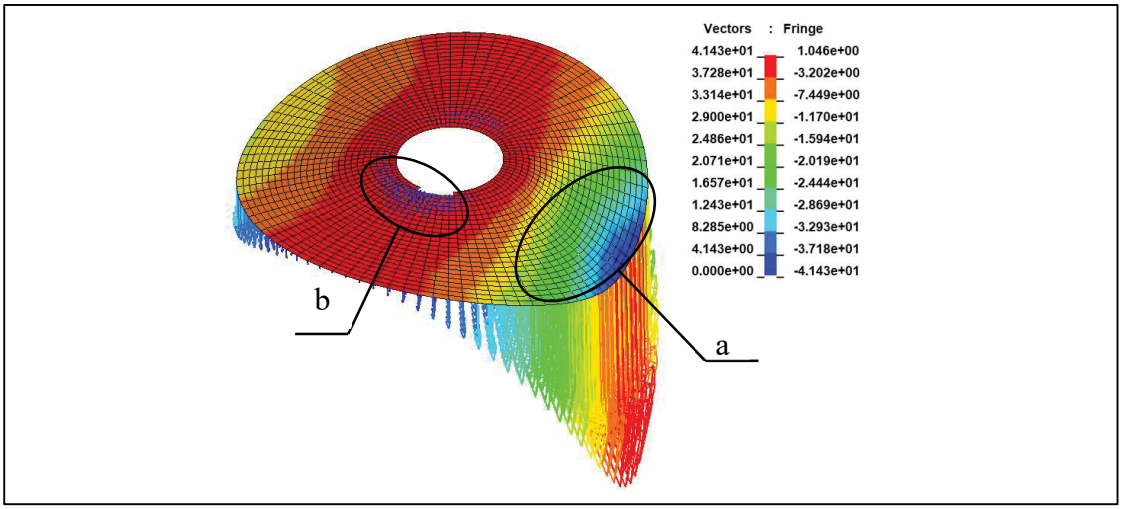

Figure 4.5 Displacement contribution when cracking; a. Roller contact area; b. Displacement around circumferential cracking

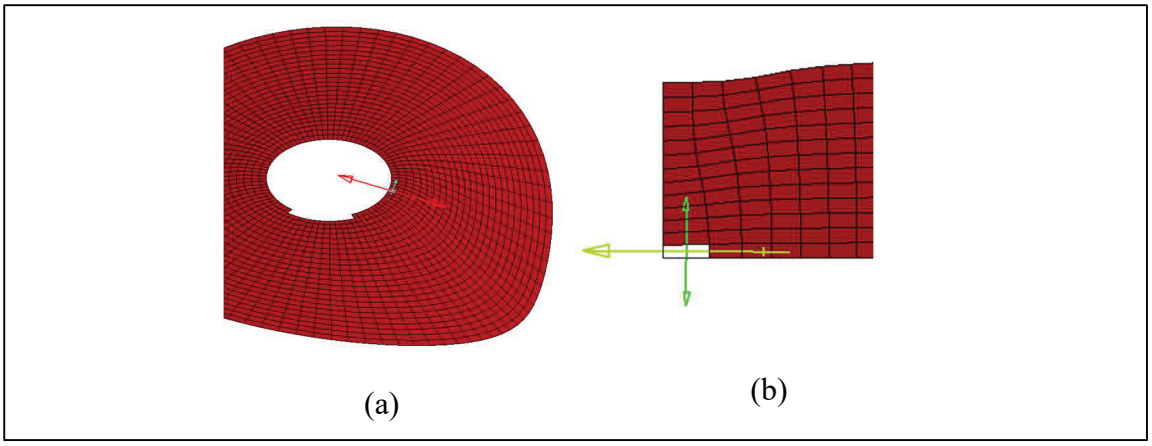

Figure 4.6 Stress state at cracking area; (a) metal spinning process; (b) tensile test

4.2 Summary

The GISSMO utilized in the spinning process has reached a mature stage of development. The failure strain is determined through a reverse engineering approach derived from simulations

of tensile tests. The stress-strain curve generated by the model closely aligns with experimental observations.

The simulation of the spinning process yielded results consistent with experimental outcomes, validating its efficacy.

A comprehensive explanation of the circumferential cracking mechanism was provided, offering valuable insights. These understandings hold promise for devising a theoretical framework to compute critical process parameters, including rotating speed, feed ratio and paths, roller diameter, and radius, among others.

CHAPTER 5

ANALYSIS OF MECHANISM INVOLVED IN THE METAL SPINNING PROCESS IN ONE FULL ROTATION OF MANDREL

Part of chapter published to "Journal of Manufacturing and Materials Processing", in January, 2024.

In this chapter, an analysis, based on deformed location and volume consistency during plasticity deformation is performed in one full rotation of the mandrel. The result, including the displacement distribution of the workpiece, the stain distribution on the workpiece, the thickness distribution of the workpiece, is investigated.

Consequently, the general expansion of the whole process is analyzed. The effect of the toolpath on the displacement of workpiece, the flange's circumference is presented.

Finally, the application of these analysis is presented, including proposed wrinkle-free toolpaths, a correlation to conventional paths, and an optimized thickness by intermediate paths.

5.1 Metal spinning formula and solution

The workpiece is deformed by a combination of rotating mandrel and movement of the roller. The roller movement usually contains multiple paths. Each path has a unique geometry represented commonly by a concave involute curve. This curve can be viewed as constructed by multiple straight segments. The length of each segment is equal to the feed rate $f\,(\mathrm{mm/rev})$ which is the distance of the roller movement over one rotation of the mandrel. Figure 5.1 illustrates the formation of the spinning process for one rotation of the mandrel and one roller path segment.

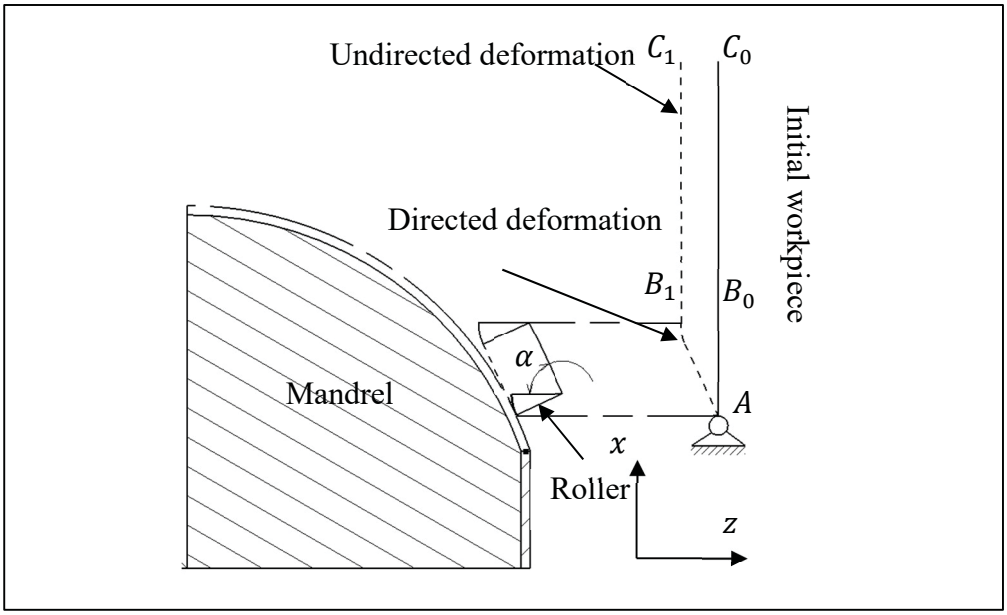

Figure 5.1 Problem formulation in one cycles of mandrel's rotation

The initial workpiece is viewed in 2D dimension by a straight line AC_0. The roller starts to deform the workpiece at the location A. The roller path is a straight line constructed by a stroke angle α and a length f. The deformed workpiece is presented by two parts: directed deformed segment AB_1 and undirected deformed segment B_1C_1.

The solution to this problem is obtained by the FEM simulation.

5.2 Displacement distribution on the workpiece

The initial workpiece, presented by a segment AC_0, is deformed to the segment AC_1. The deformed segment AC_1 contains two segments AB_1 and B_1C_1. The geometry of the segment AB_1 follows the shape of the path defined by a straight line with its length equal to feed rate and stroke angle α. The segment B_1C_1 is approximately an offset segment of the initial one B_0C_0.

The workpiece displacement can be considered mainly in plane $X - Z$ as shown in Figure 5.1 hence the displacement in two directions x and z are concerned. The displacement of the point A can be considered as fixed in both directions x and z.

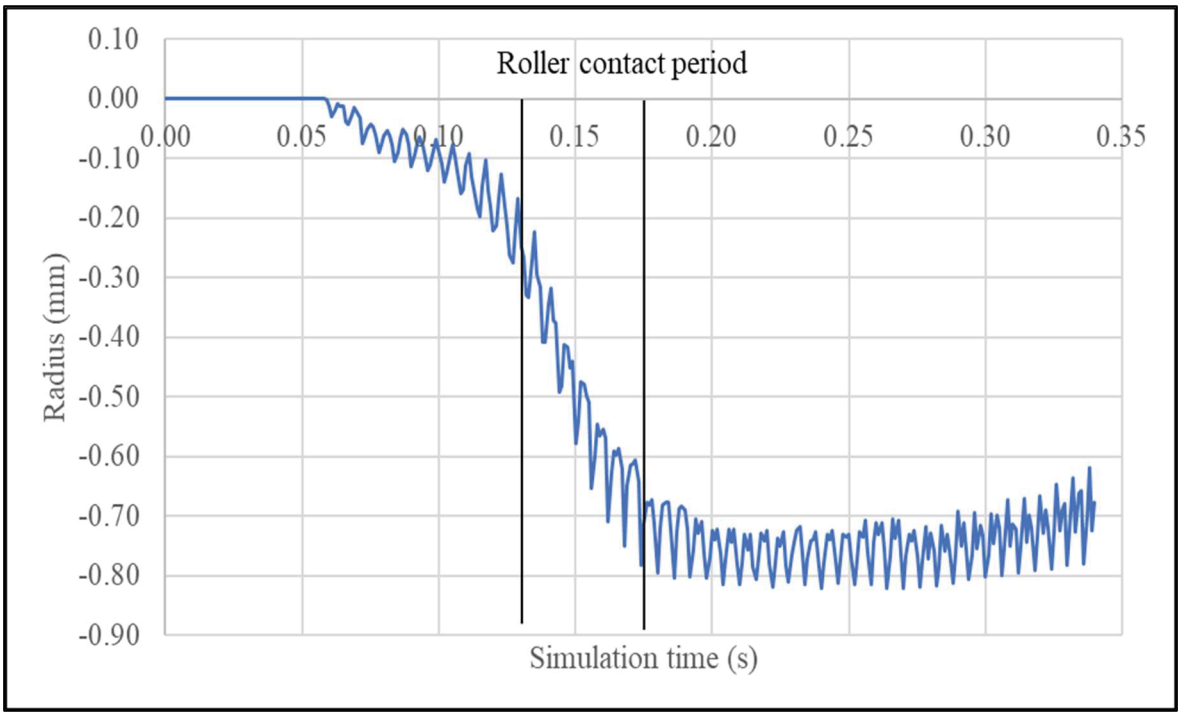

Figure 5.2 Typical radial displacement of points in segment AB_0

The radial displacement (direction x) of points in the segment AB_0, shown in Figure 5.2, reduces prior and during the period of contact with the roller, then it remains flat after contacting.

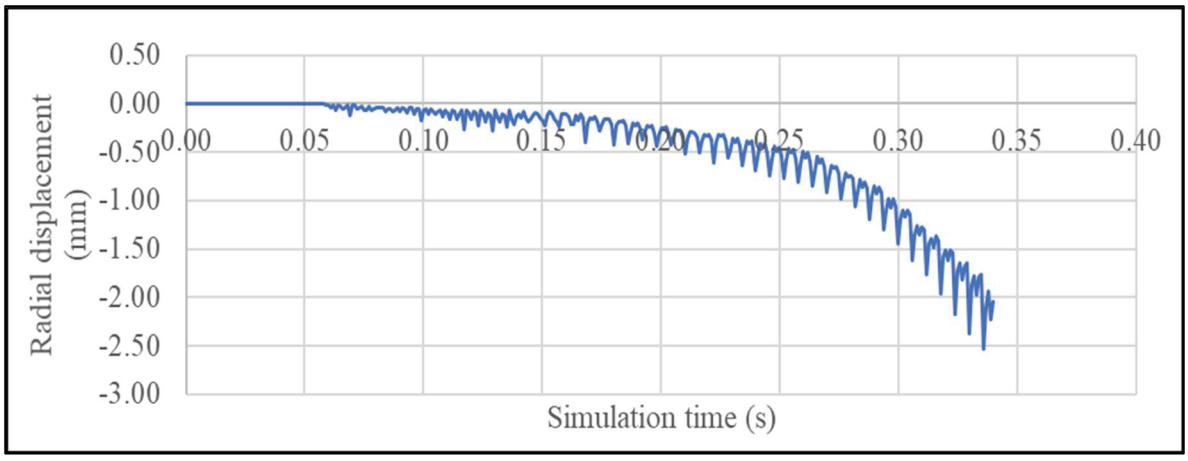

Figure 5.3 Flange radial displacement reduction versus time during the process

The segment B_0C_0 has not contacted yet with the roller but its radial displacement, shown in Figure 5.3, also illustrates the decrease continuously during the process.

5.3 Strain distribution on the workpiece

The workpiece is observed to be deformed plasticity in the whole area as shown in Figure 5.4. The minimum effective plastic strain on the workpiece, appeared very soon just after the roller contact, is $5.589e^{-6}$ MPa at element 1007 near the flange. During the process, the maximum plastic area is observed just behind the roller contact area. Due to plastic deformation, the workpiece can be considered as volume consistency during the metal spinning process. Therefore, any defect such as wrinkles and cracks occur in the plastic state.

The principal in-plane strain vectors in the workpiece are shown in Figure 5.5. The principal in-plane strain in radial direction is the tensile strain which is maximum value at the deformed area just adjacent to the roller. This tensile strain in radial direction reduces gradually toward the flange. The principal in-plane strain in the circumferential direction is compressive which has the same behavior as tensile strain in the radial direction, maximum value at the deformed area just adjacent to the roller and reduces gradually toward the flange.

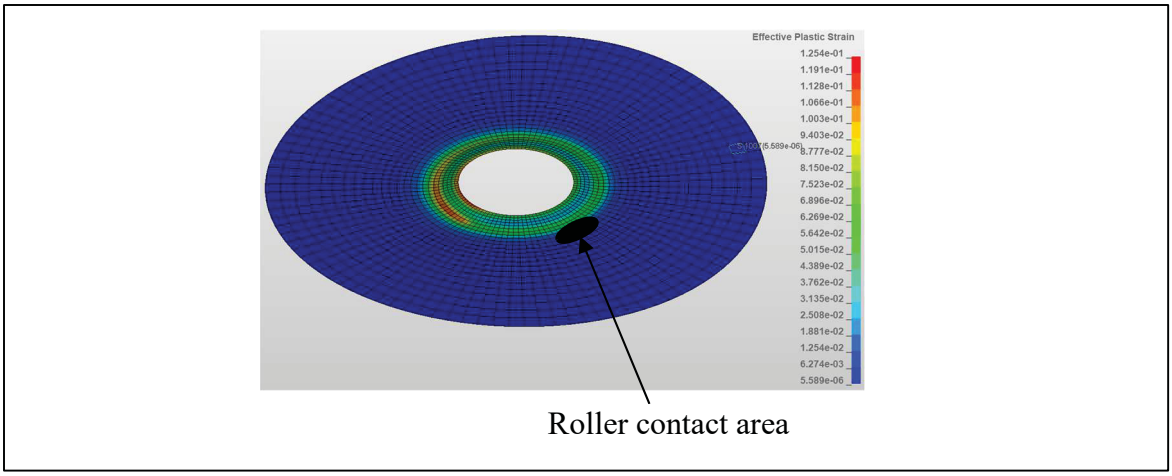

Figure 5.4 Location of minimum effective plastic strain

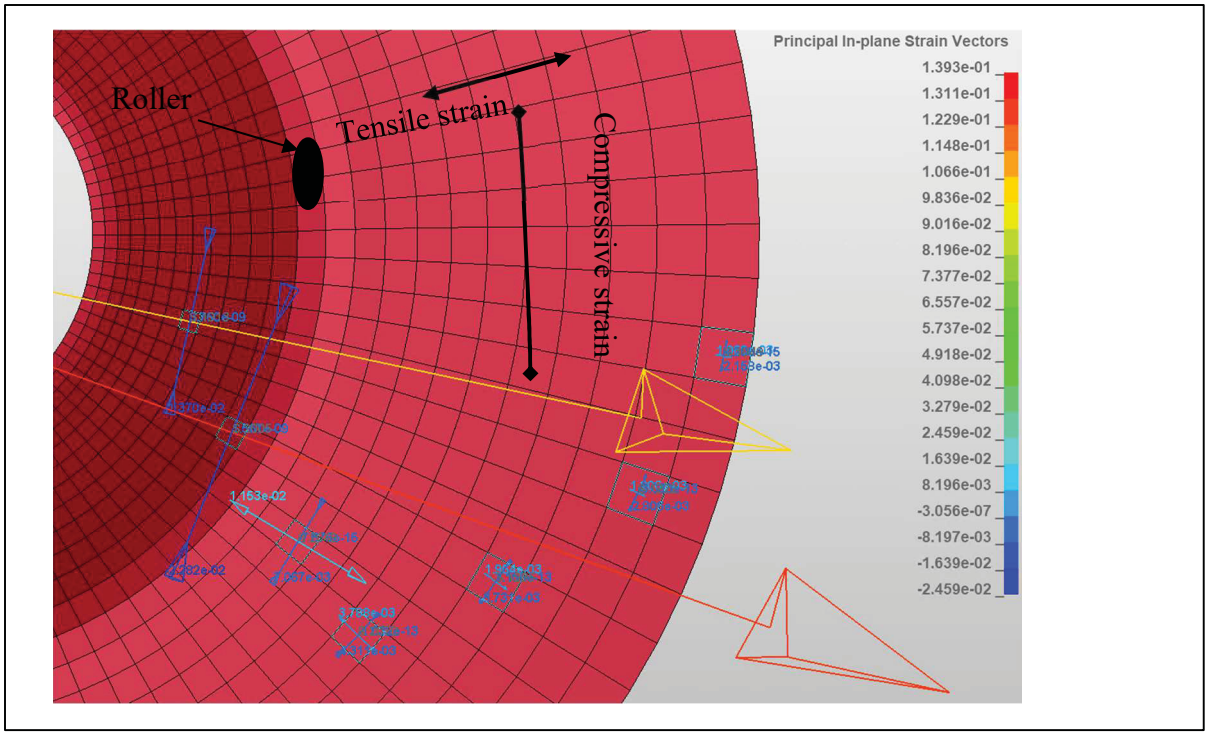

Figure 5.5 Principal in-plane strain distributed in the workpiece: tensile strain in radial direction; compressive strain in the circumferential direction

5.4 Thickness distribution of the workpiece

The thickness changes the workpiece is shown in Figure 5.6 and Figure 5.7 for directed contact segment and undirected contact segment respectively.

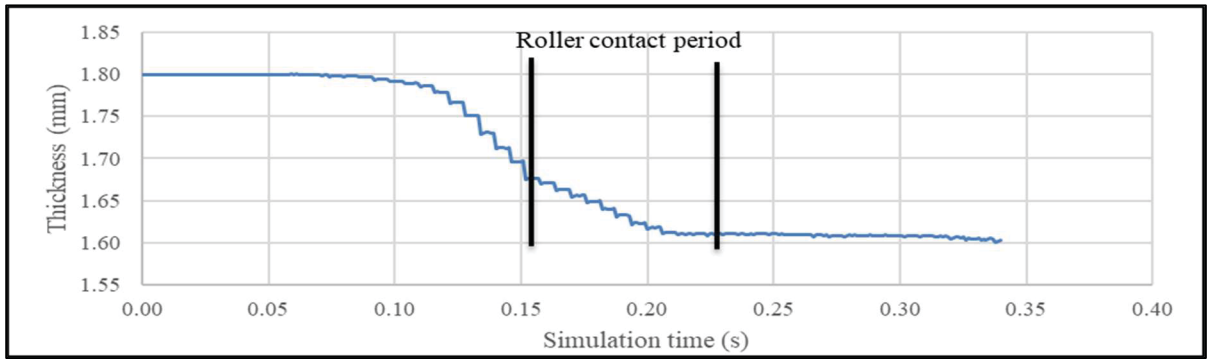

Figure 5.6 Thickness of one typical point in directed contact with roller

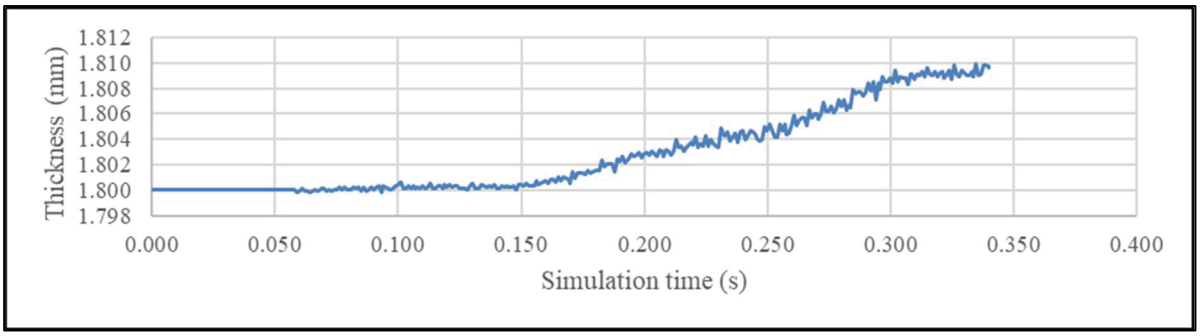

Figure 5.7 Thickness of one typical point on the flange

The thickness is observed to change prior and during the contact period with the roller and then nearly unchanged when the roller passes it.

The thickness in the undirected contact segment showed a little change of just 0.008 mm or 0.4% compared to the initial thickness. This observation can consider that thickness change is neglected in the undirected contact area with the roller.

5.5 Effect of roller path on workpiece

This problem can be solved analytically with an assumption of $x_{C_0} = x_{C_1}$, which means that the free edge (outer flange) of the workpiece is constrained to be fixed in radius. The segment AB_0 is deformed to a longer segment AB_1.

$$l_{AB_1} = \frac{l_{AB_0}}{cos(\alpha)} \tag{5.1}$$

Assuming this deformation is plastic hence the volume is consistent and can be presented by an equation (5.2).

$$l_0 \times t_0 = l_1 \times t_1 \tag{5.2}$$

The underscore numbers 0 and 1 illustrate the initial state and the deformed state respectively. The thickness of the deformed segment AB_1 can be calculated by combination of two equations (5.1) and (5.2).

$$t_{AB_1} = t_{AB_0} \cos(\alpha) = t_{AB_0} \sin(90 - \alpha) \tag{5.3}$$

The equation (5.3) is called sin law to predict the thickness in case of shear spinning. However, the conventional spinning process does not have any constraints on the flange, the solution of displacement is different from these assumptions and observed in the previous section.

5.5.1 Relationship of roller path and displacement

The length and thickness of the deformed segment AB_1 can be calculated approximately by equation (5.3). They depend on the stroke angle α and follow the sine law. The derivation of

this relation is made starting at equation (5.1) by assuming that the radial displacement (in x direction) of the point B_0 is zero so that the translation of B_0 goes to the point B_1 hence the deformed length of $AB_1 = \frac{l_{AB_0}}{\cos(\alpha)}$. However, this displacement, revealed by the simulation, is not zero but negative. The visual diagram of this displacement is shown in Figure 5.8 where the initial segment $AB_{01} > AB_0$ is deformed to the segment AB_1. Therefore, by the volume consistency, the thickness of deformed workpiece is larger than the value calculated by the sine law. This observation is reported by many articles: (Kong, Yu, Zhao, Wang, and Lin, 2017c). Moreover, this result is also agreed with many physical experiments showing that the concave path got higher thinning compared to other path geometry due to higher stroke angle approaching the later part.

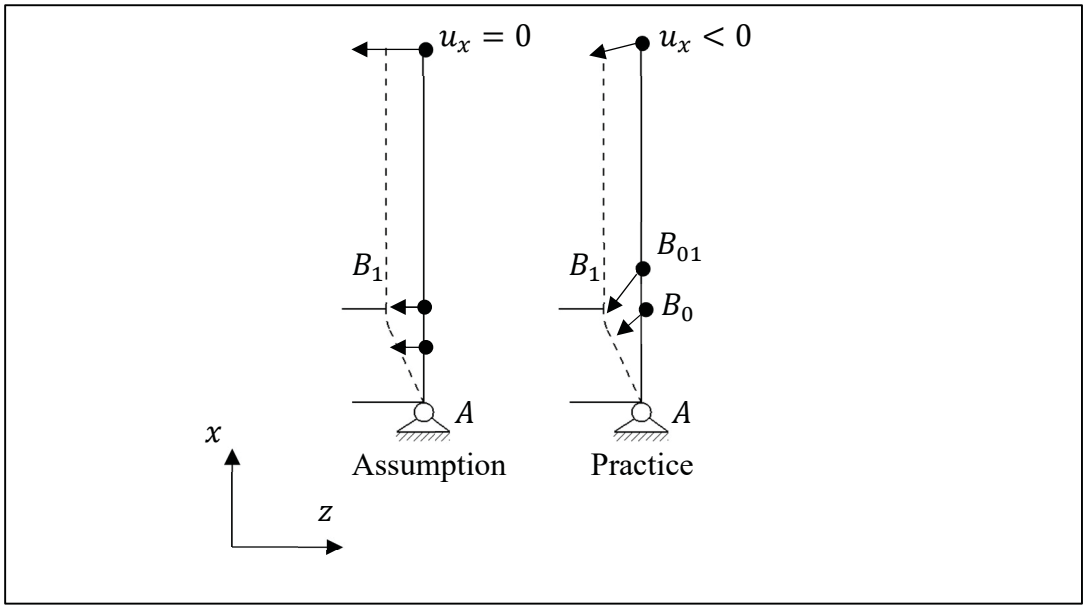

Figure 5.8 Displacement of workpiece: assumption $u_x = 0$ and practice $u_x < 0$

5.5.2 Relationship of displacement and flange circumference

The desired production has a smaller diameter $D_1 < D_0$ than the initial workpiece diameter as shown in Figure 5.8.

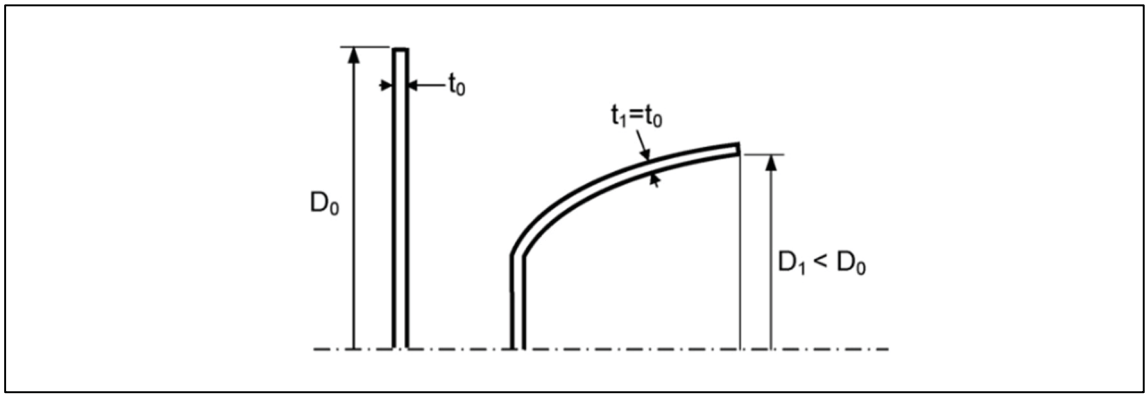

Figure 5.9 Conventional spinning: workpiece (left) and production (right)

Taken from Music (2010, p. 5)

Thus, the circumference of the flange of the production πD_1 can be clearly seen shorter than the initial one πD_0.

5.5.3 Relationship of thickness and lengths of element on the flange

The proven FEM uses the shell element formula 25 of LS-Dyna which assumes the workpiece behaves like plane stress condition with additional thickness change updated via Poisson behaviour.

$$\epsilon_{33} = \frac{\nu}{\nu - 1}(\epsilon_{11} + \epsilon_{22}) \tag{5.4}$$

The equation above shows that the thickness strain ϵ_{33} depends only the in-plane strains of circumferential direction ϵ_{11} and radial direction ϵ_{22} but not depends on stresses.

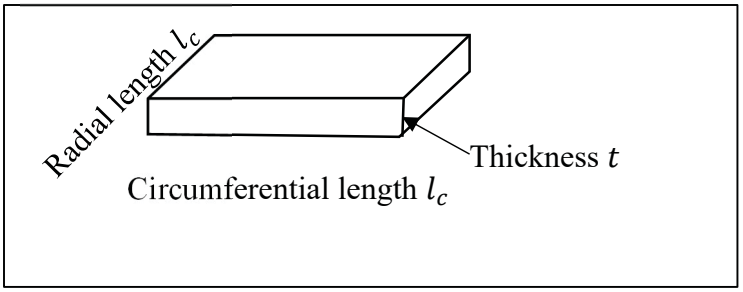

Figure 5.10 Shell element length dimensions

The volume of a shell element can be calculated approximately by multiplying three length dimensions: radial length, circumferential length, and thickness.

$$V_{elem} = l_r \times l_c \times t \tag{5.5}$$

The volume of an element in plasticity deformation stage is consistency for crystal structure of metals, hence the initial volume 0 is equal to the latter volume 1.

$$l_{r0} \times l_{c0} \times t_0 = l_{r1} \times l_{c1} \times t_1 \tag{5.6}$$

The flange circumference can be calculated as total of circumferential length of elements on the flange. The flange circumference simply equal to number of elements multiplies one element circumferential length $n_e \times l_c$.

5.5.4 Pre-wrinkle analysis

The effect of the roller path, presented in section 5.5.1, causes a reduction of the flange radius or a reduction of the flange circumference $2\pi R_{flange} = l_{c1} < 0$. In addition, the flange has a condition of volume consistency of the flange element, presented in equation (5.6), showing the multiplication $l_{r1} \times t_1$ has to be increased to satisfy this condition.

The result of the simulation, presented in section 5.3 and section 5.4, shows that the radial tensile strain on the flange or increment of radial length l_{r1} and small increment of thickness t_1. This result agreed with the analysis above.

The radial tensile strain is observed to decrease in value while approaching the flange. Hence, the element radial length l_{r1} has a small change compared to its initial one l_{r0}. If the radial tensile strain is not large enough to compensate for the decrement of the flange radius, the wrinkle, which has the property of small radius but long circumferential length, will appear to satisfy volume consistency condition.

As explained above, the wrinkle depends on the roller path, defined by feed rate f and the stroke angle α, and the radial strain of the flange.

5.5.5 Definition of wrinkle geometry and critical condition

The wrinkle part occurs only in the undirected contact part of the workpiece B_1C_1, shown in Figure 5.1. This geometry can be defined by two parameters: the relative displacement δ, shown in Figure 5.11, is the z displacement between the roller tip and the z coordinate of flange nodes; the number of maxima and minima peaks with their angle versus an x axis, shown in Figure 5.12.

Thus, these two parameters can be illustrated as a graph, shown in Figure 5.13. The geometry of the wrinkle can be seen as a wave geometry with magnitude is the relative displacement δ and maxima and minima peaks.

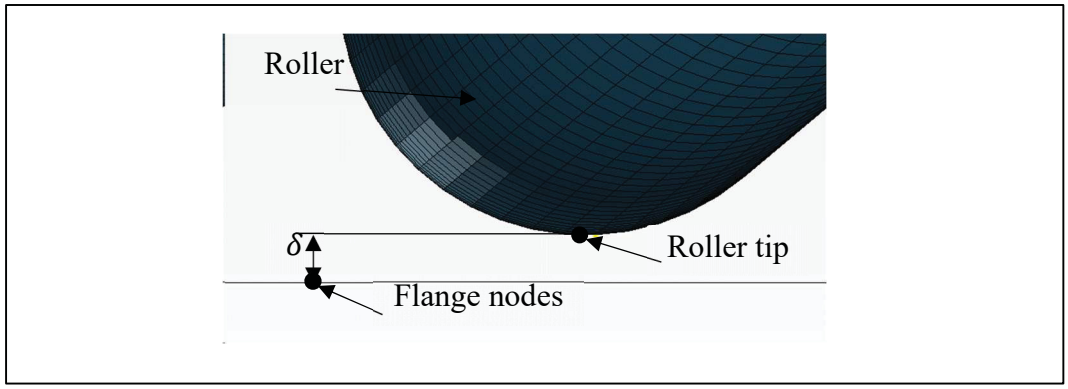

Figure 5.11 Relative displacement δ between the flange and the roller tip

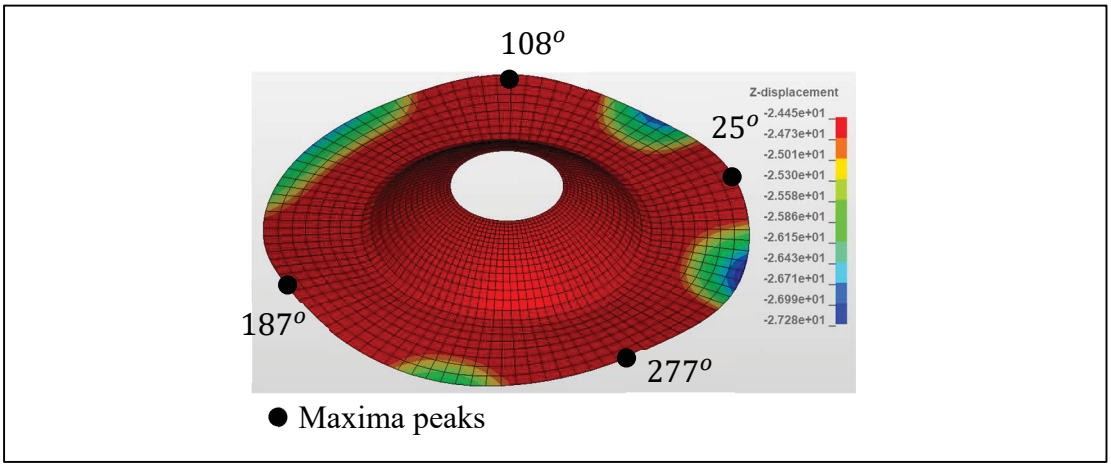

Figure 5.12 Maxima peaks corresponding to their angle versus x axis

The magnitude of the wrinkle can be considered a critical condition in which the metal spinning process cannot execute further due to extreme vibration of the workpiece.

Therefore, the goal of a successful process is to keep the magnitude of the wrinkle less than a critical condition defined by $\delta < 3$ mm.

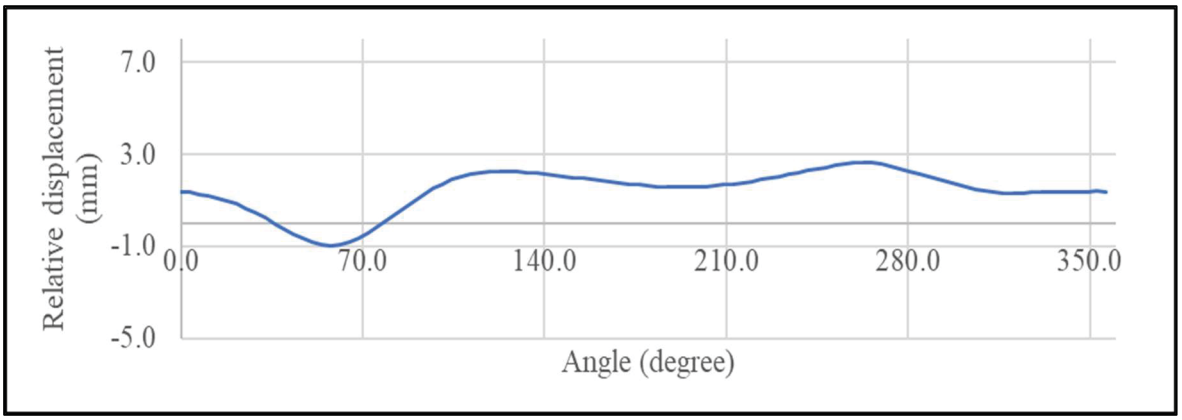

Figure 5.13 Relative displacement of the flange versus roller contact point in z direction

5.5.6 Post wrinkle initiation analysis.

The initial wrinkle, analyzed in section 5.5.4, page 80 is caused by the roller deformed the initial segment AB_0 to the tensile segment AB_1. As a result, the circumference of the flange reduces but the flange radial tensile strain is not large enough to compensate for this reduction causing the wrinkle to occur. Thus, the more deformation of the workpiece the roller made, the more wrinkle magnitude or wrinkle severity the workpiece has.

However, many articles reported that the wrinkle can disappear after the wrinkle is detected by using a more relaxed roller path. This fact is observed only by experiment (Kong, Yu, Zhao, Wang, and Lin, 2017b). This section provides an explanation about how post-wrinkle works by extension the hypothesis of pre-wrinkle analysis.

The section 5.5.4, page 80 showed a reaction of the flange to satisfy the volume consistency by producing new peaks to help maintain its circumference. Figure 5.15 showed the progress of the new maxima peak created between two existing peaks.

Figure 5.14 showed the simulation value of the number of peaks versus the wrinkle magnitude curve (be fitted). The wrinkle magnitude started at 1.7 mm, increased to 9.8 mm then reduced significantly to around 1.7 mm while the number of peaks increased gradually.

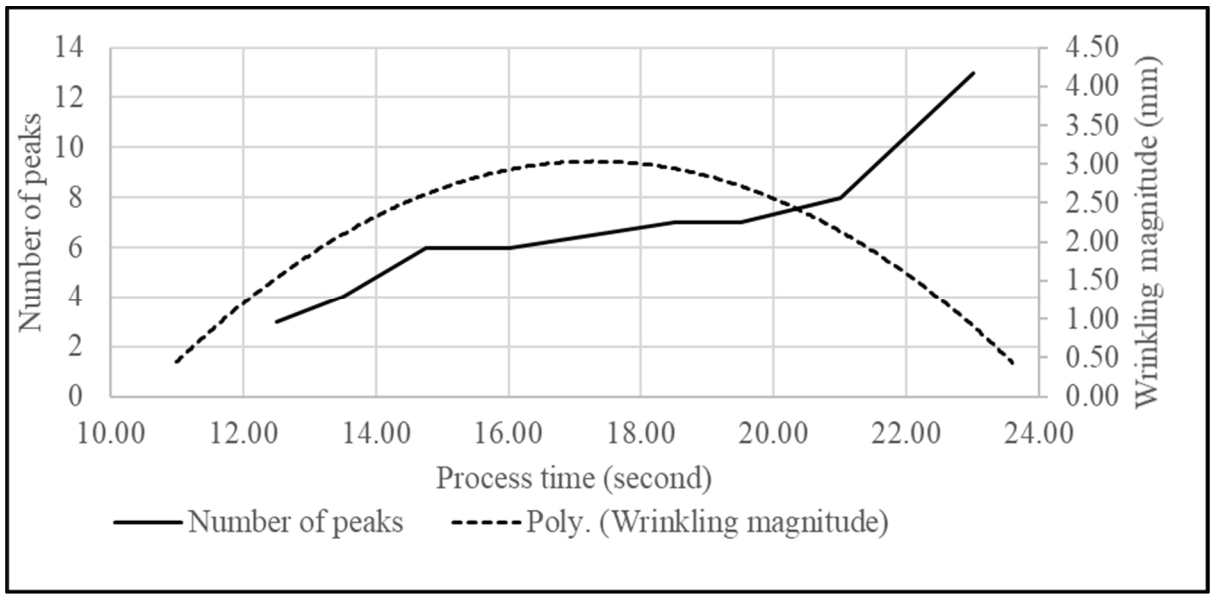

Figure 5.14 Wrinkle magnitude when recovery path at 30^o

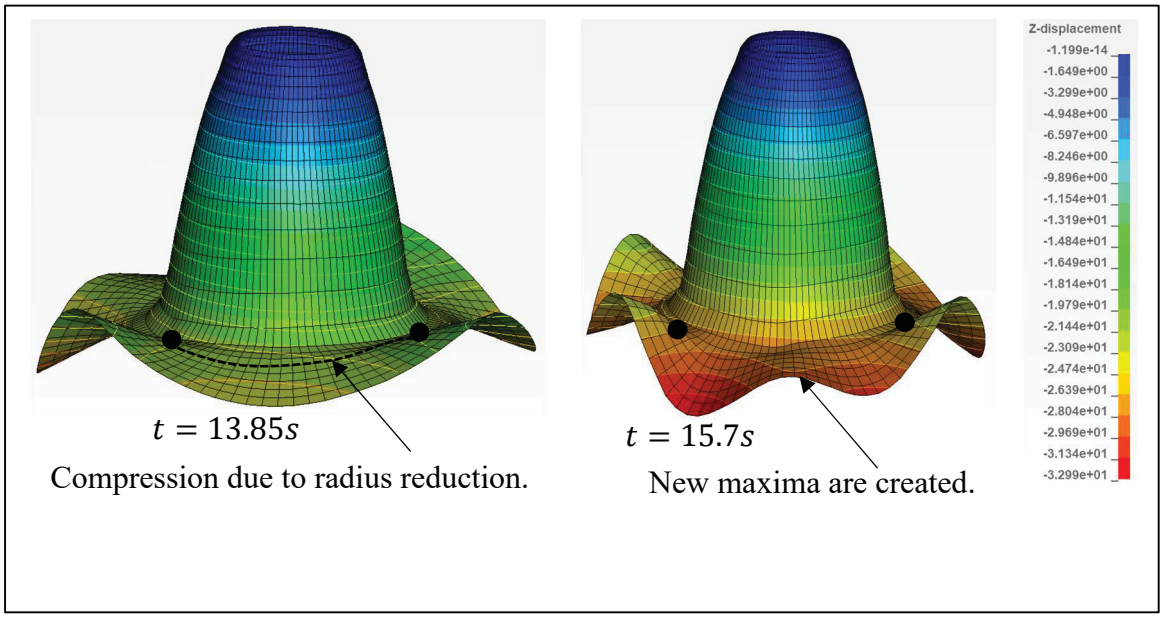

Figure 5.15 Development of new maxima and minima (displacement is scaled 5 times bigger than original)

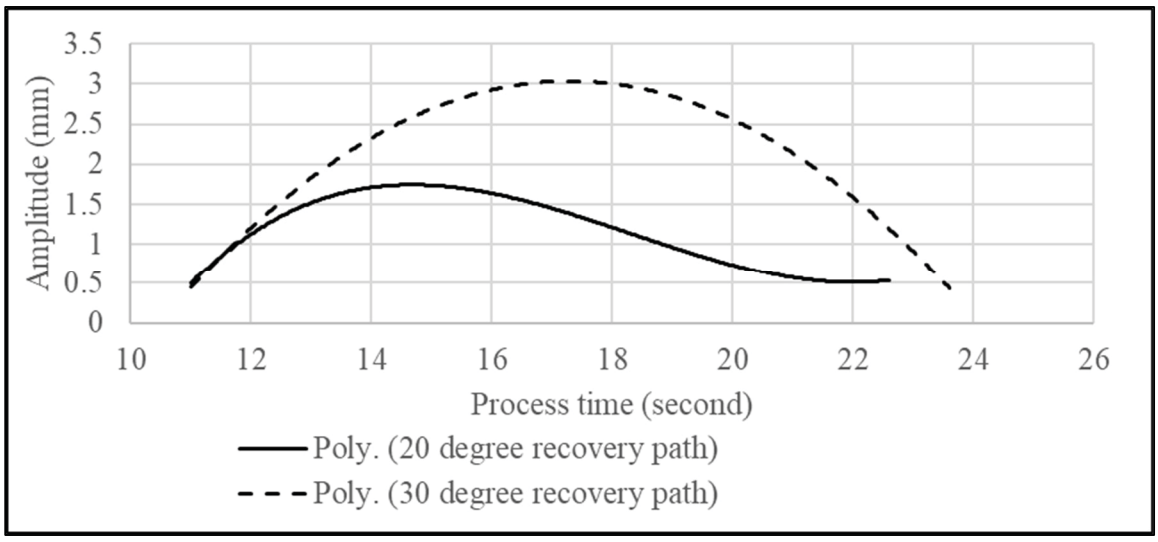

Figure 5.16 Wrinkle magnitude between the recovery path of 20^o and 30^o

If the feed rate f is kept constant during the process, the roller path depends solely on stroke angle α. The more stroke angles the roller has, the more wrinkle magnitude the flange occurs. At the same time, the increase of peak number will reduce the wrinkle magnitude. Therefore, the proper stroke angle is chosen such that the wrinkle magnitude is kept at the safe threshold. Figure 5.16 showed the wrinkle magnitude curve versus two different stroke angles 20^o and 30^o. The smaller stroke angle 20^o showed a significant smaller wrinkle magnitude of 1.7 mm versus 3.0 mm compared to the stroke angle 30^o.

Thus, by a combination of controlled stroke angle, the number of peaks increases as well as keeping magnitude not exceeding the threshold, the wrinkle can be flattened.

The wrinkle geometry is shown in Figure 5.17. It shows the waving geometry including two main output characters: the number of peaks and the amplitude. One example of this output is shown in Figure 5.18. The amplitude and the number of peaks history during the spinning

process is shown in Figure 5.19. Both experiment and simulation showed that the plate has its wrinkle initiation at about 40 degrees which is at the time 9.8 second. The wrinkle initiation can be seen on this diagram at the time 9.8s and corresponds to the appearance of the third peak.

The number of peaks is seen to increase from two to four corresponding to the initial stage and severe wrinkling respectively. In addition to the wave geometry of the flange, the hypothesis of the relationship between the number of peaks and the amplitude is proposed.

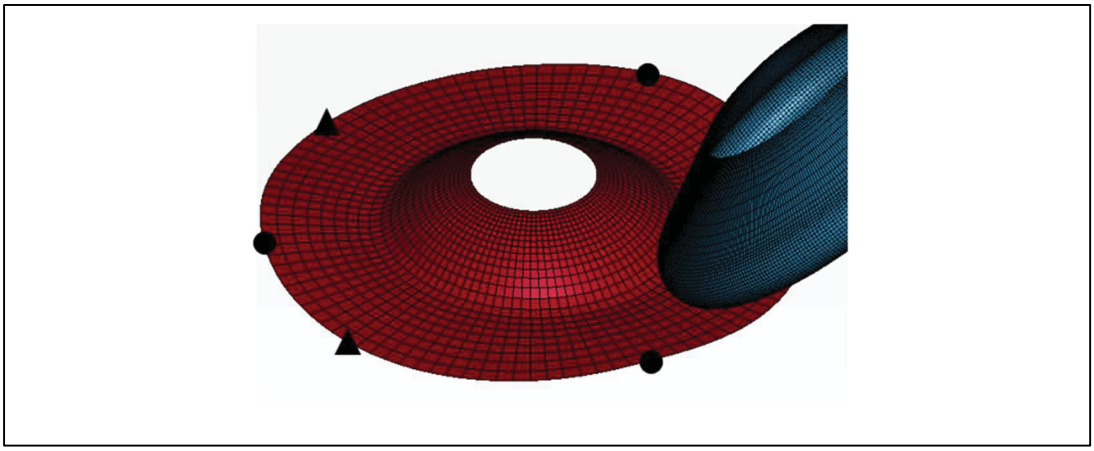

Figure 5.17 Flange wrinkle geometry: 3 maxima (dot) and 3 minima (triangle)

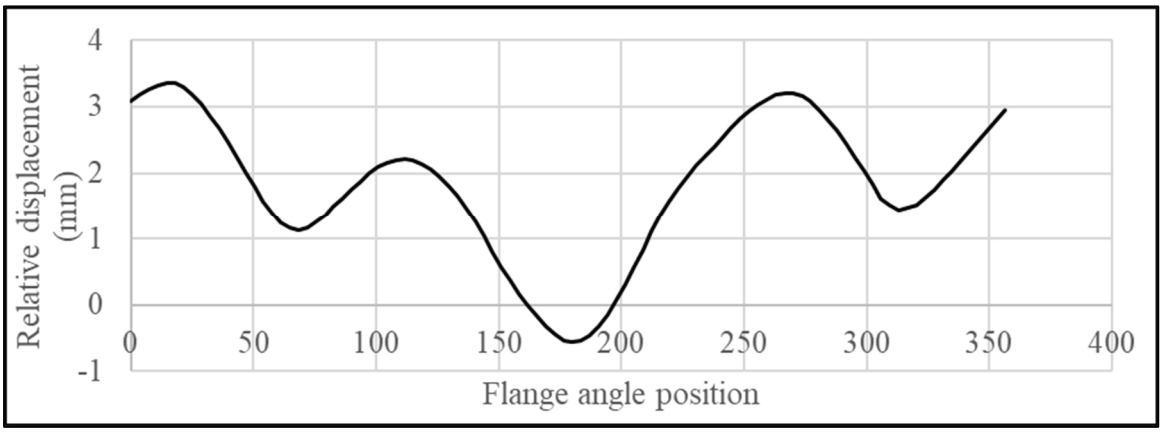

Figure 5.18 Diagram of flange z-coordinate versus the roller tip

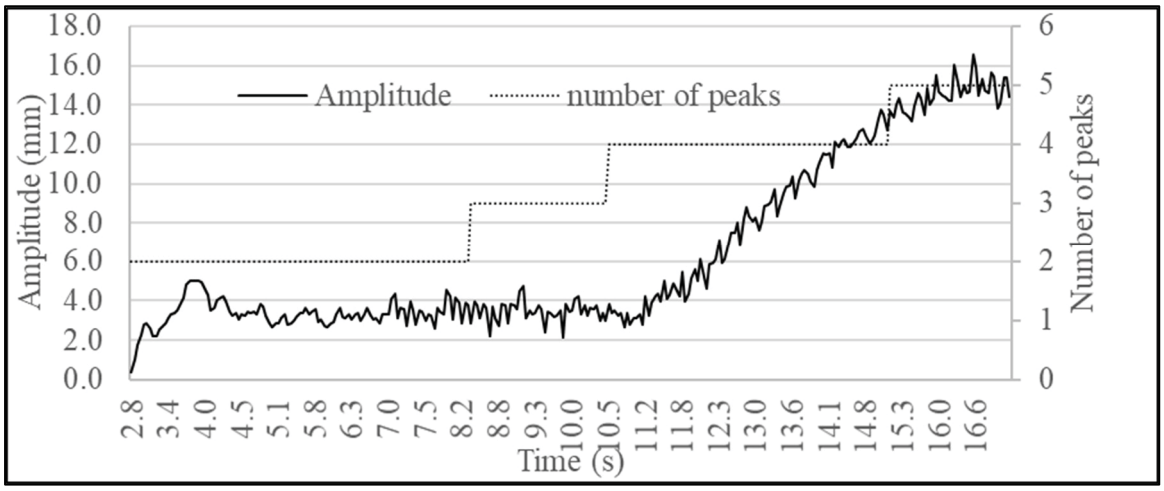

Figure 5.19 Amplitude and number of peaks versus time

Relationship between the number of peaks and the amplitude

The volume of an element in the plastic deformation phase does not change for metals with a crystalline structure.

$$V_{elem} = l_r \times l_c \times t = constant \tag{5.7}$$

The roller deformed the plate locally at the middle of the plate as shown in Figure 5.20. In addition, the flange has no constraints on the edge, hence the thickness t and the radial length l_r can be considered as having little variation. The change value of the thickness and the circumference of the flange is shown in Figure 5.21. The thickness changes 0.3% from 1.8 to 1.8055 mm and the circumference changes 0.0689% from 621.04 to 621.468mm.

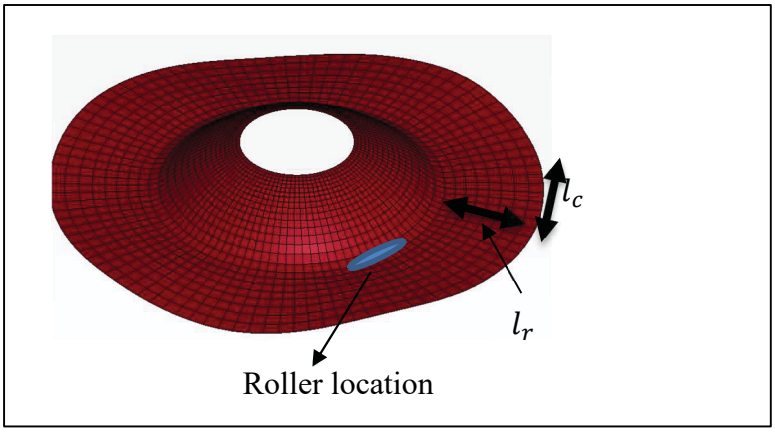

Figure 5.20 Flange element length dimensions

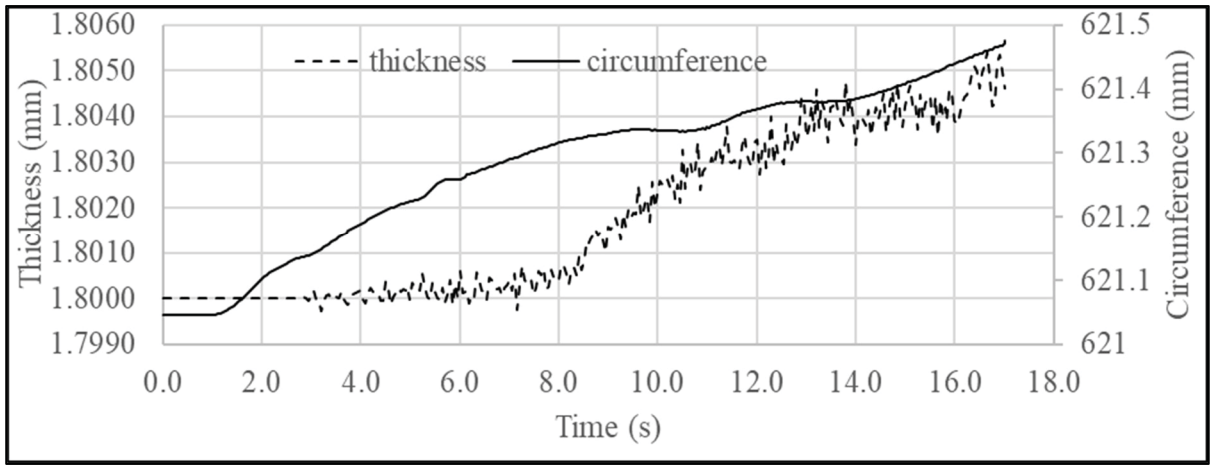

Figure 5.21 Thickness and circumference of the flange over the processing time

Therefore, the circumference of the flange can be considered as constant. This assumption is only seasonable as long as the roller has not deformed the edge yet.

Considering the waving geometry, the circumference or the length of the wave remains constant, then the number of peaks increases but the amplitude decreases.

In Figure 5.19 when the number of peaks reaches 3 at time 8.25s, the amplitude decreases. Severe wrinkling happens at time 10.25 when the amplitude increases suddenly with the slow growth of the number of peaks.

5.5.7 Circumferential cracking formulation

The metal spinning formulation, defined in section CHAPTER 5, page 71, bases on the assumption that the roller deformed completely the initial segment AB_0 to the deformed tensile segment AB_1. The sign of complete deformation is observed by the highest strain appearing on just adjacent the roller contact area as shown in Figure 5.5. There is an observation that this assumption does not always happen in which the roller cannot deform the workpiece right at the contact area as a case shown in Figure 5.22 where the highest deformed location defined by the effective plastic strain is far away from the roller and nearby the tailstock clamp location. Therefore, another formulation is recognized and presented in this section.

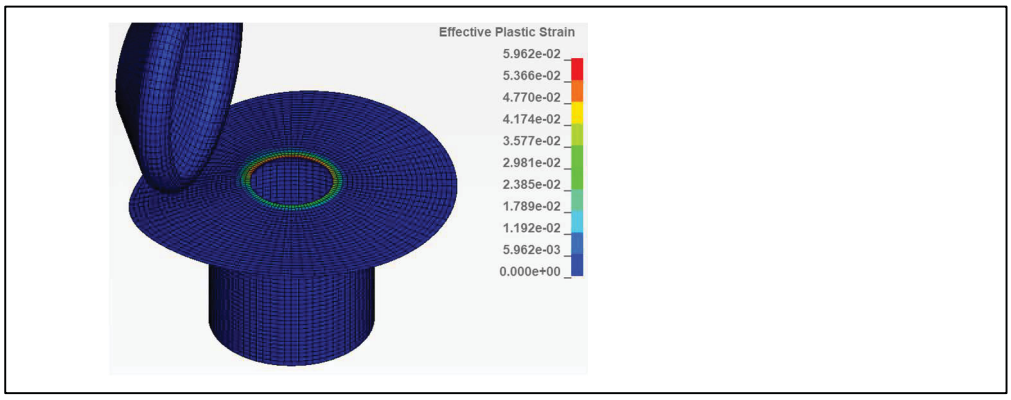

Figure 5.22 Deformation location indicated by effective plastic strain

The displacement of the workpiece in this situation is shown in Figure 5.23 where the maximum displacement in z direction corresponds to the location (1) of the roller contact area. The opposite location (2) through the center showed a similar negative displacement but with smaller value. Two perpendicular areas (3) and (4) showed the opposite displacement direction with two other locations.

The circumference of the flange varies slightly from 621.046 mm to 621.52 mm during 30 mm of stroke depth. In addition, the roller moves further in z direction, the displacement of location (1) and (2) are displaced deeper in the negative z direction causing the perpendicular location (3) and (4) are displaced higher in positive z direction to maintain the circumference of the flange.

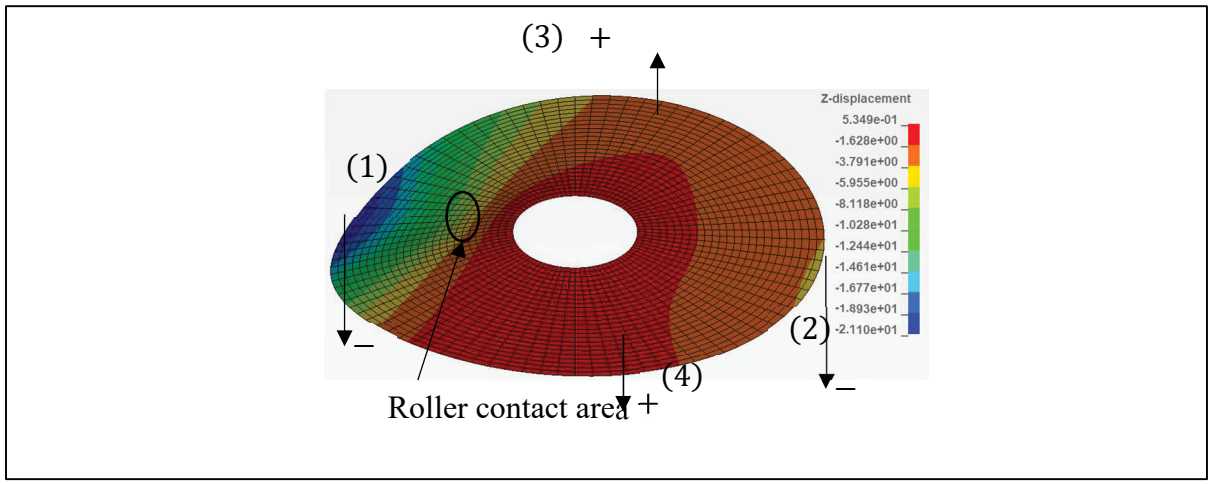

Figure 5.23 Development of displacement in a circumferential cracking case

The higher displacement in positive z direction causes the strain to build up near the fixed area between the tailstock and the workpiece. Eventually, the workpiece cracked at this location. This situation is consistent with the experiment shown in the article (Nguyen, Champliaud, and Lê, 2020), validated by the GSSMO model.

One interesting point is that this situation looks like a wrinkle with two maxima peaks and two minima peaks. However, the number of peaks does not increase to reduce the magnitude of the wrinkle because the roller cannot completely deform any segment through its stroke path.

5.6 Application

Based on the proposed hypothesis and observation above, the wrinkle is usually unavoidable unless the flange has a high-radial in-plane strain or the flange diameter is close to the roller.

This is verified by a simulation, shown in Figure 5.24, with a successful process with a workpiece radius of 80 mm instead of 100 mm.

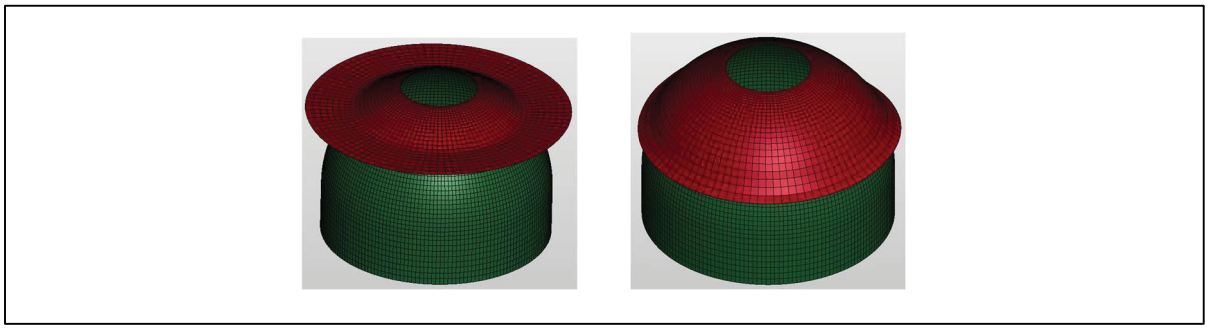

Figure 5.24 Successful production with smaller workpiece diameter $R80$ mm instead of $R100$ mm

Based on the analysis of post-wrinkle, the winkle is fixable by relaxing the roller stroke angle so that the increase of the peak number can reduce the amplitude to a safe value.

Based on the analysis of circumferential cracking, the stroke angle is chosen to be large enough to always make a deformation on the workpiece otherwise the circumferential cracking develops.

5.6.1 Proposed wrinkle-free roller multi path

The possibility is that the stroke angle remains large (path 1-a) as shown in Figure 5.25 compared to the small stroke angle of paths (1-b, 1-c, 1-d) hence the increment of number of peaks is not fast enough to decrease the amplitude.

Therefore, the smaller stroke angle paths, called the intermediate paths, are investigated to verify this hypothesis.

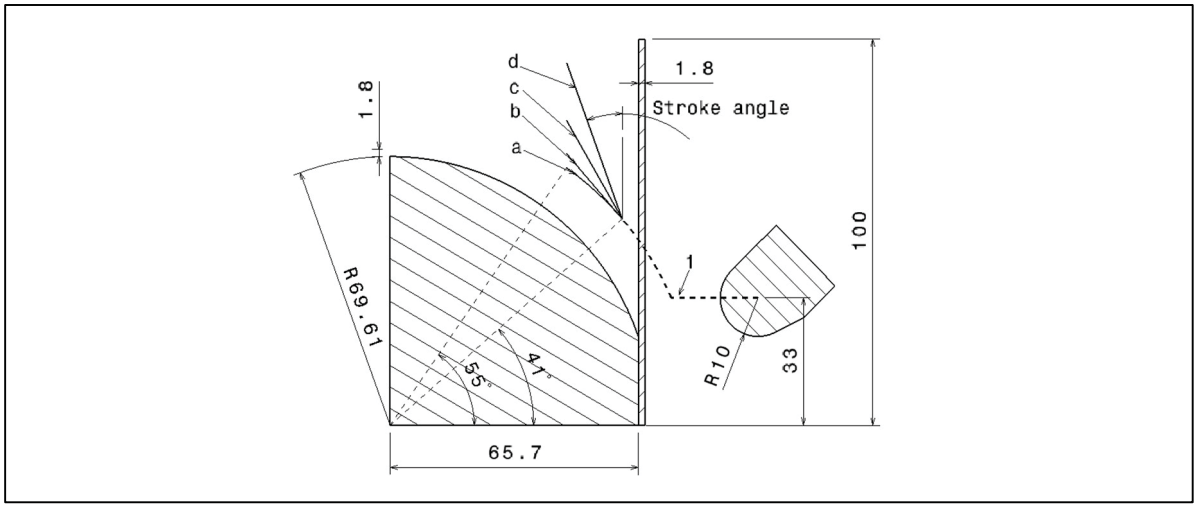

Figure 5.25 Investigate 3 intermediate paths: 1b with stroke angle 41 degrees, 1c with stroke angle 30 degrees, 1d with stroke angle 20 degrees

5.6.1.1 Investigation of 3 intermediate stroke angles

Figure 5.25 shows the sketch of the metal spinning process with 3 various intermediate stroke paths. These paths start at the angle position 41^o, where the wrinkle is on-set. The path 1-a is the direct path used in the experiment and simulation in the above section. Three intermediate paths with smaller stroke angle are included: 1-b with stroke angle 41^o, 1-c with stroke angle 30^o and 1-d with stroke angle 20^o.

The intermediate path 1-b with a stroke angle of 41^o showed the same trend of sudden change in amplitude as the direct path but path 1-b results in a smaller amplitude value. At the end of the process, the amplitude of path 1-b decreases significantly to the safe value due to the increasing number of peaks, up to 8.

The intermediate path 1-c with a stroke angle of 30^o showed a growth of the amplitude in the safe range of 6 mm. The number of peaks goes up to 7.

The intermediate path 1-d with a stroke angle of 40^o showed a constant amplitude during all processes. The number of peaks remains at 4. This can be considered as the best intermediate path for this process.

Finally, the second direct path needs to be applied in order to deform the plate to the desired location.

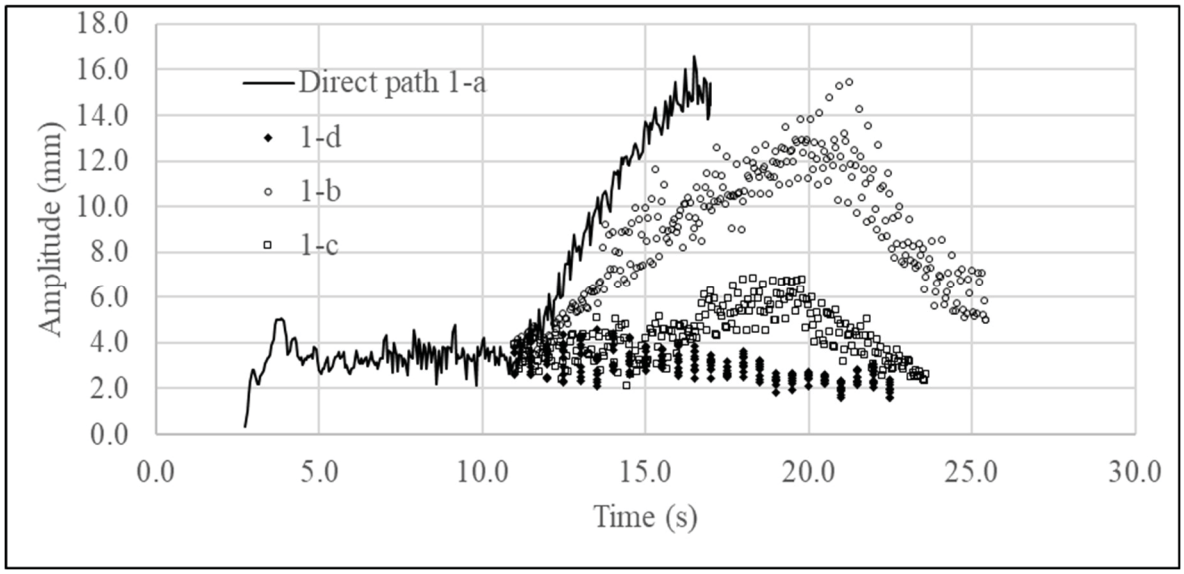

Figure 5.26 Amplitude of the direct path and three intermediate paths

5.6.1.2 Investigation of second stroke after intermediate path

This state illustrates the deformation of a segment AB_0 to a segment AB_1, shown in Figure 5.27. The deformed segment AB_1 is longer than its initial segment AB_0, hence the deformed segment AB_1 probably has radial tensile strain.

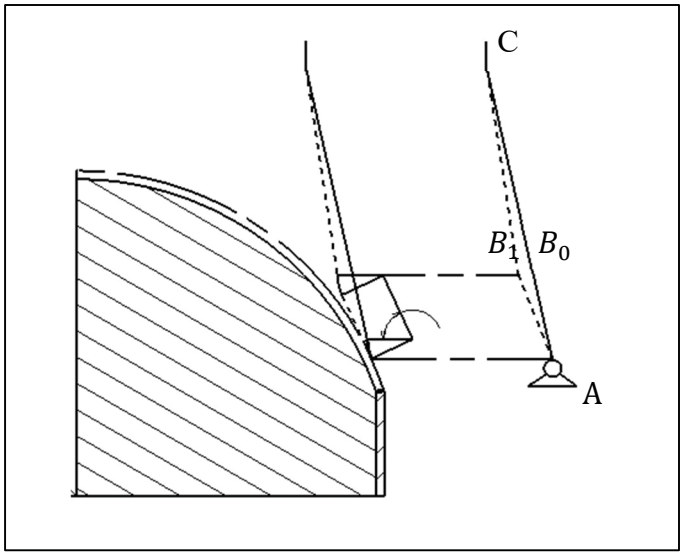

Figure 5.27 Second pass formulation

The segment B_1C is longer than the segment CB_0, hence the segment B_1C probably has radial compressive strain which contrasts to the first pass formulation, analyzed in section 5.3, page 74. Therefore, this state can be seen as a wrinkle free stroke. The flange diameter, as shown in Figure 5.28, is nearly horizontal during a duration of stroke free from time 0.4 to 0.64.

The process will return to the first pass formulation when the point B_1 and the flange C are in the vertical plane. The flange diameter of this stage, shown in Figure 5.28, reduces gradually and shows wrinkles again.

This analysis is agreed to other experiments: (Polyblank and Allwood, 2015).

This section investigates the direct path from the wrinkle initiation location 41^o to the final location at 55^o after utilizing the intermediate path “1-d”. The complete path is shown in Figure 5.29, noted path “1-d-2”.

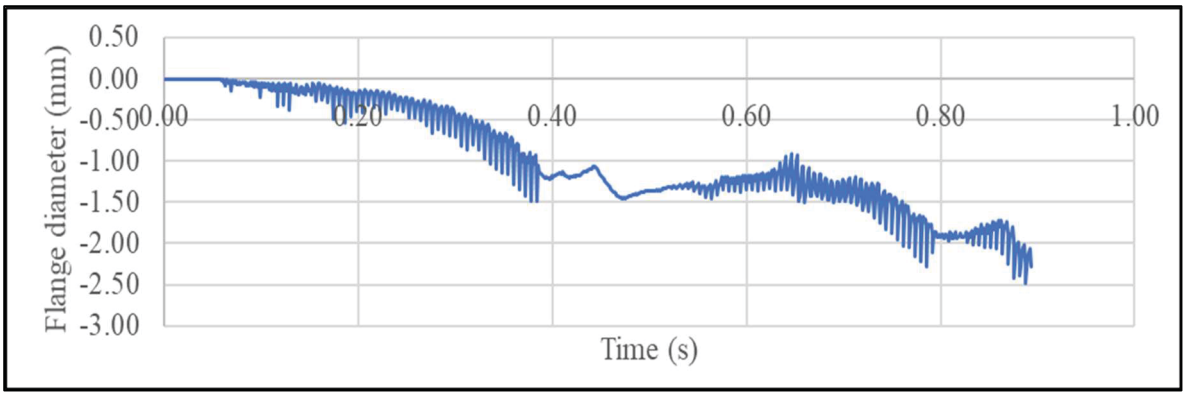

Figure 5.28 Flange diameter during spinning process

The amplitude of the second path "1-d-a" is shown in Figure 5.30. The final amplitude is about 4 mm, significantly smaller than the final amplitude of direct path "1-a" 15 mm. However, the processing time 31.65s is longer than the direct path "1-a" 16.5s due to the intermediate path "d".

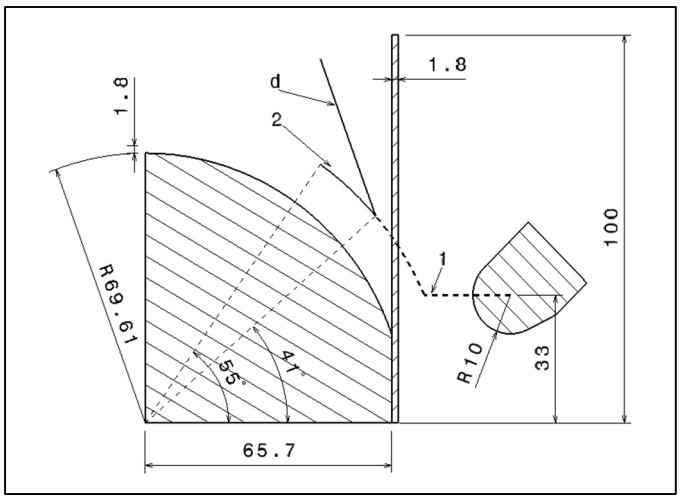

Figure 5.29 Second stroke "1-d-2"

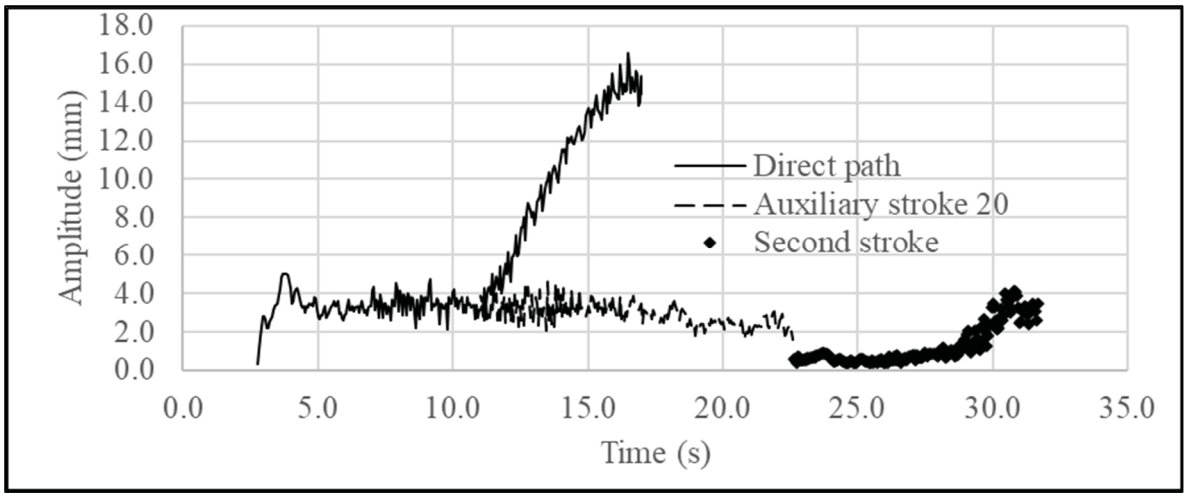

Figure 5.30 Amplitude's comparison between the direct path "1-a" and the second path "1-d-a"

Finally, it is shown that extra forming paths are efficient for successfully completing the spinning process but at the expense of the processing time.

Therefore, the first solution of roller design paths shown in figure Figure 5.31 below contains two steps. The first step is to use the final path, which is a path following the mandrel geometry as close as possible, until wrinkles on-set. The second step is to use a loop of paths containing one relaxed straight path with an angle about $\beta = 20^o$ to vertical and one final path with a distance $\cos(\beta) \times l_{flange}$, which is a distance of wrinkle-free stroke described in Figure 5.32.

Figure 5.31 shows a final path to the point of wrinkle on-set. Figure 5.32 shows a relaxed path to remove a wrinkle. Figure 5.33 and Figure 5.34 show a complete path in the second combination and the previous combination.

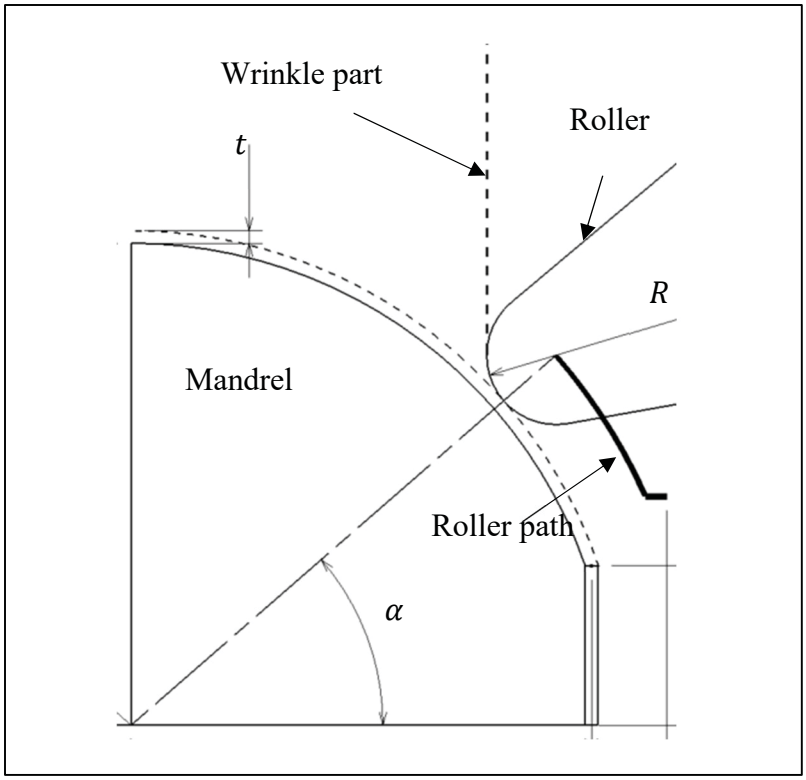

Figure 5.31 First path: stroke

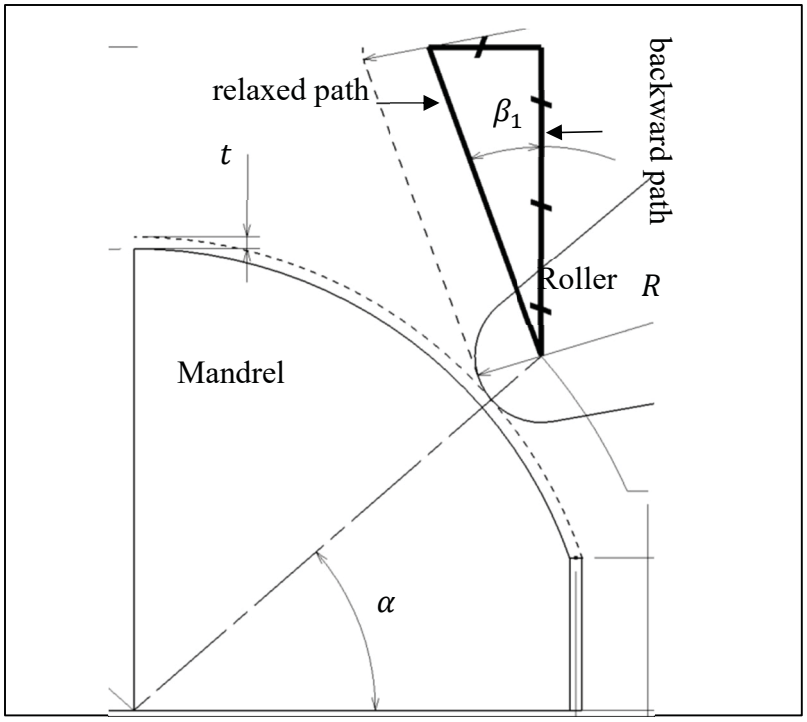

Figure 5.32 Second path: wrinkling recovery

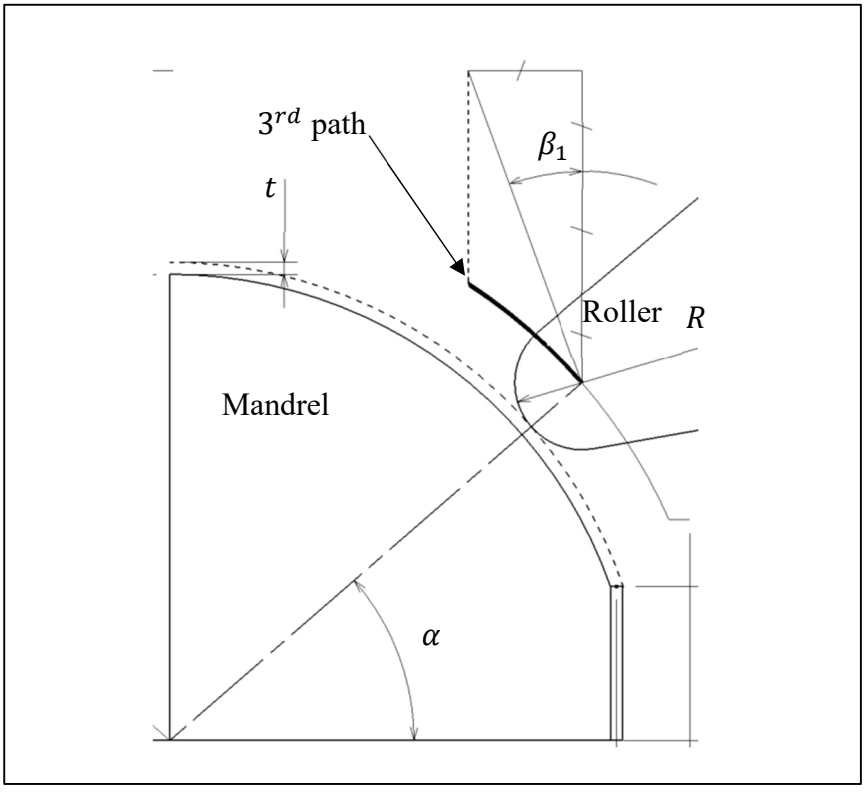

Figure 5.33 Third path: stroke

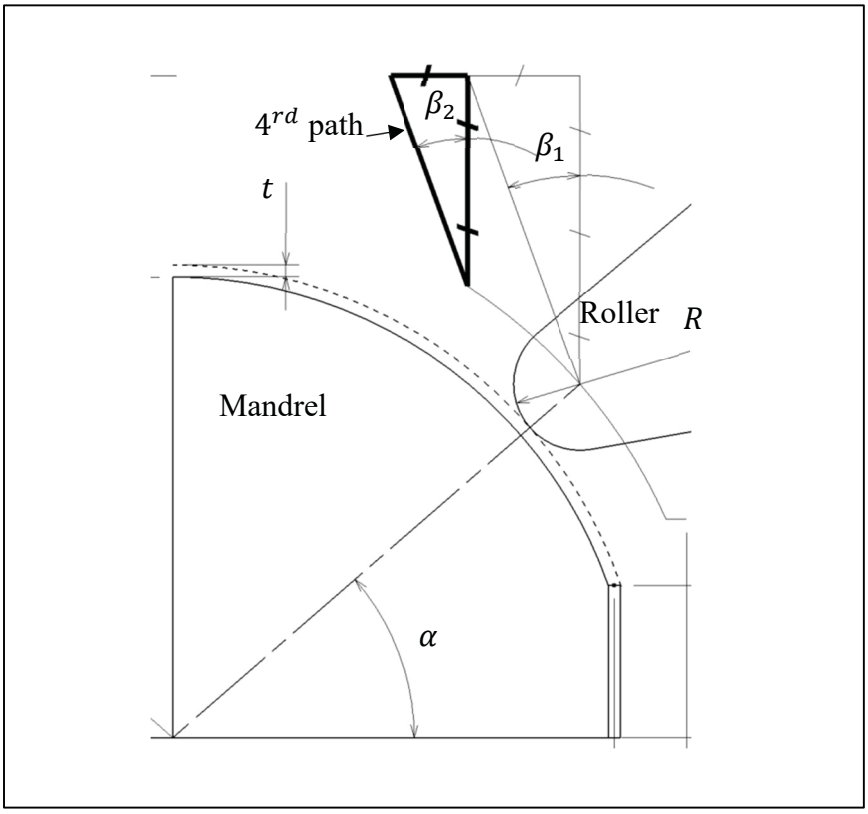

Figure 5.34 Fourth path: wrinkling recovery

5.6.2 A correlation to conventional path

As a combination of two paths: the stroked path and the relaxed path, one new path is constructed as a concave involute hyperbola path as shown in Figure 5.35.

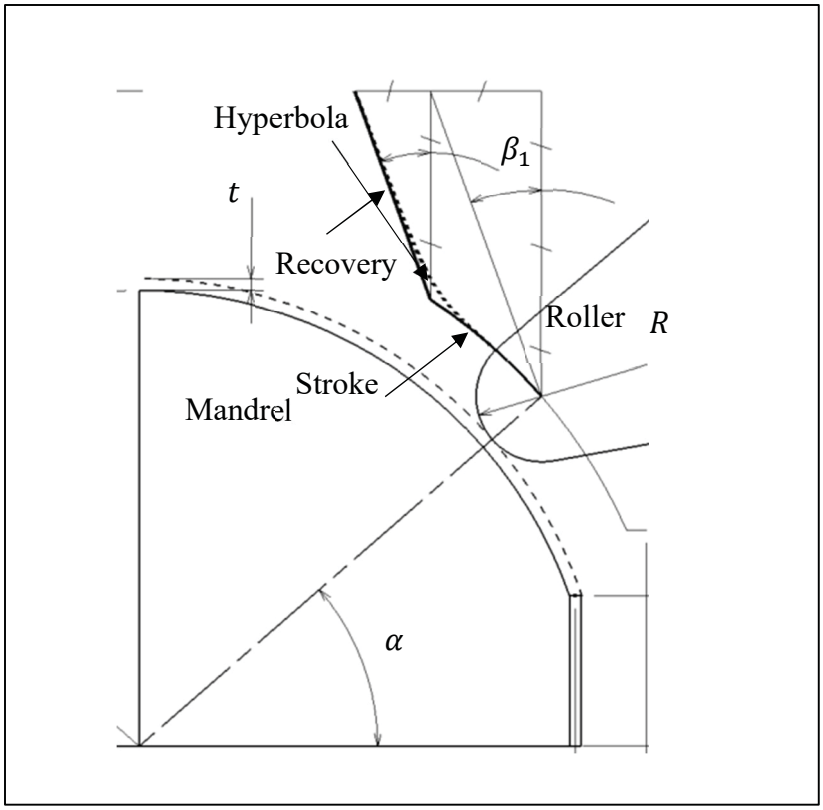

Figure 5.35 A concave involute hyperbola path

The geometry of this path is used popularly by experienced craftsmen and confirmed by many articles so far.

The complete multi-path is shown in Figure 5.36, which is designed with an initial point where wrinkle on-set; a fixed relaxed stroke angle $\beta = 20^o$.

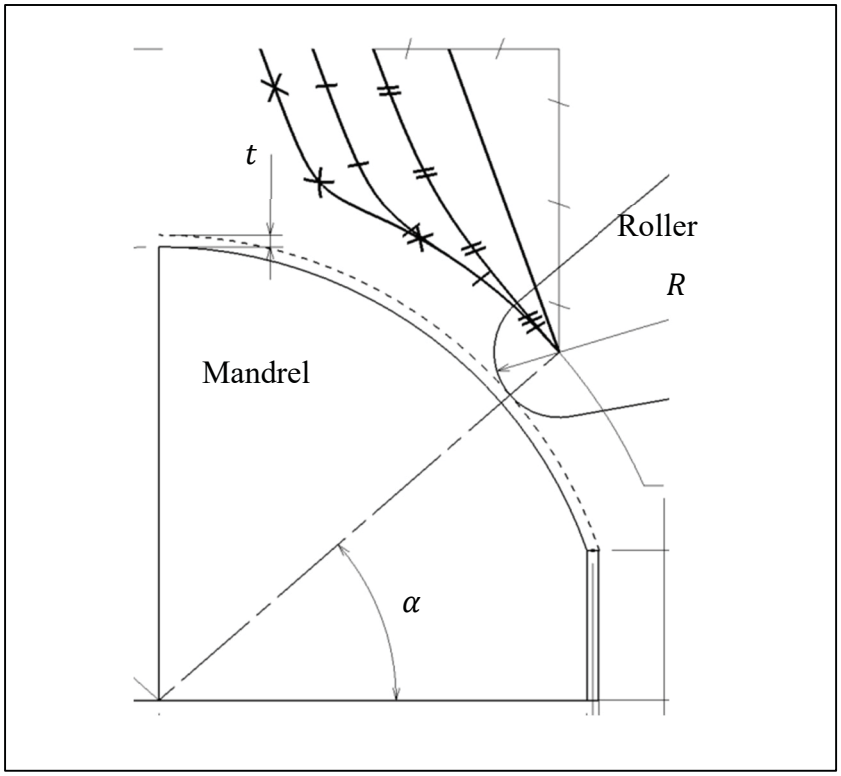

Figure 5.36 Hyperbola forward paths: stroke

5.6.3 Optimized thickness by intermediated paths

This section addresses a thinning problem of the metal spinning process. Based on the concept of volume consistency, successfully explained the process formulation, intermediate paths are introduced to improve the product thickness.

Figure 5.37 shows a sketch describing the conventional path versus intermediated paths. The length of the undirected part, not yet contacted by the roller, is the difference between two configurations. This length D_1B_1 is shorter than C_1B_1 or the length of deformed part is larger in case of intermediated paths. Therefore, the thickness of the final part AC_1 in case of intermediated paths is higher than the conventional one.

The applied simulation result of thickness, shown in Figure 5.38, indicates the minimum thickness is 1.56 mm and 1.38 mm for intermediated path and conventional path respectively.

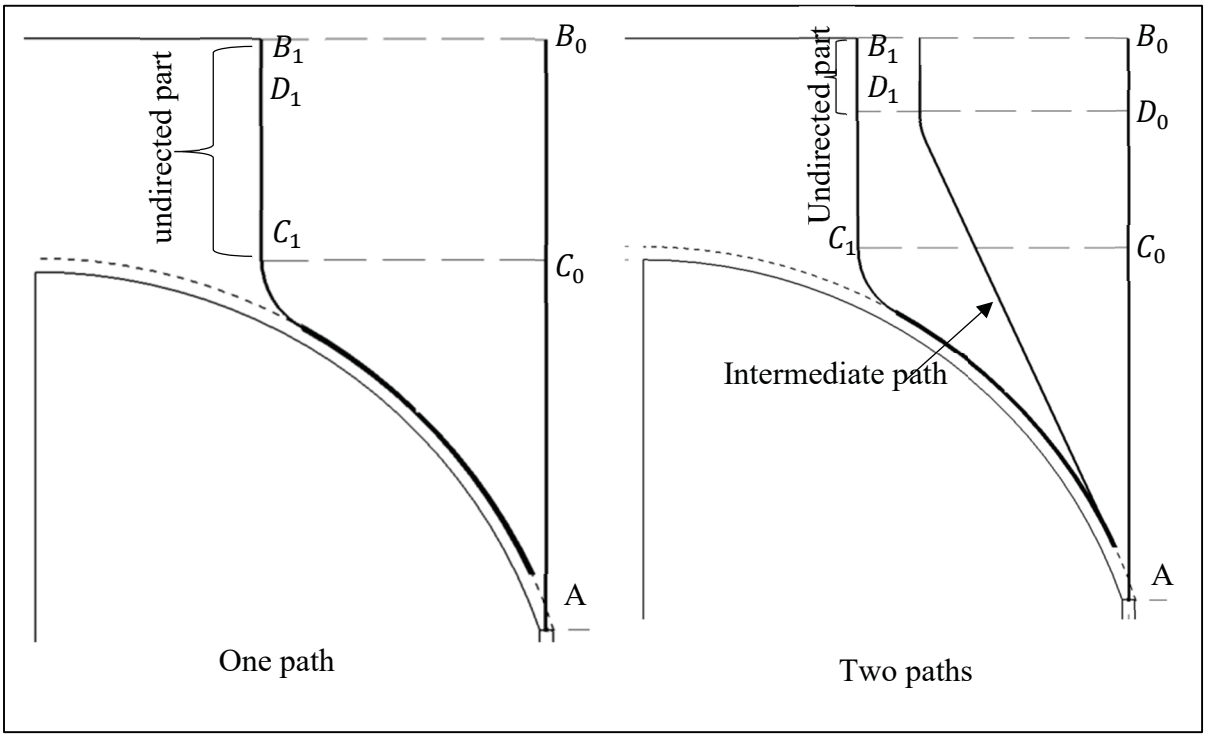

Figure 5.37 Comparison of one path and two paths with one intermediate path

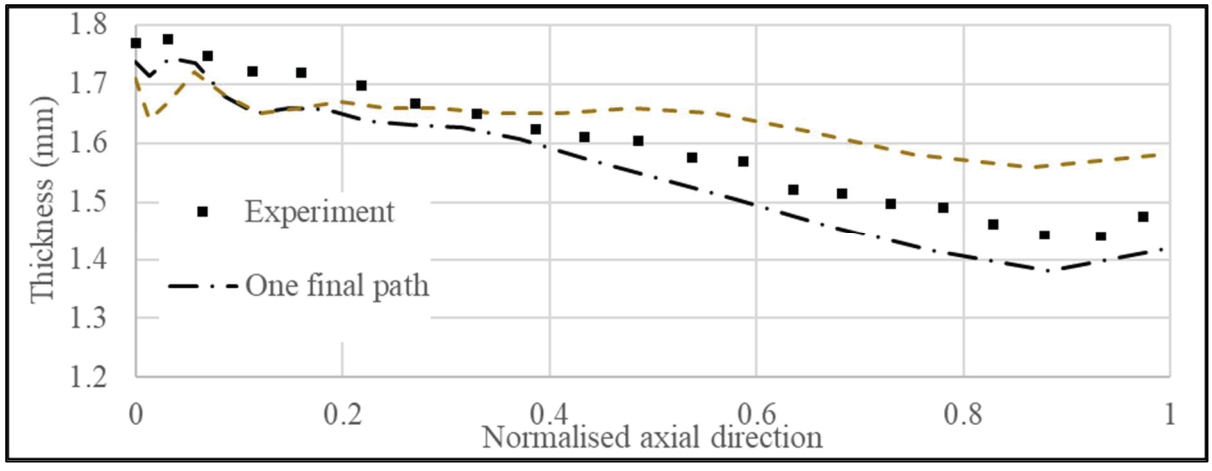

Figure 5.38 The thickness is improved by using an intermediate path

5.7 Summary

The chapter proposed and verified a hypothesis regarding the influence of roller paths on defects such as wrinkles, thinning, and circumferential cracks in metal spinning processes.

In the context of the rotating reference frame, the flange geometry after the wrinkle initiation is investigated, including the number of peaks and their amplitudes. Using this new approach, it was found that the number of peaks gradually increases from 2 to 8 peaks, while their amplitude decreases. In the case of severe wrinkles, the number of peaks stays at 4, while the amplitude increases dramatically. The intermediate path proves capable of increasing the number of peaks while maintaining a low amplitude. The path can be divided into two parts: pre-wrinkling part and post-wrinkling part. A modification in the pre-wrinkle part, reducing the thinning effect by up to 13%, is proposed.

The study of three various intermediate paths reveals the potential of designing a multi-path strategy for achieving a successful metal spinning process. While the simple straight intermediate path could yield satisfactory results, preliminary findings suggest that a curved trajectory might offer enhanced outcomes, a hypothesis deserve future investigation.

Guidelines for roller path optimization include:

- Ensuring continuous deformation at the contact interface otherwise development of circumferential cracking.
- Employing relaxed or reduced-stroke-angle paths to restore wrinkles to acceptable levels.
- Utilizing intermediate paths to mitigate thinning in the final product.
- Recognizing that workpiece thickness may be influenced by stroke angle and flange condition.

CONCLUSION

In conclusion, this chapter synthesizes the key findings of the study in relation to the research aims and discusses their significance, value, and contribution to the field. Additionally, it acknowledges the limitations of the study.

The research has successfully addressed the primary aim of the thesis, which is to understand the toolpath geometry, identifying it as comprising two essential components: the main path, following the mandrel geometry, and the intermediate path, utilized to mitigate wrinkling on the flange. By leveraging these patterns, multiple toolpath geometries can be generated iteratively until achieving the desired final product.

The three objectives outlined in the thesis have been effectively tackled. Firstly, a novel analysis employing a three-dimensional finite element model in a rotating reference frame has been introduced. This new model exhibits superior accuracy in terms of value error and trend compared to conventional models, coupled with a remarkable 50-fold reduction in computational time. Secondly, the Generalized Incremental Stress State dependent damage model (GISSMO) has demonstrated its capability to predict circumferential cracking in the metal spinning process. Thirdly, the analysis of the process within one full rotation has been proposed, revealing significant insights into the relationship between flange wave geometry parameters based on the volume-consistent properties of the metal material during plastic deformation. Notably, the constancy of the flange circumference leads to contrary changes in wrinkle amplitude and the number of peaks. The intermediate path emerges as a tool to increase the number of peaks, thereby minimizing wrinkle amplitude - a novel insight into the wrinkling phenomenon of the metal spinning process. This approach serves as a new predictive model for post-wrinkling occurrence, aiming at the elimination of wrinkles rather than merely attempting to avoid their appearance.

Limitation of the study:

- Fixed Feed Rate Assumption: Despite providing a comprehensive analysis that includes multiple paths, a significant limitation of this study is the assumption of a fixed feed rate. The mechanism theory is developed based on the consideration of one revolution of the mandrel, leading to the assumption that the feed rate remains constant throughout the process.
- Assumption of plasticity deformation by the roller: another limitation is the assumption that the roller consistently induces plastic deformation on the plate. While this assumption simplifies the theoretical framework, it may not always align with practical conditions.

RECOMMENDATIONS FOR FURTHER RESEARCH

- Investigation of Feed Rate Influence: Integrating the feed rate into the comprehensive analysis of the mechanism theory could yield novel insights and potentially uncover original findings.
- Validation of Circumferential Cracking Caused by Inadequate Plastic Deformation: The assumption that circumferential cracking in metal spinning is solely caused by inadequate plastic deformation induced by the roller warrants further validation. Conducting experimental studies to directly observe and measure the deformation behavior under different roller pressures and material properties can provide valuable insights into the mechanisms leading to circumferential cracking.
- Exploration of Curved Intermediate Paths: An expanding application of metal spinning process with not only defect-free but also maximize spinning ratio.
- Application of Hot Spinning: The proposed mechanism theory assumes plastic deformation always induced by the roller. However, instances arise where the roller may not effectively deform harder materials leading to circumferential cracking. To validate the occurrence of plastic deformation, researchers can explore the application of hot spinning techniques.

APPENDIX I

STRESS – STRAIN CONVERSION

L, L_0 are the current and original gauge length. Engineering strain is defined as

$$\epsilon_{\text{engineering}} = \frac{\mathrm{L} - \mathrm{L}_0}{\mathrm{L}_0} = \frac{\mathrm{L}}{\mathrm{L}_0} - 1 \tag{A I-1}$$

True strain is calculated from engineering strain as

$$\begin{aligned} \epsilon_{\text{true}} &= \ln\left(\frac{\mathrm{L}}{\mathrm{L}_0}\right) \\ \rightarrow \epsilon_{\text{true}} &= \ln\left(\epsilon_{\text{engineering}} - 1\right) \end{aligned} \tag{A I-2}$$

The conversion of engineering stress to true stress:

Definition of A, A_0 are the current and original cross section area. Engineering stress refers to origin area, $\sigma_{\text{engineering}} = \frac{\mathrm{P}}{\mathrm{A}_0}$ while true stress refers to current area $\sigma_{\text{true}} = \frac{\mathrm{P}}{\mathrm{A}}$, thus the relation between engineering stress and true stress is

$$\frac{\sigma_{\text{true}}}{\sigma_{\text{engineering}}} = \frac{\mathrm{A}_0}{\mathrm{A}} \tag{A I-3}$$

Because the change of volume is constant in the plastic region which yields

$$\mathrm{AL} = \mathrm{A}_0\mathrm{L}_0 \tag{A I-4}$$

The formula is valid before necking onset. Substitute equation (A I-4) and (A I-1) into equation (A I-3), the true stress is calculated as below.

$$\sigma_{true} = \sigma_{engineering}\left(\epsilon_{engineering} + 1\right) \quad \text{(A I-5)}$$

APPENDIX II

DEFINITION OF THE EFFECTIVE PLASTIC STRAIN

The effective plastic strain is defined intuitively by a similar formula as the effective stress (Von Mises). The incremental form of effective plastic strain is defined as

$$d\epsilon_p = C\sqrt{\left(d\epsilon_{p1} - d\epsilon_{p2}\right)^2 + \left(d\epsilon_{p2} - d\epsilon_{p3}\right)^2 + \left(d\epsilon_{p3} - d\epsilon_{p1}\right)^2} \quad \text{(A II-1)}$$

With C is an unknown parameter. C is chosen such as $d\epsilon_p$ reduces to $d\epsilon_{p1}$ in case of tensile test. The material does not change its volume during plastic, so the Poisson's ratio is 0.5. Therefore, $d\epsilon_{p2} = d\epsilon_{p3} = -\frac{1}{2}d\epsilon_{p1}$ which $d\epsilon_{p2}$, $d\epsilon_{p3}$ is the incremental transverse plastic strain and $d\epsilon_{p1}$ is the incremental axial plastic strain in tensile test. Based on this information, the equation (A II-1) becomes

$$d\epsilon_p = Cd\epsilon_{p1}\sqrt{\frac{9}{4} + 0 + \frac{9}{4}} = C\frac{3}{\sqrt{2}}d\epsilon_{p1} \quad \text{(A II-2)}$$

Applies $d\epsilon_p = d\epsilon_{p1}$, so $C = \frac{\sqrt{2}}{3}$. Finally, the incremental plastic strain is

$$d\epsilon_p = \frac{\sqrt{2}}{3}\sqrt{\left(d\epsilon_{p1} - d\epsilon_{p2}\right)^2 + \left(d\epsilon_{p2} - d\epsilon_{p3}\right)^2 + \left(d\epsilon_{p3} - d\epsilon_{p1}\right)^2} \quad \text{(A II-3)}$$

LIST OF BIBLIOGRAPHICAL REFERENCES

A. Haufe M. Feucht, P. DuBois and T. Borvall, F. N. (2010). A comparison of recent damage and failure models for steel materials in crashworthiness application in LS-DYNA. *11 International LS-DYNA Users Conference, Detroit*, 1–39.

ABAQUS. (2019). Abaqus User's Manual version 2019. *Dassault Systèmes Simulia Corp.: Providence, RI, USA*.

Abd-Alrazzaq, M., Ahmed, M., & Younes, M. (2018). Experimental Investigation on the Geometrical Accuracy of the CNC Multi-Pass Sheet Metal Spinning Process. *Journal of Manufacturing and Materials Processing 2018, Vol. 2, Page 59*, *2*(3), 59. https://doi.org/10.3390/JMMP2030059

Alberti, N., Cannizzaro, L., Lo Valvo, E., & Micari, F. (1989). Analysis of metal spinning processes by the ADINA code. *Computers & Structures*, *32*(3–4), 517–525. https://doi.org/10.1016/0045-7949(89)90343-X

Andrade, F. (Daimler A., Feucht, M. (Daimler A., & Haufe, A. (DYNAmore G. (2014). On the Prediction of Material Failure in LS-DYNA ® : A Comparison Between GISSMO and DIEM. *13th International LS-DYNA Users Conference*, 1–12.

Awiszus, B., & Härtel, S. (2011). Numerical simulation of non-circular spinning: A rotationally non-symmetric spinning process. *Production Engineering*, *5*(6), 605–612. https://doi.org/10.1007/s11740-011-0335-9

Bruhns, O. T. (2003). Plates and Shells. In *Advanced Mechanics of Solids* (pp. 131–148). Berlin, Heidelberg: Springer Berlin Heidelberg. https://doi.org/10.1007/978-3-662-05271-6_8

Chen, S. W., Gao, P. F., Zhan, M., Ma, F., Zhang, H. R., & Xu, R. Q. (2019a). Determination of formability considering wrinkling defect in first-pass conventional spinning with linear roller path. *Journal of Materials Processing Technology*, *265*, 44–55. https://doi.org/10.1016/j.jmatprotec.2018.10.003

Chen, S. W., Gao, P. F., Zhan, M., Ma, F., Zhang, H. R., & Xu, R. Q. (2019b). Determination of formability considering wrinkling defect in first-pass conventional spinning with linear

roller path. *Journal of Materials Processing Technology*, *265*, 44–55. https://doi.org/10.1016/j.jmatprotec.2018.10.003

Chen, S. W., Zhan, M., Gao, P. F., Ma, F., & Zhang, H. R. (2021). A new robust theoretical prediction model for flange wrinkling in conventional spinning. *Journal of Materials Processing Technology*, *288*(February 2020), 116849. https://doi.org/10.1016/j.jmatprotec.2020.116849

Effelsberg, J., Haufe, A., Feucht, M., Neukamm, F., & Bois, P. Du. (2012). On parameter identification for the GISSMO damage model. *12th International LS-DYNA Users Conference*, (3), 1–12. Retrieved from https://www.researchgate.net/publication/312046900_On_Parameter_Identification_for_the_GISSMO_Damage_Model

El-Khabeery, M. M., Fattouh, M., El-Sheikh, M. N., & Hamed, O. A. (1991). On the conventional simple spinning of cylindrical aluminium cups. *International Journal of Machine Tools and Manufacture*, *31*(2), 203–219. https://doi.org/10.1016/0890-6955(91)90005-N

Essa, K, & Hartley, P. (2010). Optimization of conventional spinning process parameters by means of numerical simulation and statistical analysis. *Proceedings of the Institution of Mechanical Engineers, Part B: Journal of Engineering Manufacture*, *224*(11), 1691–1705. https://doi.org/10.1243/09544054JEM1786

Essa, Khamis, & Hartley, P. (2009). Numerical simulation of single and dual pass conventional spinning processes. *International Journal of Material Forming*, *2*(4), 271–281. https://doi.org/10.1007/s12289-009-0602-x

Gao, P. F., Yan, X. G., Li, F. G., Zhan, M., Ma, F., & Fu, M. W. (2022). Deformation mode and wall thickness variation in conventional spinning of metal sheets. *International Journal of Machine Tools and Manufacture*, *173*. https://doi.org/10.1016/J.IJMACHTOOLS.2021.103846

Härtel, S., & Laue, R. (2016). An optimization approach in non-circular spinning. *Journal of Materials Processing Technology*, *229*, 417–430. https://doi.org/10.1016/j.jmatprotec.2015.09.003

Hayama, M., Kudo, H., & Shinokura, T. (1970). Study of the Pass Schedule in Conventional Simple Spinning. *Bulletin of JSME*, *13*(65), 1358–1365. https://doi.org/10.1299/jsme1958.13.1358

Inc, H. W. international. (2010). *Aluminium 1100-O properties*.

Kleiner, M., Göbel, R., Kantz, H., Klimmek, C., & Homberg, W. (2002). Combined methods for the prediction of dynamic instabilities in sheet metal spinning. *CIRP Annals - Manufacturing Technology*. https://doi.org/10.1016/S0007-8506(07)61501-7

Kong, Q., Yu, Z., Zhao, Y., Wang, H., & Lin, Z. (2017a). A study of severe flange wrinkling in first-pass conventional spinning of hemispherical part. *International Journal of Advanced Manufacturing Technology*, *93*(9–12), 3583–3598. https://doi.org/10.1007/s00170-017-0744-9

Kong, Q., Yu, Z., Zhao, Y., Wang, H., & Lin, Z. (2017b). A study of severe flange wrinkling in first-pass conventional spinning of hemispherical part. *International Journal of Advanced Manufacturing Technology*, *93*(9–12), 3583–3598. https://doi.org/10.1007/s00170-017-0744-9

Kong, Q., Yu, Z., Zhao, Y., Wang, H., & Lin, Z. (2017c). Theoretical prediction of flange wrinkling in first-pass conventional spinning of hemispherical part. *Journal of Materials Processing Technology*, *246*, 56–68. https://doi.org/10.1016/j.jmatprotec.2016.07.031

Li, L., Chen, S., Lu, Q., Shu, X., Zhang, J., & Shen, W. (2023). Effect of Process Parameters on Spinning Force and Forming Quality of Deep Cylinder Parts in Multi-Pass Spinning Process. *Metals 2023, Vol. 13, Page 620*, *13*(3), 620. https://doi.org/10.3390/MET13030620

Li, Z. H., & Long, H. (2022). An analytical model integrated with toolpath design for wrinkling prediction in conventional spinning. *Journal of Materials Processing Technology*, *300*, 117399. https://doi.org/10.1016/j.jmatprotec.2021.117399

Liu, C.-H. (2007). The simulation of the multi-pass and die-less spinning process. *Journal of Materials Processing Technology*, *192*, 518–524. https://doi.org/10.1016/j.jmatprotec.2007.04.021

Liu, Yang, H., & Li, Y. Q. (2002). A study of the stress and strain distributions of first-pass conventional spinning under different roller-traces. *Journal of Materials Processing Technology*, *129*(1), 326–329. https://doi.org/10.1016/S0924-0136(02)00682-9

Mackenzie, A. C., Hancock, J. W., & Brown, D. K. (1977). On the influence of state of stress on ductile failure initiation in high strength steels. *Engineering Fracture Mechanics*. https://doi.org/10.1016/0013-7944(77)90062-5

Marghmaleki, Beni, Y. T., Noghrehabadi, A. R., Kazemi, A. S., & Abadyan, M. (2011). Finite element simulation of thermomechanical spinning process. *Procedia Engineering*, *10*, 3769–3774. https://doi.org/10.1016/j.proeng.2011.04.616

Marghmaleki, I. S., & Beni, Y. T. (2014). Thermo-Mechanical Investigation of Spinning Process. *Arabian Journal for Science and Engineering*, *39*(2), 1209–1217. https://doi.org/10.1007/s13369-013-0674-2

Mori, K.-I., & Nonaka, T. (2004). Simplified Three-Dimensional Finite Element Simulation of Shear Spinning Process Based on Axi-Symmetric Modeling. *Journal of the Japan Society for Technology of Plasticity*, *45*(517), 34–38. https://doi.org/http://dx.doi.org/10.1016/S1526-6125(05)70081-5

Music, O., Allwood, J. M., & Kawai, K. (2010a). A review of the mechanics of metal spinning. *Journal of Materials Processing Technology*, *210*(1), 3–23. https://doi.org/10.1016/j.jmatprotec.2009.08.021

Music, O., Allwood, J. M., & Kawai, K. (2010b). A review of the mechanics of metal spinning. *Journal of Materials Processing Technology*, *210*(1), 3–23. https://doi.org/10.1016/j.jmatprotec.2009.08.021

Needleman, A., & Tvergaard, V. (1984). An analysis of ductile rupture in notched bars. *Journal of the Mechanics and Physics of Solids*. https://doi.org/10.1016/0022-5096(84)90031-0

Neukamm, F, Feucht, M., Haufe, A., & Roll, K. (2008). On Closing the Constitutive Gap Between Forming and Crash Simulation. In *10th International LSDYNA Users Conference* (pp. 21–32).

Neukamm, Frieder, Feucht, M., & Haufe, A. (2009). Considering damage history in crashworthiness simulations. *7th European LS-DYNA Conference*. Retrieved from https://www.dynamore.de/en/downloads/papers/09-conference/papers/B-III-02.pdf/view

Nguyen, H. H., Champliaud, H., & Lê, V. N. (2018). Dynamic finite element modeling of metal spinning process with a stationary mandrel and a rotating tool. *30th European Modeling and Simulation Symposium, EMSS 2018*, 91–96.

Nguyen, H. H., Champliaud, H., & Lê, V. N. (2020). Circumferential cracking in conventional metal spinning process. *32nd European Modeling and Simulation Symposium, EMSS 2020*, 165–170. https://doi.org/10.46354/I3M.2020.EMSS.023

Polyblank, J. A., & Allwood, J. M. (2015). Parametric toolpath design in metal spinning. *CIRP Annals - Manufacturing Technology*, *64*(1), 301–304. https://doi.org/10.1016/j.cirp.2015.04.077

Quigley, E., & Monaghan, J. (2002). Enhanced finite element models of metal spinning. *Journal of Materials Processing Technology*, *121*(1), 43–49. https://doi.org/10.1016/S0924-0136(01)01138-4

Ravi-Chandar, K. (2004). Dynamic fracture, 254.

Rentsch, B., Manopulo, N., & Hora, P. (2017). Numerical modelling, validation and analysis of multi-pass sheet metal spinning processes. *International Journal of Material Forming*, *10*(4), 641–651. https://doi.org/10.1007/s12289-016-1308-5

Russo, I. M., Cleaver, C. J., & Allwood, J. M. (2021). Seven principles of toolpath design in conventional metal spinning. *Journal of Materials Processing Technology*, *294*, 117131. https://doi.org/10.1016/J.JMATPROTEC.2021.117131

Semiatin, S. L. (2006). Manual sheet forming. In *ASM Handbook, Metalworking: Sheet Forming* (Vol. 14B, pp. 367–374). ASM International. Retrieved from https://app.knovel.com/hotlink/khtml/id:kt008I1ZR5/asm-handbook-volume-14b/asm-handbo-materials

Smith, M. (2020). *ABAQUS/Standard User's Manual, Version 6.9*. *Dassault Systemes Simulia Corpia Corp*.

Šugár, P., Šugárová, J., & Petrovič, J. (2016). Analysis of the effect of process parameters on part wall thickness variation in conventional metal spinning of Cr-Mn austenitic stainless steels. *Strojniski Vestnik/Journal of Mechanical Engineering*, *62*(3), 171–178. https://doi.org/10.5545/SV-JME.2015.2901

Sugita, Y., & Arai, H. (2015). Formability in synchronous multipass spinning using simple pass set. *Journal of Materials Processing Technology*, *217*, 336–344. https://doi.org/10.1016/J.JMATPROTEC.2014.11.017

Thickness Tolerances of Aluminium from Ullrich Aluminium. (n.d.). Retrieved September 13, 2022, from https://www.ullrich-aluminium.co.nz/rolled/rpstand1.php

Wang, L., & Long, H. (2011). A study of effects of roller path profiles on tool forces and part wall thickness variation in conventional metal spinning. *Journal of Materials Processing Technology*, *211*(12), 2140–2151. https://doi.org/10.1016/j.jmatprotec.2011.07.013

Watson, M., Long, H., & Lu, B. (2015). Investigation of wrinkling failure mechanics in metal spinning by Box-Behnken design of experiments using finite element method. *International Journal of Advanced Manufacturing Technology*, *78*(5–8), 981–995. https://doi.org/10.1007/s00170-014-6694-6

Watson, Michael, & Long, H. (2014). Wrinkling Failure Mechanics in Metal Spinning. *Procedia Engineering*, *81*, 2391–2396. https://doi.org/10.1016/J.PROENG.2014.10.339

Xia, Q., Shima, S., Kotera, H., & Yasuhuku, D. (2005). A study of the one-path deep drawing spinning of cups. *Journal of Materials Processing Technology*, *159*(3), 397–400. https://doi.org/10.1016/j.jmatprotec.2004.05.027

Xia, Y., Shu, X., Zhu, Y., & Li, Z. (2020). Influence of process parameters on forming load of variable-section thin-walled conical parts in spinning. *Applied Sciences (Switzerland)*, *10*(17). https://doi.org/10.3390/app10175932

Yu, Z., Zhao, Y., Du, C., Liu, R., & Evsyukov, S. A. (2020). Study on flange-constrained spinning process for hemispherical aluminum alloy part. *Journal of Materials Processing Technology*, *278*(October 2019), 116515. https://doi.org/10.1016/j.jmatprotec.2019.116515

Zhan, M., Yang, H., Zhang, J. H., Xu, Y. L., & Ma, F. (2007). 3D FEM analysis of influence of roller feed rate on forming force and quality of cone spinning. *Journal of Materials Processing Technology*, *187–188*, 486–491. https://doi.org/10.1016/j.jmatprotec.2006.11.114